

1 **Paxillin facilitates timely neurite initiation on soft-substrate**
2 **environments by interacting with the endocytic machinery**

3
4 Ting-Ya Chang¹, Chen Chen¹, Min Lee¹, Ya-Chu Chang¹, Chi-Huan Lu¹, Shao-Tzu Lu¹,
5 De-Yao Wang¹, Aijun Wang², Chin-Lin Guo³ and Pei-Lin Cheng^{1,*}

6
7 ¹Institute of Molecular Biology, Academia Sinica, 128 Academia Road, Section 2,
8 Nankang, Taipei 11529, Taiwan

9 ²Surgical Bioengineering Laboratory, Department of Surgery, UC Davis, 4625 2nd Ave.,
10 Suite 3005, Sacramento, USA

11 ³Institute of Physics, Academia Sinica, 128 Academia Road, Section 2, Nankang
12 District, Taipei 11529, Taiwan

13
14
15
16
17
18 **Short title: Endocytic Activity Enables Timely Neurite Initiation**

19
20
21
22
23
24 *Corresponding author: Pei-Lin Cheng, plcheng@imb.sinica.edu.tw
25
26
27
28
29
30
31
32
33
34

35 Key words: neurite initiation, endocytosis, paxillin, substrate elasticity, bistable switch
36

37 **Abstract**

38 Neurite initiation is the first step in neuronal development and occurs spontaneously in
39 soft tissue environments. Although the mechanisms regulating the morphology of
40 migratory cells on rigid substrates in cell culture are widely known, how soft
41 environments modulate neurite initiation remains elusive. Using hydrogel cultures,
42 pharmacologic inhibition, and genetic approaches, we reveal that paxillin-linked
43 endocytosis and adhesion are components of a bistable switch controlling neurite
44 initiation in a substrate modulus-dependent manner. On soft substrates, most paxillin
45 binds to endocytic factors and facilitates vesicle invagination, elevating neuritogenic
46 Rac1 activity and expression of genes encoding the endocytic machinery. By contrast,
47 on rigid substrates, cells develop extensive adhesions, increase RhoA activity and
48 sequester paxillin from the endocytic machinery, thereby delaying neurite initiation. Our
49 results highlight paxillin as a core molecule in substrate modulus-controlled
50 morphogenesis and define a mechanism whereby neuronal cells respond to
51 environments exhibiting varying mechanical properties.

52
53
54
55
56
57
58
59
60
61
62
63
64
65
66

67 Introduction

68 Environmental rigidity affects cell morphogenesis and development. For example,
69 mesenchymal cells develop long protrusions and spread when they are cultured on
70 glass coverslips or plastic plates (Lo, Wang et al., 2000), but fail to do so on soft
71 substrates ($E < 5$ kPa) in cell culture. Likewise, rigid substrates ($E > 20$ kPa) facilitate
72 differentiation of mesenchymal stem cells into osteogenic cells (Engler, Sen et al.,
73 2006). In fact, the behavior of mesenchymal cells reflects the response of most
74 migratory/adherent cells. By contrast, newborn neurons, which naturally reside in
75 extremely soft tissue environments ($E = 0.1\text{--}1$ kPa) such as brain (Christ, Franze et al.,
76 2010, Georges, Miller et al., 2006), behave differently. Soft mechanical properties
77 generally favor neuronal differentiation (Engler et al., 2006, Saha, Keung et al., 2008)
78 and maturation (Balgude, Yu et al., 2001, Fawcett, Barker et al., 1995, Leach, Brown et
79 al., 2007). In particular, neurons extend long protrusions known as neurites towards
80 softer surfaces when cultured on substrates showing a stiffness gradient
81 (Sundararaghavan, Monteiro et al., 2009). *In vivo* evidence for the inverse durotaxis of
82 neuronal cells has been provided recently using retinal ganglion cells of *Xenopus*
83 embryos, which exhibited a noticeable pattern of stiffness gradients within the optic
84 tracts towards their targets in the optic tectum (Koser, Thompson et al., 2016). Such
85 distinct behavior plays a crucial role in establishing projections and dendritic territory.
86 Although transduction mechanisms governing the development and behavior of
87 migratory cells on rigid substrates in cell culture are well characterized (Aragona,
88 Panciera et al., 2013, Dupont, Morsut et al., 2011), mechanisms underlying how
89 neurons behave differently from migratory cells on soft substrates remain elusive.

90 In general, development of cell shape depends on coordination of dynamic
91 membrane activities such as endocytosis, exocytosis, or adhesion with cytoskeletal
92 mechanics. For adherent cells grown on matrices, development of cell shape primarily
93 relies on integrin-mediated adhesions, which recruit molecules such as paxillin and
94 vinculin (Dumbauld, Lee et al., 2013, Humphries, Wang et al., 2007, Schaller, 2001,
95 Turner, 2000) to adhesive anchorages and to generate tensile forces (Carisey, Tsang et
96 al., 2013, Desmouliere, Chaponnier et al., 2005). The morphogenetic differences

97 between neurons and migratory cells in soft environments suggest that mechanisms
98 other than integrin-mediated adhesion may function in neurite initiation. Potential
99 candidates are changes in the gene expression and cell signaling that govern
100 endocytosis, which functions not only in membrane dynamics but also in integrin
101 internalization and focal adhesion disassembly (Caswell, Chan et al., 2008, Du, Chen et
102 al., 2011, Itofusa & Kamiguchi, 2011, Nishimura & Kaibuchi, 2007, White, Caswell et al.,
103 2007). Furthermore, endocytosis is required to activate and recruit the neuritogenic
104 signal molecule Rac1 (Palamidessi, Frittoli et al., 2008) to the membrane, an activity
105 that enhances formation of cell protrusions through actin filament polymerization (Hall,
106 1998, McMahon & Boucrot, 2011, Merrifield & Kaksonen, 2014).

107 Neurite initiation is the very first step of a single neuron towards neuronal
108 networking. To fully appreciate the role of soft environments in neuronal development,
109 ranging from cell fate to cell shape, it is challenging but vital to determine the underlying
110 mechanism responsible for the spatiotemporal control of neurite initiation in the
111 embryonic brain. To investigate mechanisms driving neurite initiation in soft tissue
112 environments, we cultured embryonic rat primary hippocampal neurons on hydrogels of
113 various elastic moduli and monitored spatiotemporal patterns of neurite initiation and
114 corresponding changes in gene expression. We observed a bistable pattern of neurite
115 initiation associated with altered expression of genes encoding components of the
116 endocytic machinery. In the absence of neurite-promoting factors, endocytosis was
117 required for cells to form the morphological precursors of neurites, i.e. segmented
118 lamellipodia. We identified paxillin as a key protein that directly associates with either
119 the adhesion protein vinculin or the F-BAR-containing endocytic factor CIP4. When
120 grown on soft substrates, cells expressed high levels of paxillin associated with the
121 endocytic machinery, which in turn upregulated Rac1 activity to promote neurite
122 formation and elevate expression of proteins of the endocytic machinery as part of a
123 positive feedback loop. By contrast, cells grown on rigid substrates developed
124 numerous adhesions, which sequestered paxillin from the endocytic machinery and
125 delayed neurite initiation. Using genetic profiling and biochemical approaches, we show
126 that paxillin-mediated endocytosis and formation of adhesions constitute a bistable
127 switch to control neurite initiation in a substrate modulus-dependent manner.

128 **Results**

129 **Bistable substrate modulus-dependent behavior in neurite initiation**

130 We used polymerized hydrogels to define the mechanisms underlying neurite initiation
131 in soft environments. Gels of three elastic moduli—0.1, 1 and 20 kPa—were engineered
132 and verified by atomic force microscopy (see Materials and methods, and Figure 1–
133 figure supplement 1A-D). Culturing hippocampal cells isolated from embryonic day 17.5
134 (E17.5) rat brain on these compliant gels can selectively enrich the population of
135 neurons by up to 80% and minimize growth of glial cells (Figure 1– figure supplement
136 1E). After seeding cells onto gels and incubating them for either 5 or 16 hr in regular
137 neurobasal medium, we assessed potential morphogenetic changes in cells over time.
138 Upon initial gel contact, cells formed a uniform lamellipodial extension (Figure 1A1, and
139 Figure 1– figure supplement 2A,B), which became segmented into multiple, separated
140 lamellipodia if the gel was sufficiently soft (see Figure 1– figure supplement 2A-D).
141 Lamellipodia are well-known morphological precursors of neurites (Figure 1– figure
142 supplement 2; (Dehmelt, Smart et al., 2003). However, we observed that neurites
143 formed only if their preceding lamellipodia occupied less than a third of the entire cell
144 periphery; lamellipodia occupying $>1/3$ of the periphery failed to form neurites even at
145 the 16 hr time-point (Figure 1A2-A4, and Figure 1– figure supplement 2A-D). Therefore,
146 we defined each lamellipodium with $<1/3$ occupancy of the entire cell periphery as a
147 "segmented" lamellipodium (SL), and those occupying $>1/3$ as a "broad" lamellipodium
148 (BL). In most, if not all, cases of the 5 hr cultures, a single cell could not have both SL
149 and BL.

150 We identified a bistable substrate modulus-dependent behavior by measuring the
151 distribution of SL and BL over various substrates of varying stiffness (Figure 1A3, and
152 Figure 1– figure supplement 2 E, F). Cells could be segregated into two populations, i.e.
153 those with or without SL formation, in a substrate modulus-dependent manner. For
154 example, in 5 hr soft-gel cultures (0.1 kPa), nearly 100% of cells formed SL (Figure 1A4,
155 A5, and Figure 1– figure supplement 2E), whereas most cells ($\sim 71.5\%$) on stiff-gel
156 cultures ($E=20$ kPa) or coverslips (glass) failed to form SL and instead formed a single
157 BL (Figure 1A4, and Figure 1– figure supplement 2E, F). In 16 hr cultures, the SL of

158 most (~98%) cells on soft gels had become neurites, whereas more than half (~57.3%)
159 of the cells on stiff gels possessed BL and lacked neurites (Figure 1A5). Such bistable
160 behavior suggests the existence of two distinct states in early stages of neuritogenesis;
161 a “segmentable state” in which cells can form segmented lamellipodia as morphological
162 predecessors of neurites, and a “non-segmentable state” in which cells retain a
163 spreading morphology with broad lamellipodia. The fact that cells form neurites on soft
164 gels in the absence of neurite-promoting growth factors suggests that culturing cells on
165 environments with elastic moduli <1 kPa, which match the mechanical properties of
166 brain ($E= 0.1\text{—}1$ kPa; (Christ et al., 2010, Georges et al., 2006), is sufficient to initiate
167 neurite formation. Moreover, surface laminin was detectable on 0.1 kPa, 20 kPa and
168 glass surfaces, and it was comparable following 5 and 16 hr incubation periods in
169 neuronal culture media (see Figure 1– figure supplement 1D), ruling out a difference
170 due to coating. Note that when culturing cells on coverslips, lower laminin/PLL
171 concentrations may be required for proper laminin/integrin interaction to overcome the
172 influences of high substrate rigidity (please see Appendix–figure 1).

173

174 **Substrate modulus-dependent morphogenesis is associated with** 175 **distinct cell signaling and gene expression patterns**

176 To ascertain whether changes in gene expression are associated with segmentable or
177 non-segmentable states, we undertook genetic profiling of cells grown on soft or stiff
178 substrates at 5 or 16 hr time-points. Using mRNA microarray and Gene Ontology
179 analyses, we identified 114 differentially-expressed mRNA transcripts in cells grown on
180 0.1 kPa and 20 kPa gels at the 5 hr time-point (filtering criteria: fold change ≥ 1.5 , $p < 0.05$;
181 Figure 1– figure supplement 3A, and Appendix–Table 1, 2). Among them, 66 were
182 upregulated in 0.1 kPa gel cultures and the remainder were downregulated (compared
183 to cells grown on stiffer substrates). Notably, three genes—*Cltc*, *Dab2*, and *Myo6*, all of
184 which function in clathrin-mediated endocytosis—were co-upregulated in 0.1 kPa gel
185 cultures at the 5 hr time-point (Figure 1– figure supplement 3B), suggesting that cells
186 enter a high endocytic state on a soft substrate ($E=0.1$ kPa). By contrast, several
187 adhesion factors, including *Vcl*, *Nrcam*, *Robo2* and *Cdh11*, were relatively upregulated

188 in 20 kPa gel cultures at 5 hr and/or 16 hr compared to cells grown on softer substrates
189 (Figure 1– figure supplement 3B).

190 To verify that changes in gene expression associated with endocytosis or
191 adhesion were correlated with phenotypic changes, we performed single molecular RNA
192 fluorescent in situ hybridization (smFISH, see Materials and methods for details), which
193 enables mRNA quantitation in two groups of single cells based on their morphological
194 signatures, i.e., BL or SL (Figure 1– figure supplement 3C). For this analysis, we
195 examined nine genes involved in three different types of cellular activities: endocytosis,
196 adhesion, and the Hippo-YAP pathway. All of these pathways regulate membrane
197 mechanics under certain conditions. In 5 hr cultures, we found that SL cells expressed
198 relatively lower (2.3- to 10-fold) and higher (1.2- to 4-fold) levels of adhesion-related
199 (*Vcl*, *Cdh11* and *Robo2*) and endocytic (*Cltc*, *Dab2*, and *Myo6*) mRNA, respectively,
200 compared to those of BL cells (Figure 1– figure supplement 3C). However, no significant
201 differences were observed in levels of the Hippo-YAP-related (*DKK1* and *CYR61*)
202 mRNA between SL and BL cells. Although fold-changes in gene expression vary across
203 signal detection methods (Figure 1– figure supplement 3), these findings are consistent
204 with the microarray data and suggest that cells with segmented lamellipodia undergo
205 preferential gene expression of endocytic- but not adhesion-related genes.

206

207 **Elevated endocytic activity is associated with soft substrate** 208 **environments and is critical for neurite development *in vivo***

209 To ascertain whether neurons enter an endocytic-dominant state upon contact with soft
210 environments, we measured endocytic activity in cells grown on soft or stiff gels. To
211 assess endocytosis, first we monitored uptake of the lipophilic dye FM4-64 over a 40
212 min period (at 2 min intervals) in 5 hr cultures (Figure 1B1). The rate of FM4-64 uptake
213 was reflected by the time required to reach half of the maximum FM4-64 intensity
214 measured in cells, defined as $t_{1/2}$. We observed that cells grown on 0.1 kPa gels
215 exhibited a ~1.6-fold greater FM4-64 intensity at the end-point of the measurements
216 ($t=40$ min), and a ~1.7-fold greater uptake rate [$t_{1/2}$ (0.1 kPa) v.s. $t_{1/2}$ (20 kPa) = 16.8 min v.s.

217 24.8 min] than cells grown on 20 kPa gels (Figure 1B1). Robust dye uptake was
218 pharmacologically and genetically abolished by applying inhibitors of dynamin GTPase
219 and by ectopically expressing a dominant-negative Dynamin II mutant (DynII^{K44A};
220 (Damke, Baba et al., 1994, Herskovits, Burgess et al., 1993) in 0.1 kPa cultures,
221 respectively (Figure 1B1, B2). These results suggest that dye uptake is primarily
222 endocytosis-associated. Note that constructs encoding DynII^{K44A} were in utero
223 electroporated (IUE, (Saito & Nakatsuji, 2001) into the developing brain of E16 rat
224 embryos. Cultures were prepared 24 hours after electroporation to allow for sufficient
225 expression of DynII^{K44A}. To confirm that levels of legend-mediated endocytosis were
226 elevated in neurons grown on soft substrates, we then quantified invagination of
227 quantum dot-conjugated brain-derived neurotrophic factor (denoted as QD-BDNF and
228 exhibiting a 1:1 BDNF:QD conjugation ratio; see Materials and methods) in 16 hr
229 cultures (Figure 1B3). We observed an average invagination rate of ~7 dots per cell in
230 0.1 kPa cultures over the first 5 hours after bath application of QD-BDNF. That rate was
231 significantly decreased to 2 dots per cell in 20 kPa cultures (Figure 1B3), and
232 comparable results were seen following dynamin inhibition (Figure 1B2). These findings
233 suggest that cells grown on soft substrates undergo a high level of endocytosis.

234 These findings prompted us to examine the functional relevance of endocytic
235 activity on neurite formation *in vivo*. To do so, we used in utero electroporation to
236 express constructs encoding a dominant-negative Dynamin II mutant (DynII^{K44A}) in a
237 subpopulation of neural progenitor cells (Figure 1 C). To aid observations of
238 morphogenetic phenotypes, brain slices were obtained from newborn (P0) rat cortex
239 when most newly differentiated neurons had extended their neurites and migrated
240 towards the cortical plate. Nearly all (~100%) control cortical neurons (i.e., those solely
241 expressing marker protein) exhibited a neurite-bearing, polarized morphology (Figure
242 1C1, C3), with dendritic arbors being oriented towards the pial surface and the axon
243 being oriented radially in the cortical plate. By contrast, cortical neurons expressing
244 DynII^{K44A} exhibited an apparent migration defect (Figure 1C1, C2), with a high
245 percentage of cells having a non-polarized morphology without extension of minor
246 processes (termed “no neurite”) and a reduced percentage of cells exhibiting a
247 polarized morphology (unipolar or bipolar) (Figure 1C3). Thus, a normal level of

248 endocytic reactions is required for proper neurite formation and radial migration of newly
249 generated cortical neurons; two tightly linked events during neuronal development
250 *in vivo*.

251

252 **The endocytic-dominant state on soft substrates favors Rac1** 253 **signaling and neurite formation**

254 Endocytosis enhances membrane translocation and Rac1 activation (Palamidessi et al.,
255 2008) and, though in opposing manners, both RhoA and Rac1 function in neurite
256 formation (Aoki, Nakamura et al., 2004, Da Silva, Medina et al., 2003, Govek, Newey et
257 al., 2005, Machacek, Hodgson et al., 2009); reviewed in (Guilluy, Garcia-Mata et al.,
258 2011). Given the dominance of endocytosis events on soft gels, we wondered whether
259 the substrate modulus governed Rac1 activity. Using an active Rac1 pulldown assay,
260 immunofluorescent staining of Rac1 or active Rac1, and the FRET biosensor Rac1-2G
261 (Fritz, Letzelter et al., 2013, Fritz, Menshykau et al., 2015), we observed that, unlike
262 RhoA, Rac1 activity decreased with increasing stiffness of the substrate in 5 hr neuronal
263 cultures (Figure 2– figure supplement 1A). In addition, active Rac1 accumulated in SL
264 and the tips of growing neurites, whereas there was no accumulation in BL (Figure 2A1,
265 A3). Consistently, ratiometric FRET imaging confirmed accumulation of active Rac1 at
266 segmented neuronal lamellipodia on soft gels (0.1 kPa), with FRET signal decreasing
267 from the leading edge to the cell body (Figure 2B1, B2). Moreover, either expression of
268 DynII^{K44A} or treatment of the 0.1 kPa cultures with inhibitors of endocytosis significantly
269 blocked accumulation of active Rac1 (Figure 2A1-A3). These results suggest that Rac1
270 accumulation requires endocytosis.

271 Previous studies have shown that Rac1 activation induces cell protrusions through
272 actin filament polymerization (reviewed in (Hall, 1998, Ridley, 2011)). To ascertain
273 whether Rac1 increase and accumulation on soft gels (0.1 kPa) was responsible for
274 neurite initiation, we treated cells grown on soft gels with the Rac1 inhibitor NSC 23766
275 immediately after plating and assessed phenotypes at the 5 hr time-point, which
276 resulted in the onset of lamellipodial segmentation being significantly delayed (see 48 hr
277 time-point in Figure 2– figure supplement 1B). In support of the idea that Rac1

278 accumulation requires endocytosis (Figure 2A), inhibition of endocytosis in soft-gel
279 cultures for 1 hr also significantly increased manifestation of the BL phenotype at the 5
280 hr time-point (Figure 2C1), with >90% of cells exhibiting sparsely distributed and less
281 activated Rac1 and broad lamellipodia that resembled those seen on 20 kPa gels
282 (Figure 2A, B). The number of neurite-bearing neurons was also decreased to ~13%
283 compared to the untreated control (Figure 2C2). In contrast, bath-application of Y27632
284 (an inhibitor of Rho-associated protein kinase, ROCK) or the PI3k inhibitor LY294002 to 0.1
285 kPa cultures did not alter the onset of lamellipodial segmentation (Figure 2– figure
286 supplement 1B). These results suggest that culturing cells on a soft substrate is
287 sufficient to promote a neuritogenic state through endocytosis-associated Rac1
288 activation.

289

290 **Model for competitive recruitment of paxillin to divergent cellular** 291 **machineries as part of a bistable switch**

292 In many biological systems, selection between two distinguishable states requires
293 changes in gene expression, which are then amplified via a bistable switch (reviewed in
294 (Ferrell, 2002, Smits, Kuipers et al., 2006). Our results suggest that newborn neurons
295 possess two morphological states: one with the ability to form segments and neurites
296 and the other without. These states are associated with specific genetic changes that
297 are governed by substrate stiffness, cell contractility, and endocytic activity (Figure 1
298 and Figure 2). To account for both endocytosis and adhesion, here we assume a simple
299 “sequestering” mechanism whereby a factor/switcher required for both endocytosis and
300 cell-substrate adhesion exists (mathematical model and figure shown in Appendix). To
301 identify the molecular switch, we evaluated by Western blot analysis the protein levels
302 of candidate molecules functioning in adhesion or the endocytosis machinery. In 5 hr
303 cultures on stiff substrates (20 kPa gels or glass), cells expressed higher levels of
304 adhesion factors (such as integrin β 1; for the level of active integrin, please see
305 Appendix–figure 3) than endocytic factors (Figure 3A, B). Although pFAK levels
306 increased slightly on stiff substrates, the changes were not statistically significant. By
307 contrast, cells grown on soft gels (0.1 kPa and 1 kPa) expressed higher levels of factors

308 associated with clathrin-mediated endocytosis, including myosin VI, clathrin heavy chain
309 (CHC) and Cdc42 interacting protein 4 (CIP4) (Figure 3A, B). Among the candidates of
310 interest, we also evaluated the scaffolding protein paxillin, which is known to be an
311 integral component of focal adhesions that bind vinculin and FAK (Schaller, 2001,
312 Turner, Glenney et al., 1990). We observed that expression levels of paxillin and
313 phosphorylated paxillin in cultured neurons did not match the profiles of other adhesion
314 factors, but instead matched the profiles of endocytic factors (Figure 3 A and B). Further
315 analysis of relative paxillin expression in 5 hr cultures indicated that cells grown on soft
316 substrates (0.1 kPa gels) expressed significantly higher levels of paxillin than those
317 grown on stiff substrates (Figure 3 B). These observations strongly suggest that paxillin
318 is associated with the endocytic machinery in soft cultures and may serve as the
319 proposed switcher.

320 Evidence for a role of paxillin in endocytosis is limited (but see (Duran, Rahman
321 et al., 2009). To examine this possibility, we assessed if paxillin is associated with
322 endocytic vesicles using a detergent-free membrane flotation assay of embryonic rat
323 cortex (with cardiac tissue used for comparison). We found >30% of paxillin from brain
324 lysates co-fractionated with the endocytosis factors Rab5 and CHC (in floating
325 membrane fractions), whereas co-fractionation was <5% in cardiac lysates (Figure 3–
326 figure supplement 1), suggesting that a significant proportion of paxillin is associated
327 with endocytic vesicles in neurons. Live cell imaging also revealed a long-range,
328 predominantly retrograde transport of paxillin-mCherry from axonal tips (Figure 3– figure
329 supplement 2; Figure 3-video 1); a behavior similar to that seen in neuronal signaling
330 endosomes (Cosker & Segal, 2014, Yap & Winckler, 2012). Next, we wondered whether
331 paxillin preferentially binds to endocytic rather than adhesion factors in the segmentable
332 state. Using 5 hr soft-gel cultures, we conducted immunostaining of endocytosis-
333 associated kinase AAK1 (Conner & Schmid, 2002, Ricotta, Conner et al., 2002) or
334 adhesion kinase p-FAK^{Y397}. A significant proportion (~39%) of paxillin staining
335 colocalized with that of AAK1 rather than p-FAK^{Y397} on soft gels (0.1 kPa; Figure 3C).
336 This outcome was quantitatively confirmed by confocal microscopy with enhanced
337 resolution (~1.7X greater using Airyscan). In cells exhibiting an SL phenotype on soft
338 gels (0.1 kPa), enhanced resolution confocal microscopy also revealed that a significant

339 portion (>40%) of paxillin appeared in a punctate pattern and co-localized with the
340 endocytic factors CHC or AAK1 (Pearson's coefficient > 0.75) rather than adhesion
341 factors p-FAK^{Y397} or vinculin (Pearson's coefficient < 0.45) (Figure 3D, F). Interestingly,
342 paxillin preferentially associated with p-FAK^{Y397} and vinculin in cells exhibiting BL on stiff
343 gels (20 kPa; Figure 3E, F). Together, these observations suggest that paxillin functions
344 in both endocytic and adhesion activities.

345

346 **Endocytic factor CIP4 and adhesion factor vinculin are potential** 347 **competitors for paxillin binding**

348 Validation of our model requires that a molecular switch binds to endocytic and
349 adhesion machineries in a competitive and substrate modulus-dependent manner. To
350 determine whether paxillin meets these criteria, we tested its binding to the endocytic
351 machinery using liquid chromatography-tandem mass spectrometry (LC-MS/MS) of
352 lysates from rat embryonic brain and *in vivo* co-immunoprecipitation of cortical neurons
353 cultured on hydrogels. Our analyses identified several endocytic factors that bind to
354 paxillin, including clathrin, dynamin, and CIP4 (Figure 4A-C, and Appendix-Table 3).
355 Moreover, the binding affinity of paxillin to these factors increased with substrate
356 compliance, whereas the binding affinity of paxillin to vinculin increased with substrate
357 stiffness (Figure 4A). These findings indicate that paxillin can switch its binding
358 preference in a substrate modulus-dependent manner.

359 Next, we examined whether binding of paxillin to endocytic or adhesion factors
360 is competitive. Structurally, paxillin is an adaptor protein composed of N-terminal LD
361 motifs and C-terminal LIM domains, both of which are important for binding to focal
362 adhesion factors (Brown, Perrotta et al., 1996, Brown, Perrotta et al., 1998). Among
363 those factors, vinculin exhibits a well-characterized paxillin-binding subdomain or "PBS"
364 (Tachibana, Sato et al., 1995, Wood, Turner et al., 1994). By evaluating potential
365 structural similarities between endocytic factors and the vinculin PBS, we found that the
366 F-BAR domain of CIP4 shares the greatest degree of similarity with the PBS (Figure 4-
367 figure supplement 1A). To ascertain whether this domain binds paxillin, we used GST-

368 fused full-length paxillin (GST-PXN^{FL}) to pull down bacterially-expressed, histidine-
369 tagged full-length (His-CIP4^{FL}) or F-BAR domain-deleted (His-CIP4^{ΔF-BAR}) CIP4. Both
370 proteins were HPLC-purified and biochemically confirmed by mass spectrometry. GST-
371 PXN^{FL} associated with His-CIP4^{FL} but not His-CIP4^{ΔF-BAR} (Figure 4B), confirming that
372 the F-BAR domain is required for paxillin binding.

373 Furthermore, using an *in vitro* GST pulldown assay and domain mapping
374 analysis in HEK293T cell lysates, we found that deletion of the LIM3-4 domain reduced
375 paxillin affinity for vinculin and CIP4 (Figure 4C, D). However, the paxillin interaction
376 domains for vinculin and CIP4 do not fully overlap, as vinculin and CIP4 primarily
377 associated with LD motifs (LD1, 2, and/or 4; (Turner, Brown et al., 1999) and the LIM
378 domain, respectively (Figure 4-figure supplement 1). In addition, deletion of LIM
379 domains and the last two LD domains (as seen in the paxillin^{LD1-3} construct) was
380 required to completely attenuate binding of vinculin and CIP4 to paxillin (see Figure 4C,
381 D). Given that CIP4 dimerizes *in vitro* and *in vivo* via its F-BAR domain (as verified by
382 small angle X-ray scattering analysis), we asked whether increased CIP4 binding to
383 paxillin LIM domains may spatially hinder vinculin from accessing the LD motifs. Indeed,
384 ectopic expression of full-length CIP4 or the F-BAR domain alone in HEK293T cells
385 decreased association of both GST-PXN^{FL} (Figure 4E) and endogenous paxillin (Figure
386 4F) with vinculin dose-dependently, but ectopic expression of the F-BAR-deleted CIP4
387 mutant (ΔN^1 -F-BAR) did not (Figure 4F, and Figure 4-figure supplement 1B-D). In
388 addition, competition assays using the paxillin variants GST-PXN^{FL}, GST-PXN^{ΔLD1}, and
389 GST-PXN^{ΔLIM3-4} showed that the CIP4-binding LIM 3-4 region, but not the vinculin-
390 binding LD1 motif, is required for high affinity CIP4 binding, as CIP4 could not out-
391 compete vinculin for binding to the paxillin- Δ LIM3-4 construct (Figure 4E, and Figure 4-
392 figure supplement 1F). These findings indicate that endocytic factors interact with the
393 paxillin LIM domain and are suggestive of a competitive-binding mechanism.

394

395 **Paxillin is required for robust neurite formation on soft substrates**

396 Given that endocytic activity is required for neurite initiation on a soft substrate, we
397 wondered whether paxillin and CIP4 function in endocytosis. To assess this, we

398 evaluated FM4-64 uptake in hippocampal neurons grown on soft substrates with or
399 without paxillin/CIP4 knockdown by shRNA (Figure 5– figure supplement 1). Reducing
400 paxillin and CIP4 levels in this way significantly decreased the rate and level of FM4-64
401 uptake (endocytosis) in neurons grown on soft gels (0.1 kPa; Figure 5A, C and Figure
402 5– figure supplement 2). This outcome was not seen following ectopic expression of the
403 shRNA-resistant paxillin mutant PXN-R (Figure 5A, C). Furthermore, ectopic expression
404 of full-length paxillin potentiated FM4-64 uptake in neurons grown on both soft and stiff
405 gels (0.1 kPa or 20 kPa; relative to untransfected neighboring control cells); an effect
406 not seen following ectopic expression of paxillin^{ΔLIM3-4} or paxillin^{LD1-3}, which lacks the
407 LIM-domain required for CIP4 association (Figure 5B, D and E). These findings suggest
408 that paxillin assists endocytosis on soft substrates via its interaction with components of
409 the endocytic machinery. Note that in neurons cultured on 20 kPa gels, but not on 0.1
410 kPa gels, we observed an altered CIP4 distribution along the enlarged lamella edge
411 (Figure 5– figure supplement 2); a pattern similar to that reported for coverslips
412 (Saengsawang, Mitok et al., 2012) on which the endocytic role of CIP4 may have been
413 compromised.

414 Based on its physical and functional association with CIP4 and CHC (Figure 4
415 and Figure 5), we wondered whether paxillin might participate in vesicle invagination
416 during clathrin-coated pit formation. To test this possibility, we quantified QD-BDNF
417 invagination in HEK293T cells with or without paxillin knockdown. Note that HEK293T
418 cells respond to BDNF only when transfected with a BDNF receptor (TrkB) expression
419 construct (see Figure 6A). We did not observe detectable QD-BDNF invagination into
420 non-TrkB-expressing HEK293T cells but, following transfection of cells with a TrkB
421 expression construct, we observed an average invagination rate of ~32 dots per cell
422 over the first hour after bath application of QD-BDNF. That rate significantly decreased
423 to 4 dots per cell on paxillin knockdown, and comparable results were seen following
424 CIP4 knockdown or dynasore treatment (Figure 6A, B). The decreased rates were
425 rescued by ectopic expression of shRNA-resistant PXN-R in the paxillin knockdown
426 experiment (Figure 6A). These findings suggest that paxillin is required for efficient
427 vesicle invagination.

428 The effect of paxillin loss on neurite formation was further evaluated by
429 measuring the rate at which paxillin knockdown cells enter a segmentable state. On soft
430 substrates (0.1 kPa), paxillin knockdown significantly increased the percentage of
431 neurons exhibiting the BL morphology and reduced the number of neurons bearing
432 neurites in 16 hr cultures, with these effects being similar to those seen following
433 treatment with the endocytosis inhibitors (Figure 2B, and Figure 7A, B). Further, paxillin
434 knockdown significantly reduced levels of active Rac1 accumulation at the protruding
435 edge (Figure 7C, D). These findings suggest that paxillin is a putative factor
436 participating in a substrate modulus-dependent bistable switch in neurite formation *in*
437 *vitro* (Figure 7 H). We also asked whether manipulating paxillin binding affinity for
438 endocytic or adhesion molecules could lead to a SL-BL phenotypic switch. Based on the
439 domain mapping results in Figure 4C, we conclude that the paxillin- Δ LD1 variant favors
440 CIP4/clathrin association and that paxillin- Δ LIM3-4 favors vinculin association. Using
441 this approach, we found that ectopic $PXN^{\Delta LIM3-4}$ expression in 0.1 kPa cultures
442 enhanced the neuritogenesis-delaying BL phenotype, whereas $PXN^{\Delta LD1}$ expression
443 reduced the BL population in 20 kPa cultures (Figure 7-figure supplement 1). By
444 contrast, ectopic expression of PXN^{LD1-3} , which cannot bind vinculin or CIP4, had no
445 significant effect on neurite outgrowth (Figure 7-figure supplement 1). These results
446 support the idea that whether paxillin forms a complex with either endocytic or adhesion
447 molecules determines the probability that newborn neurons will form proper neurites.

448 **Paxillin is required for neurite development *in vivo***

449 We next evaluated the effect of paxillin activity on neurite development *in vivo* by
450 monitoring the protein expression of endocytic factors in embryonic rat brain. We
451 observed high levels of endocytosis-related factors and low levels of adhesion-related
452 molecules in embryonic rat brains compared to hepatic and cardiac control tissues
453 (Figure 7– figure supplement 2). In addition, paxillin abundance increased between E13
454 and E18 and declined postnatally (between P1 and P14) in the developing cortex
455 (Figure 7– figure supplement 3). This time-course is compatible with and parallels that
456 of neurite formation in the developing rat brain.

457 Then, to assess the function of paxillin in neurite development *in vivo*, we
458 conducted in utero electroporation of paxillin shRNA (PXN-shRNAs) in a subpopulation
459 of neural progenitor cells at embryonic day 17 (E17). Because aberrant neurite
460 formation *in vivo* usually delays neuronal migration into the cortical plate (CP) (Hsu,
461 Guo et al., 2015), we analyzed E20 rat brain slices in which most cells (~75%) in control
462 embryos had migrated out of the subventricular zone (SVZ) with a radial infiltration into
463 the intermediate zone (IZ) towards the CP (Figure 7E, F). Neurons expressing paxillin-
464 shRNA showed apparent migration defects relative to controls, with ~42% of cells
465 accumulating in the SVZ, wherein ~25% of paxillin-knockdown neurons did not exhibit
466 neurite processes (Figure 7E, G). These phenotypes were rescued by co-expression of
467 shRNA-resistant PXN-R (Figure 7E-G).

468

469

470 Discussion

471 Neurite formation is the first morphogenetic step in establishing axonal projections and
472 dendritic territory. Under physiological environments *in vivo*, both genetic programs and
473 cell mechanics contribute to timely emergence of neuronal morphology and activity.
474 Nevertheless, it remains challenging to define spatio-temporal patterns of neurite
475 initiation and most studies to date have tackled this question using thin-glass or plastic
476 cell culture substrates in which cell-matrix adhesion is a prominent response. In the
477 present study, we used culture on soft substrates to demonstrate a paxillin-linked
478 bistable switch that governs the ability of newborn neurons to shift their lamellipodium
479 morphology to one of two stable states and to assume a neuritogenic state within a few
480 hours. Our system recapitulates temporal and morphologic features observed *in vivo*.
481 By contrast, when cells are grown on rigid substrates or when endocytosis is inhibited,
482 neurons adopt the behavior of most migratory cells and paxillin becomes associated
483 with cell-matrix or adhesion factors, exhibiting broad lamellipodia that delay neurite
484 formation. Such biphasic neurite initiation emerges from an amplification loop enabling
485 mutual inhibition of endocytosis by the adhesion machinery, and vice versa (Figure 7 H).
486 Through this mechanism, newborn neurons can respond to the soft environments that

487 dictate a phenotypic switch to allow neurite initiation. Our findings also complement
488 previous views of neurite formation defined by conventional Banker's culture on
489 coverslips.

490 To form protrusions from a cell body, cells must coordinate several distinct
491 intracellular mechanisms, including actin retrograde flow (Endo, Ohashi et al., 2003,
492 Flynn, Hellal et al., 2012), actomyosin-generated contractility (Amano, Chihara et al.,
493 1998, Raucher & Sheetz, 2000), membrane fusion and/or membrane tension (Fujita,
494 Koinuma et al., 2013, Zheng, Lamoureux et al., 1991), and exo- and endocytic
495 pathways (Raiborg, Wenzel et al., 2015). It is not surprising that paxillin is involved in
496 these processes, given its role as an integrator of integrin and growth factor signaling
497 (Brown & Turner, 2004). What is striking is our finding that paxillin plays a dual role in
498 adhesion and endocytosis, with predominance of one of these roles determining the fate
499 of a newborn neuron. Historically, paxillin has been known as a major player in cell-
500 matrix adhesions, where it associates with tyrosine kinases (such as FAK and Src) and
501 the actin-binding proteins vinculin and actopaxin (Brown et al., 1996, Brown & Turner,
502 2004, Nikolopoulos & Turner, 2000, Schaller, 2001, Turner, 2000). Our findings suggest
503 that on soft gels in particular, newborn neurons recruit paxillin to the endocytic
504 machinery (via binding with clathrin and CIP4) with a higher, but not exclusive,
505 preference over cell-matrix adhesions. Our microarray analysis indicates that selectively
506 elevated levels of endocytic factors may underlie their preferential recruitments with
507 paxillin observed in soft-gel cultures. This heretofore unknown behavior of paxillin then
508 elevates endocytic activity, Rac1 signaling, and expression of the genes encoding
509 endocytic proteins that are required for timely neurite emergence. As a result, a soft
510 environment with elasticity lower than 1 kPa is sufficient to induce timely neurite
511 initiation. Conversely, our observations suggest that culturing cells on rigid substrates,
512 disruption of Rac1 activation, and blockage of endocytosis all delay spontaneous
513 neurite initiation.

514 Proper functioning of neural networks depends on physical connections between
515 neurons, such as synapses, which in turn requires the capacity to control morphological
516 changes such as protrusion in the course of neuritogenesis. For most cells,

517 microenvironmental stiffness has been shown to promote cell spread and protrusion
518 (Discher, Janmey et al., 2005, Yeung, Georges et al., 2005). However, those same
519 environments may lead to formation of unnecessary connections in young neurons or
520 even promote deleterious “noise” that can interfere with neuronal function. The ability of
521 neonatal neurons to delay neuritogenesis on a rigid environment could endow cells with
522 the ability to establish robust and functional networks only in permissive environments
523 (i.e., soft microenvironments). While paxillin functions in endocytic reactions as opposed
524 to adhesion upon neurite initiation on soft substrates, endocytic accessory components
525 could have an unconventional role when endocytic signaling becomes compromised
526 under high cell-matrix adhesion regimes. For example, ectopically-expressed CIP4 has
527 been shown to accumulate at broad lamellipodia and to inhibit neurite formation on stiff
528 substrata (coverslips) (Saengsawang et al., 2012), where CIP4 may function in actin
529 polymerization rather than neuritogenic endosomal reactions.

530 Paxillin-associated endocytosis may also occur in epithelial cells, since both
531 epithelial cells and neurons are derived from ectoderm. In fact, in vitro experiments
532 demonstrate that proper development of epithelial organs requires soft
533 microenvironments, while stiff stroma is often observed in advanced cancers (Gilkes,
534 Semenza et al., 2014, Paszek, Zahir et al., 2005, Wirtz, Konstantopoulos et al., 2011).
535 By comparison, muscle cells, fibroblasts or osteoclasts, which are derived from other
536 germ layers, may exhibit higher tension or rigidity. Based on studies reporting the
537 natural stiffness of mouse embryonic cerebral cortex at E16.5 to E18.5 (Iwashita,
538 Kataoka et al., 2014), we surmise that a neuronal switch favoring paxillin/endocytic
539 factor binding is required and activated immediately after embryonic neuronal
540 differentiation to ensure timely neurite initiation. This switch may also promote departure
541 of cells from neurogenic regions, such as the ventricular and subventricular zones,
542 whose stiffness is relatively high compared to the cortical plate at E18.5. However, at a
543 later developmental time-point (since brain stiffness increases with age) and at synaptic
544 contact sites, the paxillin adhesion switch may predominate, allowing contacts with
545 postsynaptic cells or decreasing the capacity for neurite outgrowth. For example,
546 synapses at neuro-muscular junctions where repetitive muscle contraction can endow
547 much greater localized stiffness than that seen in brain cortex may favor

548 paxillin/adhesion machinery association. Furthermore, as shown here, the paxillin
549 adhesion switch relies on formation of adhesion complexes and consequently depends
550 on integrin signaling. In developing and adult brain, integrins play important roles in
551 controlling neuronal process outgrowth and regulating synaptic plasticity and memory
552 formation (reviewed in (Park & Goda, 2016)). However, the paxillin-mediated switch to
553 control timing of neurite initiation may not underlie morphogenetic events occurring at
554 later stages, as neuronal paxillin expression decreases as neurons mature. Therefore, it
555 will be important to revisit the relationship among genetic profiles, cellular reactions, and
556 tissue mechanical properties over different cell types and developmental stages.

557 Looking forward, our observations and our model for a molecular switch that is
558 integrated with changes in gene expression and the dual role of paxillin represent a
559 robust mechanism that could underlie synchronous behaviors, such as morphological
560 transformation or cohort migration, that occur when a group of developing cells is
561 exposed to diverse signals *in vivo*. Besides substrate stiffness, physiological constraints
562 imposed by other factors, such as cell-cell contact guidance or actin-microtubule
563 coupling efficiency, could play important roles in neurite formation. In addition to a
564 morphogenetic role, paxillin-associated endocytosis may also potentiate retrograde
565 relay of growth and survival signals deployed from the neuritic terminal (Cosker &
566 Segal, 2014) and thereby provide another mechanism to positively regulate neuronal
567 development.

568

569

570

571 **Materials and Methods**
572

Key Resources Table

Reagent type (species) or resource	Designation	Source or reference	Identifiers	Additional information
cell line	HEK293T	ATCC	ATCC Cat# CRL-3216, RRID:CVCL_0063	
antibody	anti-FLAG M2	Sigma-Aldrich	Sigma-Aldrich Cat# F1804, RRID:AB_262044	dilution: 1:1000
	c-Myc Tag Monoclonal Antibody (9E10)	Thermo Fisher Scientific	Thermo Fisher Scientific Cat# MA1-980, RRID:AB_558470	dilution: 1:1000
	Anti-beta III tubulin Antibody	Millipore	Millipore Cat# AB9354, RRID:AB_570918	dilution: 1:1000 in IF
	MAP2	Millipore; PMID:26244549	Millipore Cat# AB5622, RRID:AB_11213363	dilution: 1:1000 in IF
	actin	Millipore	Millipore Cat# MAB1501, RRID:AB_2223041	dilution: 1:2000
	Tau-1	Millipore	Millipore Cat# MAB3420, RRID:AB_94855	dilution: 1:1000 in IF
	Anti-Paxillin (N-Term), Rabbit Monoclonal, clone Y113 antibody	Millipore	Millipore Cat# 04-581, RRID:AB_838293	dilution: 1:1000 in WB; 1:200 in IF
	p-PaxillinY118	ECM Biosciences	ECM Biosciences Cat# PP4501	dilution: 1:1000
	Mouse Anti-Paxillin Monoclonal Antibody, Unconjugated, Clone 349	BD Biosciences; PMID:28362576	BD Biosciences Cat# 612405, RRID:AB_647289	dilution: 1:1000
	Anti-Vinculin, clone V284 antibody	millipore; PMID:28697342	Millipore Cat# 05-386, RRID:AB_309711	dilution: 1:1000 in WB; 1:200 in IF
	Anti-Integrin Beta1, activated, Clone HUTS-4, Azide Free antibody	Millipore; PMID:28602620	Millipore Cat# MAB2079Z, RRID:AB_2233964	dilution: 1:1000
	TRIP/CIP4	Bethyl Laboratories; A301-186A		dilution: 1:1000 in WB; 1:200 in IF
	Clathrin heavy chain antibody	Abcam; PMID:28231467, PMID:28575669	Abcam Cat# ab21679, RRID:AB_2083165	dilution: 1:1000 in WB; 1:200 in IF
	Talin 1 and 2 antibody [8D4]	Abcam	Abcam Cat# ab11188, RRID:AB_297828	dilution: 1:1000 in WB
	Rabbit Anti-Rab5 Polyclonal Antibody, Unconjugated	Abcam; PMID:28408870, PMID:28669519	Abcam Cat# ab18211, RRID:AB_470264	dilution: 1:1000 in WB
	Integrin beta 1 antibody [EP1041Y] - Carboxyterminal end	Abcam; PMID:25330147, PMID:28552668, PMID:28609658	Abcam Cat# ab52971, RRID:AB_870695	dilution: 1:1000 in WB; 1:200 in IF
	Phospho-FAK (Tyr397) Antibody (31H5L17), ABfinity(TM) Rabbit Monoclonal	Thermo Fisher Scientific; PMID:22049075, PMID:25280968, PMID:26056143, PMID:26381152, PMID:26393679, PMID:26984758	Thermo Fisher Scientific Cat# 700255, RRID:AB_2532307	dilution: 1:1000 in WB; 1:200 in IF
	Rabbit Anti-FAK [pY397] Polyclonal Antibodies, Unconjugated antibody	Thermo Fisher Scientific; PMID:27474796, PMID:28069919, PMID:28520937	Thermo Fisher Scientific Cat# 44-624G, RRID:AB_2533701	dilution: 1:1000 in WB; 1:200 in IF

	Akt1/2/3 (H-136) antibody	Santa Cruz Biotechnology ; PMID:27316329, PMID:27410235, PMID:28911175	Santa Cruz Biotechnology Cat# sc-8312, RRID:AB_671714	dilution: 1:200 in WB
	Rac 1 (C-11) antibody	Santa Cruz Biotechnology	Santa Cruz Biotechnology Cat# sc-95, RRID:AB_2176125	dilution: 1:200 in WB
	Cdc42 (P1) antibody	PMID:28181299, PMID:28457749	Santa Cruz Biotechnology Cat# sc-87, RRID:AB_631213	dilution: 1:200 in WB
	Rho A (26C4) antibody	Santa Cruz Biotechnology ; PMID:28287395, PMID:28323616	Santa Cruz Biotechnology Cat# sc-418, RRID:AB_628218	dilution: 1:200 in WB
	Anti-Active Rac1-GTP Mouse Monoclonal Antibody	NewEast Biosciences	NewEast Biosciences Cat# 26903, RRID:AB_1961793	dilution: 1:200 in WB and IF
	Anti-RhoA antibody (mouse MAb) + control	Cytoskeleton Inc; PMID:27822498	Cytoskeleton Cat# ARH03, RRID:AB_10708069	dilution: 1:200 in WB and IF
	Anti-Rac1 specific mouse MAb antibody	Cytoskeleton Inc	Cytoskeleton Cat# ARC03-A, RRID:AB_10709099	dilution: 1:200 in WB and IF
	Anti-Cdc42 Mouse Monoclonal Antibody	Cytoskeleton Inc	Cytoskeleton Cat# ACD03-A, RRID:AB_10716593	dilution: 1:200 in WB and IF
peptide, recombinant protein	PAK-GST, GST-Photekin-RBD	Cytoskeleton Inc	Cytoskeleton Inc Cat. #BK035 ; Cat. # BK036	

573
574
575

Plasmids

576 Plasmids used are as follows: fluorescence resonance energy transfer (FRET) reporters for
577 Rac1 activity assays, Rac1-2G (Plasmid #66111; (Fritz et al., 2013), GFP-Dynamin 2 K44A
578 (Plasmid #22301;(Ochoa, Slepnev et al., 2000) and paxillin-pEGFP plasmid (Plasmid # 15233;
579 (Laukaitis, Webb et al., 2001) were obtained from Addgene. Lentiviral transfer plasmid pLenti-C-
580 Myc-DDK-CIP4 (also known as TRIP10) was generated by subcloning the C-Myc-DDK-CIP4
581 fragment from pCMV-C-Myc-DDK-TRIP10 (OriGene Technologies, Rockville, MD) into pLenti
582 vector using AsiSI and PmeI restriction sites. GST- or His-tagged fusion protein expression
583 constructs encoding full-length or truncated versions of paxillin or CIP4 were cloned into
584 pDONR/Zeo vectors (Invitrogen, Carlsbad, CA) by PCR-based methods and transferred to T7
585 promoter-driven pDEST15 or pEXP2-6xHis-DEST Gateway destination vectors (Invitrogen,
586 Carlsbad, CA) by recombination-based Gateway technology according to the manufacturer's
587 protocols (Invitrogen, Carlsbad, CA). Paxillin-mCherry plasmid was generated by replacing the
588 EGFP fragment from paxillin-pEGFP with the mCherry sequence. Lentiviral-based short hairpin
589 RNA (shRNA) constructs were purchased from OriGene Technologies (Rockville, MD). For
590 paxillin shRNA constructs, 29-oligonucleotide duplexes targeting rat paxillin cDNA sequences
591 (PXN-shRNA A targeting position 1505, PXN-shRNA B targeting position 1571, PXN-shRNA C
592 targeting position 346, and PXN-shRNA D targeting position 952 of the corresponding paxillin
593 sequence) and a control non-effective scrambled shRNA cassette (5'-
594 CACAAGCTGGAGTACAACACTACAACAGCCA-3') were cloned into pGFP-C-shLenti vector
595 (OriGene Technologies, Rockville, MD). For CIP4 shRNA constructs, TRIP10-shRNA A targeting
596 position 172, TRIP10-shRNA B targeting position 351, TRIP10-shRNA C targeting position 811,
597 and TRIP10-shRNA D targeting position 983 of the corresponding CIP4 coding sequence were
598 also cloned into pGFP-C-shLenti vector (OriGene Technologies, Rockville, MD). The encoding
599 regions of shRNAs contained a 29-nucleotide sense strand, a TCAAGAG loop structure, and
600 the reverse complementary sequence, followed by a TTTTTT termination sequence. The
601 chicken ortholog of a mammalian paxillin expression plasmid, paxillin-pEGFP, was used as the
602 shRNA-resistant construct (PXN-shRNA-R), the sequence of which is resistant to PXN-shRNA

603 targeting. pLenti-C-mGFP-PXN (rat paxillin) was purchased from OriGene Technologies
604 (Rockville, MD). The plasmid encoding mCherry-TrkB used in QD-BDNF internalization assays
605 was kindly provided by Dr. Mu-Ming Poo, UC Berkeley, USA.

606

607

608 **Reagents**

609 Sources of antibodies, proteins, and chemicals are as follows. Purified PAK-GST and GST-
610 Rhotekin-RBD for active Rac1 and RhoA pulldown assays were from Cytoskeleton Inc. (Denver,
611 CO). Primary antibodies: monoclonal anti-FLAG M2 was from Sigma-Aldrich (Saint Louis, MO).
612 Polyclonal antibodies to neuronal class III β -tubulin (Tuj-1, AB9354) and MAP2 (AB5622), as
613 well as monoclonal antibodies to actin (clone C4, MAB1501), Tau-1 (clone PC1C6, MAB3420),
614 paxillin (N-term, 04-581), vinculin (clone V284, 05-386) and activated integrin β 1 (clone HUTS-
615 4, MAB 2079Z) were from EMD Millipore Corp. (Billerica, MA). Polyclonal antibodies to
616 TRIP/CIP4 (A301-186A). was from Bethyl Laboratories, Inc. (Montgomery, TX). Clathrin heavy
617 chain (ab21679), Rab5 (ab18211), and monoclonal antibodies to integrin β 1 (ab52971) and talin
618 1/2 (ab11188) were from Abcam Inc. (Cambridge, MA). Polyclonal antibody to p-FAK^{Y397} (44-
619 624G) and monoclonal antibody to p-FAK^{Y397} (700255) were from Thermo Fisher Scientific.
620 Polyclonal antibody to p-Paxillin^{Y118} (PP4501) was from ECM Biosciences (Versailles, KY).
621 Monoclonal antibody to paxillin (612405) was from BD Biosciences (Franklin Lakes, NJ).
622 Polyclonal antibodies to Akt1/2/3 (H-136), Rac1 (C-11, sc-95), Cdc42 (P1, sc-87), as well as
623 monoclonal antibody to RhoA (26C4, sc-418), were from Santa Cruz Biotechnology (Santa
624 Cruz, CA). Monoclonal antibody to c-Myc (9E10, MA1-980) was from Thermo Scientific
625 (Waltham, MA). Monoclonal antibody to active Rac1-GTP (26903) was from NewEast
626 Biosciences (King of Prussia, PA). Monoclonal antibodies to RhoA (ARH03), Rac1 (ARC03) and
627 Cdc42 (ACD03) were from Cytoskeleton Inc. (Denver, CO).

628 Pharmacological reagents: recombinant human BDNF was from PeproTech (Rocky Hill, NJ).
629 PP2 (Src and RIP2 kinase inhibitor, ab120308), Dynole[®] 2-24 (potent dynamin I and II inhibitor;
630 ab141290), and Dyngo[®] 4a (ab120689; highly potent dynamin inhibitor) were purchased from
631 Abcam Inc. (Cambridge, MA). Actinomycin D (A9415), dynasore (D7693) and dansylcadaverine
632 (also described as monodansyl cadaverine (MDC), 30432) were purchased from Sigma Aldrich
633 (Saint Louis, MO). PD150606 (1269) and NSC23766 (2161) were purchased from Tocris
634 Bioscience (Ellisville, MO). LY 294002 (440202) and Y-27632 (SCM075) were bought from EMD
635 Millipore Corp. (Billerica, MA).

636 Fluorescent reagents: Alexa Fluor 488, Alexa Fluor 546, Alexa Fluor 647, fluorescent dye FM1-
637 43FX (F35355) and FM4-64FX (F34653) were from Invitrogen (Carlsbad, CA). DAPI (D9542),
638 Acrylamide (A4058) and N'-N'-methylenebisacrylamide solution (M1533) were purchased from
639 Sigma-Aldrich (Saint Louis, MO). Phalloidin-*iflour* 488 conjugate, phalloidin-*iflour* 555 conjugate
640 and phalloidin-*iflour* 647 conjugate were from AAT Bioquest Inc. (Sunnyvale, CA).

641

642 **Cell culture, protein lysate preparations, and immunostaining**

643 Hippocampal neurons were prepared from E17.5 rat embryos as previously described (Dotti
644 et al., 1988), and were cultured in neurobasal medium supplemented with Gem21 NeuroPlex[™]
645 (GEMINI bio-products, West Sacramento, CA). A similar procedure was applied to preparation
646 of cortical neuronal cultures. Human Embryonic Kidney 293T (HEK293T; ATCC Cat# CRL-
647 3216) cells used for biochemical assays were tested for Mycoplasma and characterized by STR
648 profiling as indicated in the ATCC online catalog. HEK293T cells were cultured in Dulbecco's
649 Modified Eagle's Medium supplemented with 10% fetal bovine serum (Biological Industries, Beit

650 Haemek, Israel). Transfection of these cultures was performed using a lentivirus-based
651 expression system or Lipofectamine™ 2000 (Invitrogen, Carlsbad, CA), according to the
652 manufacturer's instructions. Unless otherwise stated, hippocampal neurons were used as a
653 standard model for in vitro immunocytochemistry to analyze neuronal morphology. Cortical
654 neuronal cultures were used to obtain a sufficient number of cells for biochemical assays not
655 requiring transfection of exogenous proteins.

656 For cortical neurons grown on gel or glass substrates, protein lysate was harvested in RIPA
657 buffer (Sigma Aldrich, St. Louis, MO) containing complete protease inhibitor cocktail (Roche,
658 BASEL, Switzerland) and phosphate inhibitor PhosSTOP (Roche, BASEL, Switzerland). For
659 tissue lysate preparations, brain and heart were dissected out from E17.5 rat embryos and
660 rinsed briefly with PBS, followed by tissue homogenization using a pestle in ice-cold lysis buffer
661 (20 mM Tris-HCl, 5 mM MgCl₂ and 1 mM DTT), followed by four rounds of sonication (20
662 seconds on followed by 10 seconds off). For other biochemical experiments, cell lysates were
663 prepared by the freeze-thaw method.

664 For immunostaining, cultured hippocampal neurons were fixed with 4% paraformaldehyde for
665 12 min and then permeabilized in 0.3% Triton X-100 for 12 min and blocked with 3% BSA for 1
666 hr. The fixed cells were processed further for immunostaining according to standard procedures
667 and imaged with a confocal microscope (Zeiss LSM700) equipped with a 63× oil-immersion
668 objective (NA1.4; Zeiss) and a 40× water-immersion objective (NA1.1; Zeiss). For quantitative
669 measurements of colocalization, images were acquired using a Zeiss LSM880 confocal
670 microscope with an Airyscan module (32-channel GaAsP detector array) equipped with a Plan
671 Apo 63× oil-immersion objective (NA1.4). The axial step size was set to 125 nm. Surface
672 rendering of the three-dimensional images was performed using ZEN (Zeiss) and Imaris
673 (Bitplane) software without Z-correction. Images were analyzed and processed for presentation
674 in the figures, using brightness and contrast adjustments with NIH ImageJ software and
675 following the guidelines of Rossner and Yamada (Rossner & Yamada, 2004).

676
677

678 **Polyacrylamide gel preparation**

679 Fabrication of polyacrylamide gels with tunable mechanical stiffness was slightly modified from
680 a previous protocol (Tse & Engler, 2010). Briefly, uniform polyacrylamide gels were fabricated in
681 a three-layer assembly of 200 μm thickness. The bottom layer was a hydrophilic amino-silanized
682 coverslip prepared according to the following protocol. A thin film of sodium hydroxide was
683 allowed to form on the coverslips at approximately 90°C. The entire surface of each coverslip
684 was then immersed with a sufficient volume of (3-aminopropyl) triethoxysilane (Sigma-Aldrich,
685 Saint Louis, MO) for 5 min. The (3-aminopropyl) triethoxysilane was then completely rinsed off
686 to prevent precipitation before 0.5% (v/v) glutaraldehyde (Sigma-Aldrich, Saint Louis, MO) in
687 PBS was added onto the silanized coverslips for 30 min. Fluids were removed by suction before
688 the amino-silanized coverslips were air-dried and sterilized with 70% ethanol for 16 hours prior
689 to gel preparation. The top layer comprised a laminin-coated coverslip prepared by sterilizing an
690 acid-washed coverslip with 70% ethanol and then coating it with 5 μg/ml of poly-L-Lysine
691 (Sigma Aldrich, Saint Louis, MO) and 0.08 μg/ml of laminin (Corning, NY) by absorption for an
692 hour at 37°C.

693 For the middle gel layers of differing stiffness, a prepolymer mixture was prepared as shown in
694 the table below. Polymerization of the prepolymer mixture was carried out by adding 10 μl of
695 10% ammonium persulfate, 2 μl of TEMED (Bio-Rad Laboratories, Hercules, CA) and sufficient
696 deionized water to yield a final volume of 1000 μl. The resulting prepolymer-catalyst mixture was
697 dropped onto hydrophobic amino-silanized coverslips. The three-layer assembly was formed by

698 transferring the pre-coated poly-L-Lysine and laminin coverslips to the surfaces of the
 699 polyacrylamide gels during polymerization. After 30 minutes, the top layer was gently peeled off
 700 and washed three times with HEPES solution to remove unreacted monomer and excess
 701 coatings.
 702

	4% acrylamide (μl)	2%N'-N'-methylenebisacrylamide (μl)	deionized water (μl)
0.1 kPa	75	25	900
1 kPa	100	50	850
20 kPa	200	240	560

703

704 **Substrate elasticity measurements**

705 Substrate elasticity of uniform gels was measured by using a JPK NanoWizard® II AFM system
 706 installed above the stage of an inverted light microscope (Zeiss Axio Observer) in a custom-built
 707 anti-noise, anti-vibration system. A 5 μm (in diameter) polystyrene bead-modified tip-less
 708 cantilever (ARROW-TL1-50, NanoWorld, US) was utilized. The spring constants, calibrated by a
 709 thermal noise-based method, were at a range of 0.02 to 0.08 N/m for all cantilevers. All
 710 indentation depth curves were calculated using the manufacturer's software (Hertz model, JPK
 711 instruments, Berlin, Germany). The average value of Young's modulus of tensile elasticity was
 712 acquired from 25 measurements for each independent experiment.

713

714 **Phalloidin intensity profiling**

715 Images of 5 hr neuronal cultures stained with phalloidin were analyzed in a circular coordinate
 716 system using an oval-profile ImageJ plugin (courtesy of Bill O'Connell,
 717 <http://rsbweb.nih.gov/ij/plugins/oval-profile.html>). The pixel intensities along each radian in a
 718 circle (radius=8 μm) covering the cell periphery were normalized against the background value
 719 and plotted as an intensity-distribution profile. The lamellipodium occupancy (LO) refers to the
 720 proportion of the individual phalloidin arc length (angular span) to the entire cell periphery ($2\pi r$),
 721 calculated by the formula $\frac{\text{phalloidin arc length}}{2\pi r}$. The major LO represents the maximum LO value of
 722 each cell.

723

724 **Single molecule FISH**

725 Neurons grown on gel or glass substrates were fixed in 4% paraformaldehyde at room
 726 temperature for 10 min, and then permeabilized in 0.3% Triton X-100 for 12 min and rinsed in
 727 70% ethanol for subsequent RNA FISH. For hybridization, samples were briefly washed once
 728 with wash buffer (10% deionized formamide, 2 × SSC) for 5 min, and then hybridized with RNA
 729 FISH probes in hybridization buffer (10% formamide, 10% dextran sulfate, 2× SSC) overnight at
 730 37 °C. Following hybridization, samples were washed twice with wash buffer (30 min per wash),
 731 and washed once with 1× PBS. Samples were then imaged with a Delta Vision microscopy
 732 system equipped with a PlanApoN 60X oil-immersion objective (1.42 NA; Olympus). Images
 733 were collected and analyzed with NIH Image software. Alexa Fluor 488 phalloidin was used to
 734 identify the lamellipodium phenotypes of the stained cells. smRISH probe sets targeting the rat
 735 transcripts of *CLTC*, *MYO6*, *DAB2*, *VCL*, *CDH11*, *ROBO2*, *DKK1*, and *CYR61* were ordered
 736 from Stellaris with Quasar 570 dye (Bioserach Technologies, Petaluma, USA).

737

738 **FRET imaging and analysis**

739 Cultured hippocampal neurons were imaged with a Rolera EM-C² EMCCD camera (QImaging)
740 and Yokogawa CSU-X1 spinning-disk confocal microscopy (Zeiss) and a 40× water-immersion
741 objective (NA1.1; Zeiss). Excitation spectra were excited by a solid-state 445 nm diode laser,
742 through a 457-nm dichroic filter. Emission spectra were sequentially acquired using 485 ± 20 nm
743 and 535±30 nm band-pass emission filters for mTFP1 and Venus fluorescence, respectively.
744 Images were collected and analyzed with NIH ImageJ software. All filters and dichroics were
745 from Chroma Technology. Live images were acquired for 150 milliseconds at 3-second intervals.
746 The intensity of mTFP1 and Venus fluorescence was measured at a level below saturation for
747 all neurites. Measurements were not performed on the soma due to fluorescence saturation
748 being at the excitation level suitable for neurite measurements. For the ratiometric FRET
749 analysis, the mTFP1 and Venus signals were background-subtracted (with background intensity
750 taken from a nearby cell-free region), normalized against the control value (averaged over 3
751 minutes), and the FRET value was calculated as a ratio (mTFP1/Venus). The intensity of the
752 FRET signal was calculated with NIH ImageJ software and is represented by pseudocolors.

753

754 **Expression of GST- and His-tagged proteins, and *in vitro* binding assays**

755 For protein expression and purification, GST fusion proteins were produced as previously
756 described. Briefly, GST- or His-tagged proteins were expressed in *E. coli* BL21(DE3) induced by
757 0.4 mM IPTG overnight at 30 °C in LB medium. Bacteria were lysed by sonication in short
758 pulses of 15 seconds in lysis buffer [(50mM Tris-HCl, pH=7.4, 50mM NaCl, 5mM DTT, 1mM
759 phenylmethylsulfonyl fluoride, 1% Triton X-100 containing 1% Triton X-100, 1 mM EDTA, 1 mM
760 dithiothreitol and protease inhibitors (Complete EDTA-free; Roche)]. Cell debris was removed by
761 centrifugation at 9000 *g* for 10 min at 4 °C. The resulting supernatant was applied onto a
762 Glutathione Sepharose™ 4B or HisTrap column (GE Healthcare). After washing, GST- and His-
763 tagged proteins were eluted in buffer containing 10 mM reduced glutathione and 300 mM
764 imidazole, respectively. We added 1 M imidazole to samples shortly after elution to prevent
765 precipitation of His-tagged protein. Protein concentrations were measured using the Bio-Rad
766 DC Protein Assay. Protein purity was further assessed by fast protein liquid chromatography,
767 followed by SDS- PAGE and Coomassie blue staining.

768

769 For GST pull-down assays, cell lysate/His-tagged protein and GST fusion proteins were
770 incubated together with glutathione-agarose beads. Complexes recovered from the beads were
771 resolved by SDS-PAGE and analyzed by Western blotting.

772

773 **FM4-64 dye imaging**

774 Hippocampal neurons grown on various substrates were starved in neurobasal medium for 30
775 minutes and transferred to extracellular solution (145 mM NaCl, 10 mM HEPES, 8 mM glucose,
776 3 mM CaCl₂, 2 mM MgCl₂ and 3 mM KCl) before loading with the fluorescent dye FM® 4-64FX
777 (Invitrogen, Carlsbad, CA). Time-lapse images of neurons loaded with 20 μM FM4-64 were
778 acquired as 10 μm z-series stacks (spaced at 0.5 μm) at 2 min intervals for 40 min using
779 Yokogawa CSU-X1 spinning-disk confocal microscopy (Zeiss). Image analysis of FM dye
780 intensity of the region of interest in cell bodies was performed by NIH ImageJ software. All
781 pictures were taken at equal exposure for control and experimental groups.

782

783 **Measurements of QD-BDNF internalization**

784 Quantum dot-labeled BDNF (QD-BDNF) was prepared as previously described (Xie, Zhang et
785 al., 2012). Briefly, streptavidin-conjugated QD655 (Invitrogen, Carlsbad, CA) mixed with human
786 BDNF-biotin (Alomone Labs, Jerusalem, Israel) at a molar ratio of 1:2 was incubated overnight
787 at 4 °C. Unbound BDNF was separated from QD-BDNF with Sephacryl S-300 HR beads
788 (Sigma-Aldrich, Saint Louis, MO), and the elution fractions (in 20 mM HEPES buffer, pH 7.2)
789 with the highest fluorescence were regarded as the purified QD-BDNF. HEK293T cells
790 transfected with TrkB expression constructs or hippocampal neurons were exposed to 0.1 nM
791 QD-BDNF in 2% BSA containing extracellular solution for 30 min, followed by a period of
792 washout before image acquisition. The fluorescence images of internalized QD-BDNF were
793 acquired by spinning-disk confocal microscopy (Zeiss, multiple emission set: E460 SPUVv2,
794 EX; 475DCXRU dichroic mirror, BS; D655/40m, EM) in the presence of the quencher QSY-21 (2
795 μ M) to prevent signals of extracellular QD-BDNF. We quantified amounts of BDNF-Qdots taken
796 up by cells and correlated them with TrkB expression in transfected cells. BDNF-Qdot uptake by
797 HEK293T cells requires TrkB expression, but TrkB levels do not show a linear correlation with
798 numbers of intracellular BDNF-Qdots. Based on TrkB levels seen in our experiments, the
799 amount of receptor is already saturating and sufficient to accurately assess BDNF-Qdot uptake
800 by HEK293T cells. We omitted analysis of cells whose TrkB intensity is relatively low (cut-off =
801 5% of highest TrkB intensity in each group). This adjustment does not alter overall observation
802 that loss of paxillin expression significantly reduces BDNF-Qdot uptake.

803

804 **cdNA microarray and data validations**

805 Total RNA of cortical neurons growing on gels of differing stiffness and glass was extracted at
806 different time-points using a QuickGene RNA cultured cell kit from Kurabo Industries Ltd.
807 (Osaka, Tokyo). RNA concentrations were quantified using a NanoDrop Spectrophotometer ND-
808 1000 (NanoDrop Technologies, Wilmington, ED). RNA quality was assessed using a 2100
809 Bioanalyzer (Agilent Technologies, Santa Clara, CA) based on the following criteria: RNA
810 integrity (number) >8.0, rRNA ratio (28S/18S) >1.8, and the proportion of 28S and 18S (amount)
811 >40%. cDNA probe labeling and hybridization on rat gene expression microarray slides (Agilent
812 Technologies, Santa Clara, CA) was conducted according to the manufacturers' protocols and
813 carried out in the Institute of Molecular Biology Genomics Core Facility. Microarray data (19956
814 entrez genes) were analyzed using GeneSpring GX software (version 12.1, Agilent). In brief,
815 gene expression levels were subjected to quantile normalization and averaged from three
816 independent experiments. Gene modules of the differential expressions were identified using a
817 volcano plot (filtering criteria: >1.5-fold change, $p < 0.05$, t test), followed by Gene Ontology
818 analysis (cut off: $p < 0.02$; Appendix-Table 1). Validation of results was achieved by overlaying
819 the microarray-identified genes with a global molecular network (the IPA knowledge base),
820 which revealed that the 114 genes were eligible to generate networks with a p -value <0.02. We
821 prioritized the 114 genes based on their significance (p -value), and "endocytosis-related
822 reaction" came out as the top-ranked GO term for molecular functions among genes in the list.
823 Three out of 37 genes that were selectively upregulated in 5 hr 0.1kPa cultures are directly
824 linked to endocytic processes. Based on significant shared GO terms, the correlations between
825 the stiffness of substrates and the expression levels of genes associated with endocytosis,
826 adhesion, neuronal development and cytoskeleton (see Appendix-Table 2) were further verified
827 by using QuantiGene Plex 2.0 assays according to the manufacturer's instructions (Affymetrix,
828 Santa Clara, CA). The two housekeeping genes, GAPDH and HPRT, were used for data
829 normalization. GEO accession number of the microarray data set is GSE102350.

830

831 **In utero electroporation**

832 In utero electroporation followed previously described procedures (Saito & Nakatsuji, 2001),
833 with minor modifications. Timed-pregnant Sprague-Dawley rats were anesthetized at E17.5 with
834 isoflurane, and the uterine horns were exposed by way of a laparotomy. Saline solution
835 containing the expression plasmid of interest (2 mg/ml) together with the dye Fast Green
836 (0.3 mg/ml; Sigma-Aldrich, Saint Louis, MO) was injected (1–2 μ l) through the uterine wall into
837 one of the lateral ventricles of the embryos. The embryo's head was electroporated by tweezer-
838 type circular electrodes across the uterus wall, and five electrical pulses (50 V, 50 ms duration at
839 100 ms intervals) were delivered with a square-wave electroporation generator (model ECM
840 830, BTX Inc.). The uterine horns were then returned to the abdominal cavity, the wall and skin
841 were sutured, and the embryos continued normal development. Control embryos were
842 electroporated with the tdTomato construct together with the GFP construct (1:2 ratio), and
843 experimental embryos were electroporated with DynII^{K44A} or PXN-shRNA (both sequence C and
844 D) (see also Supplemental Materials), control scramble-shRNA, and the shRNA-resistant
845 construct (PXN-shRNA-R), each in addition to the tdTomato construct. Control and experimental
846 E20 embryos were obtained from the same litter and the injections were always made into the
847 left and right ventricles, respectively, for later identification. Maximum intensities of the z-
848 projection of tile images (20 μ m thickness) were attained from spinning-disk confocal
849 microscopy (Zeiss). Animal protocols were approved by the Animal Care and Use Committee of
850 Academia Sinica.

851

852 **Membrane floatation assay**

853 Dissected embryonic rat brain and heart at E17.5 were sonicated (four cycles of 20 seconds on
854 and 10 seconds off) and mixed with 90% (w/w) sucrose to a final concentration of 45% sucrose
855 in detergent-free lysis buffer (20 mM Tris-HCl, 5 mM MgCl₂ and 1 mM DTT with Complete
856 protease inhibitor). Samples (1.5 ml) were overlaid with 1.5 ml of 35% sucrose and 9 ml of 5%
857 sucrose and centrifuged at 175,000 x *g* for 18 h at 4°C. Fractions (300 μ l each) were collected
858 from the top and subjected to immunoblot analysis.

859

860 **Statistical analysis**

861 To choose the statistical test for comparisons between two datasets, we first examined whether
862 the data in each set was normally distributed using a Jarque-Bera test. A *t* test was used for
863 normally distributed datasets. One-way ANOVA followed by a Dunnett's post hoc *test* was used
864 for comparisons involving multiple datasets.

865

866

867 **Acknowledgments**

868 We thank Hwai-Jong Cheng for discussions and critical reading of the manuscript. We thank R.
869 Thakar, S. Li, M. Nasir, and D. Liepmann (University of California, Berkeley, CA) for help with
870 PDMS microfluidic molds for making patterned substrates. We thank the Research Center for
871 Applied Sciences, Academia Sinica, for help on atomic force microscopy measurements. We
872 thank the IBC Mass Spectrometry Facilities (Institute of Biological Chemistry, Academia Sinica)
873 for help with LTQ-Orbitrap data acquisition and additional technical assistance. We thank the
874 IMB Genomics Core Facilities (Institute of Molecular Biology, Academia Sinica) for microarray
875 analysis. This work was supported in part by a grant from the Ministry of Science and
876 Technology of Taiwan.

877

878

879

880 References

- 881 Amano M, Chihara K, Nakamura N, Fukata Y, Yano T, Shibata M, Ikebe M, Kaibuchi K (1998)
882 Myosin II activation promotes neurite retraction during the action of Rho and Rho-kinase.
883 *Genes Cells* 3: 177-88
- 884 Aoki K, Nakamura T, Matsuda M (2004) Spatio-temporal regulation of Rac1 and Cdc42
885 activity during nerve growth factor-induced neurite outgrowth in PC12 cells. *J Biol Chem*
886 279: 713-9
- 887 Aragona M, Panciera T, Manfrin A, Giulitti S, Michielin F, Elvassore N, Dupont S, Piccolo S
888 (2013) A mechanical checkpoint controls multicellular growth through YAP/TAZ regulation
889 by actin-processing factors. *Cell* 154: 1047-59
- 890 Balgude AP, Yu X, Szymanski A, Bellamkonda RV (2001) Agarose gel stiffness determines
891 rate of DRG neurite extension in 3D cultures. *Biomaterials* 22: 1077-84
- 892 Brown MC, Perrotta JA, Turner CE (1996) Identification of LIM3 as the principal
893 determinant of paxillin focal adhesion localization and characterization of a novel motif on
894 paxillin directing vinculin and focal adhesion kinase binding. *J Cell Biol* 135: 1109-23
- 895 Brown MC, Perrotta JA, Turner CE (1998) Serine and threonine phosphorylation of the
896 paxillin LIM domains regulates paxillin focal adhesion localization and cell adhesion to
897 fibronectin. *Mol Biol Cell* 9: 1803-16
- 898 Brown MC, Turner CE (2004) Paxillin: adapting to change. *Physiol Rev* 84: 1315-39
- 899 Carisey A, Tsang R, Greiner AM, Nijenhuis N, Heath N, Nazgiewicz A, Kemkemer R, Derby B,
900 Spatz J, Ballestrem C (2013) Vinculin regulates the recruitment and release of core focal
901 adhesion proteins in a force-dependent manner. *Curr Biol* 23: 271-81
- 902 Caswell PT, Chan M, Lindsay AJ, McCaffrey MW, Boettiger D, Norman JC (2008) Rab-coupling
903 protein coordinates recycling of alpha5beta1 integrin and EGFR1 to promote cell migration
904 in 3D microenvironments. *J Cell Biol* 183: 143-55
- 905 Christ AF, Franze K, Gautier H, Moshayedi P, Fawcett J, Franklin RJ, Karadottir RT, Guck J
906 (2010) Mechanical difference between white and gray matter in the rat cerebellum
907 measured by scanning force microscopy. *J Biomech* 43: 2986-92
- 908 Conner SD, Schmid SL (2002) Identification of an adaptor-associated kinase, AAK1, as a
909 regulator of clathrin-mediated endocytosis. *J Cell Biol* 156: 921-9
- 910 Cosker KE, Segal RA (2014) Neuronal signaling through endocytosis. *Cold Spring Harb*
911 *Perspect Biol* 6
- 912 Da Silva JS, Medina M, Zuliani C, Di Nardo A, Witke W, Dotti CG (2003) RhoA/ROCK
913 regulation of neuritogenesis via profilin IIA-mediated control of actin stability. *J Cell Biol*
914 162: 1267-79
- 915 Damke H, Baba T, Warnock DE, Schmid SL (1994) Induction of mutant dynamin specifically
916 blocks endocytic coated vesicle formation. *J Cell Biol* 127: 915-34
- 917 Dehmelt L, Smart FM, Ozer RS, Halpain S (2003) The role of microtubule-associated protein
918 2c in the reorganization of microtubules and lamellipodia during neurite initiation. *J*
919 *Neurosci* 23: 9479-90
- 920 Desmouliere A, Chaponnier C, Gabbiani G (2005) Tissue repair, contraction, and the
921 myofibroblast. *Wound Repair Regen* 13: 7-12
- 922 Discher DE, Janmey P, Wang YL (2005) Tissue cells feel and respond to the stiffness of their
923 substrate. *Science* 310: 1139-43

924 Du J, Chen X, Liang X, Zhang G, Xu J, He L, Zhan Q, Feng XQ, Chien S, Yang C (2011) Integrin
 925 activation and internalization on soft ECM as a mechanism of induction of stem cell
 926 differentiation by ECM elasticity. *Proc Natl Acad Sci U S A* 108: 9466-71
 927 Dumbauld DW, Lee TT, Singh A, Scrimgeour J, Gersbach CA, Zamir EA, Fu J, Chen CS, Curtis
 928 JE, Craig SW, Garcia AJ (2013) How vinculin regulates force transmission. *Proc Natl Acad Sci*
 929 *U S A* 110: 9788-93
 930 Dupont S, Morsut L, Aragona M, Enzo E, Giulitti S, Cordenonsi M, Zanconato F, Le Digabel J,
 931 Forcato M, Bicciato S, Elvassore N, Piccolo S (2011) Role of YAP/TAZ in
 932 mechanotransduction. *Nature* 474: 179-83
 933 Duran MB, Rahman A, Colten M, Brazill D (2009) Dictyostelium discoideum paxillin
 934 regulates actin-based processes. *Protist* 160: 221-32
 935 Endo M, Ohashi K, Sasaki Y, Goshima Y, Niwa R, Uemura T, Mizuno K (2003) Control of
 936 growth cone motility and morphology by LIM kinase and Slingshot via phosphorylation and
 937 dephosphorylation of cofilin. *J Neurosci* 23: 2527-37
 938 Engler AJ, Sen S, Sweeney HL, Discher DE (2006) Matrix elasticity directs stem cell lineage
 939 specification. *Cell* 126: 677-89
 940 Fawcett JW, Barker RA, Dunnett SB (1995) Dopaminergic neuronal survival and the effects
 941 of bFGF in explant, three dimensional and monolayer cultures of embryonic rat ventral
 942 mesencephalon. *Exp Brain Res* 106: 275-82
 943 Ferrell JE, Jr. (2002) Self-perpetuating states in signal transduction: positive feedback,
 944 double-negative feedback and bistability. *Curr Opin Cell Biol* 14: 140-8
 945 Flynn KC, Hellal F, Neukirchen D, Jacob S, Tahirovic S, Dupraz S, Stern S, Garvalov BK,
 946 Gurniak C, Shaw AE, Meyn L, Wedlich-Soldner R, Bamburg JR, Small JV, Witke W, Bradke F
 947 (2012) ADF/cofilin-mediated actin retrograde flow directs neurite formation in the
 948 developing brain. *Neuron* 76: 1091-107
 949 Fritz RD, Letzelter M, Reimann A, Martin K, Fusco L, Ritsma L, Ponsioen B, Fluri E, Schulte-
 950 Merker S, van Rheenen J, Pertz O (2013) A versatile toolkit to produce sensitive FRET
 951 biosensors to visualize signaling in time and space. *Sci Signal* 6: rs12
 952 Fritz RD, Menshykau D, Martin K, Reimann A, Pontelli V, Pertz O (2015) SrGAP2-Dependent
 953 Integration of Membrane Geometry and Slit-Robo-Repulsive Cues Regulates Fibroblast
 954 Contact Inhibition of Locomotion. *Dev Cell* 35: 78-92
 955 Fujita A, Koinuma S, Yasuda S, Nagai H, Kamiguchi H, Wada N, Nakamura T (2013) GTP
 956 hydrolysis of TC10 promotes neurite outgrowth through exocytic fusion of Rab11- and L1-
 957 containing vesicles by releasing exocyst component Exo70. *PLoS One* 8: e79689
 958 Georges PC, Miller WJ, Meaney DF, Sawyer ES, Janmey PA (2006) Matrices with Compliance
 959 Comparable to that of Brain Tissue Select Neuronal over Glial Growth in Mixed Cortical
 960 Cultures. *Biophysical Journal* 90: 3012-3018
 961 Gilkes DM, Semenza GL, Wirtz D (2014) Hypoxia and the extracellular matrix: drivers of
 962 tumour metastasis. *Nat Rev Cancer* 14: 430-9
 963 Govek EE, Newey SE, Van Aelst L (2005) The role of the Rho GTPases in neuronal
 964 development. *Genes Dev* 19: 1-49
 965 Guilluy C, Garcia-Mata R, Burridge K (2011) Rho protein crosstalk: another social network?
 966 *Trends Cell Biol* 21: 718-26
 967 Hall A (1998) Rho GTPases and the actin cytoskeleton. *Science* 279: 509-14
 968 Herskovits JS, Burgess CC, Obar RA, Vallee RB (1993) Effects of mutant rat dynamin on
 969 endocytosis. *J Cell Biol* 122: 565-78

970 Hsu MT, Guo CL, Liou AY, Chang TY, Ng MC, Florea BI, Overkleeft HS, Wu YL, Liao JC, Cheng
 971 PL (2015) Stage-Dependent Axon Transport of Proteasomes Contributes to Axon
 972 Development. *Dev Cell* 35: 418-31
 973 Humphries JD, Wang P, Streuli C, Geiger B, Humphries MJ, Ballestrem C (2007) Vinculin
 974 controls focal adhesion formation by direct interactions with talin and actin. *J Cell Biol* 179:
 975 1043-57
 976 Itofusa R, Kamiguchi H (2011) Polarizing membrane dynamics and adhesion for growth
 977 cone navigation. *Mol Cell Neurosci* 48: 332-8
 978 Iwashita M, Kataoka N, Toida K, Kosodo Y (2014) Systematic profiling of spatiotemporal
 979 tissue and cellular stiffness in the developing brain. *Development* 141: 3793-8
 980 Koser DE, Thompson AJ, Foster SK, Dwivedy A, Pillai EK, Sheridan GK, Svoboda H, Viana M,
 981 Costa LD, Guck J, Holt CE, Franze K (2016) Mechanosensing is critical for axon growth in the
 982 developing brain. *Nat Neurosci* 19: 1592-1598
 983 Laukaitis CM, Webb DJ, Donais K, Horwitz AF (2001) Differential dynamics of alpha 5
 984 integrin, paxillin, and alpha-actinin during formation and disassembly of adhesions in
 985 migrating cells. *J Cell Biol* 153: 1427-40
 986 Leach JB, Brown XQ, Jacot JG, Dimilla PA, Wong JY (2007) Neurite outgrowth and branching
 987 of PC12 cells on very soft substrates sharply decreases below a threshold of substrate
 988 rigidity. *J Neural Eng* 4: 26-34
 989 Lo CM, Wang HB, Dembo M, Wang YL (2000) Cell movement is guided by the rigidity of the
 990 substrate. *Biophys J* 79: 144-52
 991 Machacek M, Hodgson L, Welch C, Elliott H, Pertz O, Nalbant P, Abell A, Johnson GL, Hahn
 992 KM, Danuser G (2009) Coordination of Rho GTPase activities during cell protrusion. *Nature*
 993 461: 99-103
 994 McMahon HT, Boucrot E (2011) Molecular mechanism and physiological functions of
 995 clathrin-mediated endocytosis. *Nat Rev Mol Cell Biol* 12: 517-533
 996 Merrifield CJ, Kaksonen M (2014) Endocytic Accessory Factors and Regulation of Clathrin-
 997 Mediated Endocytosis. *Cold Spring Harbor Perspectives in Biology* 6
 998 Nikolopoulos SN, Turner CE (2000) Actopaxin, a new focal adhesion protein that binds
 999 paxillin LD motifs and actin and regulates cell adhesion. *The Journal of cell biology* 151:
 1000 1435-48
 1001 Nishimura T, Kaibuchi K (2007) Numb controls integrin endocytosis for directional cell
 1002 migration with aPKC and PAR-3. *Dev Cell* 13: 15-28
 1003 Ochoa GC, Slepnev VI, Neff L, Ringstad N, Takei K, Daniell L, Kim W, Cao H, McNiven M,
 1004 Baron R, De Camilli P (2000) A functional link between dynamin and the actin cytoskeleton
 1005 at podosomes. *J Cell Biol* 150: 377-89
 1006 Palamidessi A, Frittoli E, Garre M, Faretta M, Mione M, Testa I, Diaspro A, Lanzetti L, Scita G,
 1007 Di Fiore PP (2008) Endocytic trafficking of Rac is required for the spatial restriction of
 1008 signaling in cell migration. *Cell* 134: 135-47
 1009 Park YK, Goda Y (2016) Integrins in synapse regulation. *Nat Rev Neurosci* 17: 745-756
 1010 Paszek MJ, Zahir N, Johnson KR, Lakins JN, Rozenberg GI, Gefen A, Reinhart-King CA,
 1011 Margulies SS, Dembo M, Boettiger D, Hammer DA, Weaver VM (2005) Tensional
 1012 homeostasis and the malignant phenotype. *Cancer Cell* 8: 241-54
 1013 Raiborg C, Wenzel EM, Pedersen NM, Olsvik H, Schink KO, Schultz SW, Vietri M, Nisi V, Bucci
 1014 C, Brech A, Johansen T, Stenmark H (2015) Repeated ER-endosome contacts promote
 1015 endosome translocation and neurite outgrowth. *Nature* 520: 234-8

1016 Raucher D, Sheetz MP (2000) Cell spreading and lamellipodial extension rate is regulated
1017 by membrane tension. *The Journal of cell biology* 148: 127-36
1018 Ricotta D, Conner SD, Schmid SL, von Figura K, Honing S (2002) Phosphorylation of the AP2
1019 mu subunit by AAK1 mediates high affinity binding to membrane protein sorting signals. *J*
1020 *Cell Biol* 156: 791-5
1021 Ridley AJ (2011) Life at the leading edge. *Cell* 145: 1012-22
1022 Rossner M, Yamada KM (2004) What's in a picture? The temptation of image manipulation.
1023 *J Cell Biol* 166: 11-5
1024 Saengsawang W, Mitok K, Viesselmann C, Pietila L, Lumbard DC, Corey SJ, Dent EW (2012)
1025 The F-BAR protein CIP4 inhibits neurite formation by producing lamellipodial protrusions.
1026 *Curr Biol* 22: 494-501
1027 Saha K, Keung AJ, Irwin EF, Li Y, Little L, Schaffer DV, Healy KE (2008) Substrate Modulus
1028 Directs Neural Stem Cell Behavior. *Biophysical Journal* 95: 4426-4438
1029 Saito T, Nakatsuji N (2001) Efficient gene transfer into the embryonic mouse brain using in
1030 vivo electroporation. *Dev Biol* 240: 237-46
1031 Schaller MD (2001) Paxillin: a focal adhesion-associated adaptor protein. *Oncogene* 20:
1032 6459-72
1033 Smits WK, Kuipers OP, Veening JW (2006) Phenotypic variation in bacteria: the role of
1034 feedback regulation. *Nat Rev Microbiol* 4: 259-71
1035 Sundararaghavan HG, Monteiro GA, Firestein BL, Shreiber DI (2009) Neurite growth in 3D
1036 collagen gels with gradients of mechanical properties. *Biotechnol Bioeng* 102: 632-43
1037 Tachibana K, Sato T, D'Avirro N, Morimoto C (1995) Direct association of pp125FAK with
1038 paxillin, the focal adhesion-targeting mechanism of pp125FAK. *J Exp Med* 182: 1089-99
1039 Tse JR, Engler AJ (2010) Preparation of hydrogel substrates with tunable mechanical
1040 properties. *Curr Protoc Cell Biol* Chapter 10: Unit 10 16
1041 Turner CE (2000) Paxillin and focal adhesion signalling. *Nat Cell Biol* 2: E231-6
1042 Turner CE, Brown MC, Perrotta JA, Riedy MC, Nikolopoulos SN, McDonald AR, Bagrodia S,
1043 Thomas S, Leventhal PS (1999) Paxillin LD4 motif binds PAK and PIX through a novel 95-kD
1044 ankyrin repeat, ARF-GAP protein: A role in cytoskeletal remodeling. *J Cell Biol* 145: 851-63
1045 Turner CE, Glenney JR, Jr., Burridge K (1990) Paxillin: a new vinculin-binding protein
1046 present in focal adhesions. *The Journal of cell biology* 111: 1059-68
1047 White DP, Caswell PT, Norman JC (2007) alpha v beta3 and alpha5beta1 integrin recycling
1048 pathways dictate downstream Rho kinase signaling to regulate persistent cell migration. *J*
1049 *Cell Biol* 177: 515-25
1050 Wirtz D, Konstantopoulos K, Searson PC (2011) The physics of cancer: the role of physical
1051 interactions and mechanical forces in metastasis. *Nat Rev Cancer* 11: 512-22
1052 Wood CK, Turner CE, Jackson P, Critchley DR (1994) Characterisation of the paxillin-binding
1053 site and the C-terminal focal adhesion targeting sequence in vinculin. *J Cell Sci* 107 (Pt 2):
1054 709-17
1055 Xie W, Zhang K, Cui B (2012) Functional characterization and axonal transport of quantum
1056 dot labeled BDNF. *Integr Biol (Camb)* 4: 953-60
1057 Yap CC, Winckler B (2012) Harnessing the power of the endosome to regulate neural
1058 development. *Neuron* 74: 440-51
1059 Yeung T, Georges PC, Flanagan LA, Marg B, Ortiz M, Funaki M, Zahir N, Ming W, Weaver V,
1060 Janmey PA (2005) Effects of substrate stiffness on cell morphology, cytoskeletal structure,
1061 and adhesion. *Cell Motil Cytoskeleton* 60: 24-34

1062 Zheng J, Lamoureux P, Santiago V, Dennerll T, Buxbaum RE, Heidemann SR (1991) Tensile
1063 regulation of axonal elongation and initiation. J Neurosci 11: 1117-25

1064

1065

1066

1067

1068

1069

1070

1071 **Figure Legends**

1072

1073 **Figure 1, with 3 supplementary figures**

1074 **Morphology and endocytic activity of neurons grown on substrates of varying**
1075 **stiffness**

1076 **A.** Substrate modulus-dependent biphasic distribution of lamellipodium occupancy. **(A1)**
1077 Representative intensity profile of phalloidin-stained hippocampal neurons on a soft
1078 hydrogel ($E= 0.1$ kPa). Lamellipodium occupancy (LO) of each phalloidin-positive
1079 segment is calculated by the formula shown in the box at bottom right. **(A2)**
1080 Representative images of neurons grown on substrates for 5 hours or 16 hours and
1081 stained with phalloidin (Red), DAPI (Blue), and antibodies against Tuj-1 (Green), as
1082 indicated. Scale bar: 20 μm . **(A3)** Histograms of LO distributions at 5 hr showing two
1083 distinct patterns in 0.1, 1, or 20 kPa cultures ($n>68$ cells for each experiment). Simplified
1084 drawings above histograms illustrate the typical segmented lamellipodium ("SL") and
1085 broad lamellipodium ("BL") phenotypes in 5 hr neuronal cultures, as indicated. **(A4** and
1086 **A5)** Histograms summarizing the percentages of lamellipodium phenotypes seen in 5 hr
1087 cultures (A4) and the distributions of neurite numbers (A5) in 16 hr cultures. Data
1088 represent mean \pm SEM ($n>3$ independent experiments; 150 cells for each culture; "*", p
1089 < 0.05 ; "**", $p<0.01$; "****", $p < 0.0001$; one way ANOVA with *Dunnett's post hoc* test).

1090 **B.** Enhanced membrane endocytosis in 0.1 kPa cultures. Time-lapse images (20
1091 frames; 2-minute intervals) of neurons isolated from E17.5 rat cortices transfected in
1092 utero at E16 without **(B1)** or with **(B2)** IRES constructs harboring control EGFP and/or a
1093 dominant-negative dynamin II mutant (Dy^{II}^{K44A}), cultured on 0.1 kPa or 20 kPa gels for
1094 5 hr, followed by endocytosis assay in the presence or absence of the endocytosis
1095 inhibitors Dynole 2-24 or Dyngo 4a, as indicated. Dashed lines surround the region of
1096 interest (ROI) in quantitative FM4-64 measurements. Asterisks in **B2** mark non-
1097 transduced neighboring cells. Graph at right summarizes the accumulation curves of
1098 FM4-64 signal (\pm SEM, $n>3$ independent experiments, 10-20 cells per group, normalized
1099 to $t=0$ value; "****", $p<0.0001$; two-way RM ANOVA with *Dunnett's post hoc* test), which
1100 reflects the rate of FM4-64 uptake at different time-points after FM4-64 loading. The

1101 data were fitted to a single exponential to determine the time ($t_{1/2}$) required to reach half
1102 of the plateau value. **(B3)** Representative images of neurons plated on 0.1 kPa or 20
1103 kPa gels overnight, followed by incubation of quantum dot-conjugated brain-derived
1104 neurotrophic factor (QD-BDNF) for 5 hr. Dot plot showing that 0.1 kPa cultures exhibited
1105 a significantly higher level (n=39-46 cells from three independent experiments; “***”,
1106 $p<0.001$; “****”, $p<0.0001$; one way ANOVA with *Dunnett’s post hoc* test) of QD-BDNF
1107 internalization (as reflected by a ~2-fold greater quantity of intracellular QD-BDNF) than
1108 20 kPa cultures.

1109 **C.** Expression of DynII^{K44A} prevents neurite formation and cortical neuron migration *in vivo*.
1110 **(C1)** Fluorescence images of P0 rat cortices transfected in utero at E16 with IRES
1111 constructs harboring control EGFP and/or DynII^{K44A}. The middle panels show 16x
1112 magnifications of boxed regions of the corresponding P0 cortex in the top panels. The
1113 bottom panels show sample tracings of 2D projections from confocal images of typical
1114 cortical neurons in the corresponding P0 cortex. Bar, 100 μ m. **(C2 and C3)** Histograms
1115 showing the localization (C2) and the percentage (C3) of transfected cortical neurons
1116 exhibiting unipolar/bipolar polarized processes (“polarized”), multiple short neurites
1117 without a long tailing process (“unpolarized”), or no process (“no neurite”; arrowheads in
1118 the middle panels) in the cortical plate (“CP”) or subventricular zone/intermediate zone
1119 (“SVZ / IZ”) regions. Datasets (mean \pm SEM, n>150 cells per cortex, >5 cortices each;
1120 “****”, $p<0.001$, multiple *t* test) showing significant differences are marked.

1121

1122 Figure 1– figure supplement 1. Hippocampal neurons cultured on polyacrylamide hydrogels
1123 of varying stiffness

1124 **A.** Schematic of the three-layer assembly of polyacrylamide (PA) hydrogels (diameter=1.8
1125 mm, thickness=200 μ m). Light blue, the poly-L-Lysine/laminin-coated side of the coverslip.

1126 **B.** Atomic force microscopy measurement of elastic modulus (\pm SEM, n=3) of PA gels.
1127 Table shows the ratio of acrylamide and bis-acrylamide used to determine the crosslink
1128 density and the stiffness (0.1 kPa, 1 kPa, and 20 kPa) of the polymers.

1129 **C, D.** Transfer printing of laminin on hydrogels. (C) Representative images of PA hydrogel
1130 peeled from laminin-coated coverslips, both immunostained with antibodies against laminin
1131 (shown in green). Note that laminin was completely transferred from the laminin-coated

1132 coverslip to the gel surface. (D) Quantification of laminin fluorescence intensity (\pm SEM,
1133 $n>3$; “ns”, no significance; *t-test*) on the gel surface before and after incubation for 16 hr
1134 with culture medium. Acid-washed coverslips were pre-coated with laminin (a stock
1135 concentration of 1.62 mg/ml) in a 1:50 dilution. Note that the staining intensity of surface
1136 laminin was comparable between 0.1 kPa and 20 kPa gels.

1137 **E.** Cell type enrichment analysis for hippocampal cultures. Cultured neurons plated on
1138 substrates were immunostained with antibodies against the neuron-specific marker Tuj-1
1139 and the astroglial marker glial fibrillary acidic protein (GFAP). Histogram showing
1140 percentages (\pm SEM; $n>200$ cells for each group from more than three independent
1141 experiments; “*”, $p < 0.05$; relative to that of 0.1 kPa culture, *t-test*) of Tuj-1- or GFAP-
1142 positive cells in hippocampal cultures at 3 days in vitro (DIV).

1143 **F.** Cell viability analysis for hippocampal neurons cultured on PA gels and glass. DIV3
1144 cultures were subjected to propidium iodide (PI) staining. Arrow, apoptotic cells with
1145 fragmented nuclei (PI positive). Dimethyl sulfoxide (2%) was used as a positive control of
1146 maximum cytotoxicity. Data represent mean \pm SEM ($n>200$ cells for each group from more
1147 than three independent experiments; “*”, $p < 0.05$; “****”, $p<0.001$; relative to that of glass
1148 culture, *t-test*).

1149

1150 Figure 1– figure supplement 2. Differential lamellipodium phenotypes of neurons grown
1151 on hydrogels

1152 **A, B.** Phalloidin intensity profiling of neurons on soft ($E=0.1$ kPa; **A**) and stiff ($E=20$ kPa;
1153 **B**) hydrogels stained with phalloidin (Red) for F-actin filaments and antibodies against
1154 Tuj-1 (Green), as indicated. Lamellipodium occupancy (LO) of phalloidin-positive
1155 segments (“S”) along the cell periphery was calculated according to the formula shown
1156 in the lower panel. Cells exhibiting typical morphologies of the segmented lamellipodium
1157 (“SL”, A) or broad lamellipodium (“BL”, B) are shown.

1158 **C, D.** Time-lapse bright-field images of newly plated neurons on 0.1 kPa (C) or 20 kPa (D)
1159 gels. Note that neurite initiation sites (arrowheads at time-point=15:10:00) are correlated
1160 with the positions of initial segmented lamellipodia (delimited by the dashed line in panel C;

1161 individual LO < 0.33). Broad lamellipodia of a neuron grown on a 20 kPa gel are delimited
1162 by solid lines in panel D. Scale bar = 20 μ m.

1163 **E, F.** Distribution of individual lamellipodium occupancy (E) and total lamellipodium
1164 occupancy (F) from the same sets of experiments shown in main Figure 1A3. Simplified
1165 drawings above histograms illustrate the typical segmented lamellipodium and broad
1166 lamellipodium phenotypes of hippocampal neurons grown on soft ($E = 0.1$ kPa or 1 kPa)
1167 and stiff ($E = 20$ kPa) PA hydrogels.

1168

1169 Figure 1– figure supplement 3. Differential gene expression pattern of neurons grown
1170 on hydrogels

1171 **A.** Up-regulation of clathrin-associated endocytosis genes in 0.1 kPa cultures. Gene
1172 expression patterns emerging from microarray analysis were grouped into four modules:
1173 expression increased with substrate softness in 5 hr (i) or 16 hr (iii) cultures, or
1174 increased with substrate stiffness in 5 hr (ii) or 16 hr (iv) cultures (cut off: >1.5-fold
1175 change, $p < 0.05$, $n = 3$ independent experiments). Normalized expression levels are
1176 represented by a color-coded heatmap.

1177 **B.** A QuantiGene Plex branched-chain DNA amplification assay validated the relatively
1178 increased levels of mRNAs encoding the clathrin-associated endocytosis factors Dab2,
1179 Myo6, and Cltc in neurons grown on 0.1 kPa gels. Data represent fold changes in RNA
1180 levels (\pm SEM; $n = 4-5$ independent experiments; relative to that of 0.1 kPa culture; “*”,
1181 $p < 0.05$; t test).

1182 **C.** Representative single-molecule RNA fluorescence in situ hybridization (smRNA
1183 FISH) images of mRNA encoding Myo6, Dab2, Chd11, Vcl, or Cry61 on segmented
1184 lamellipodium (SL) or broad lamellipodium (BL) neurons in 5 hr cultures, as indicated.
1185 Histograms showing average number (\pm SEM; $n = 42-52$ cells; “*”, $p < 0.05$; “***”, $p < 0.01$;
1186 “*****”, $p < 0.0001$; t test) of smRNA FISH puncta for each gene per single neurons of the
1187 SL and BL cells.

1188

1189

1190 **Figure 2, with 1 supplementary figure**

1191 **Substrate modulus-dependent Rac1 increase and lamellipodium segmentation**
1192 **require endocytic activity**

1193 **A.** Inhibition of endocytosis suppresses Rac1 activity in 0.1 kPa cultures. (A1-A3)
1194 Representative images of 5 hr neuronal cultures treated with the endocytosis inhibitors
1195 dynasore (50 μ M, 1 hr), Dynole 2-24 (2-24, 2 μ M, 1 hr), Dyngo 4a (4a, 2 μ M, 1 hr) or
1196 monodansylcadaverine (MDC, 100 μ M, 1hr) and immunostained with antibodies against
1197 Rac1, GTP-bound Rac1 (“active Rac1”; A1, left panel), or RhoA (A1, right panel). The
1198 same staining procedure was applied to the IUE neuron (A2, arrow) expressing control
1199 EGFP and/or DynII^{K44A} as shown in **A2**. Asterisks mark non-transduced neighboring
1200 cells. Intensities of active Rac1 and RhoA correspond to linear pseudocolor maps. (A3)
1201 Histograms, all from experiments similar to those described above, showing that
1202 endocytosis inhibition significantly decreases levels of total Rac1 and active Rac1 (but
1203 not RhoA) at lamellipodial protrusions (at 5 hr) in 0.1 kPa cultures. Data represent mean
1204 intensity \pm SEM (n>50 per group from three independent experiments; “****”, $p<0.001$;
1205 one way ANOVA with *Dunnett’s post hoc* test).

1206 **B.** Representative FRET-based imaging of hippocampal neurons transfected with a
1207 FRET indicator for GTP-bound Rac1 (Rac1-2G; see Materials and Methods). (B1)
1208 Images of monomeric Teal fluorescent protein 1 (mTFP1) and FRET signals (presented
1209 as pseudocolor maps in a linear scale) acquired from neurons plated on 0.1 kPa gels in
1210 the presence or absence of dynasore (50 μ M) or MDC (100 μ M) for 1 hr. Bar, 20 μ m. (B2)
1211 Traces depict active Rac1 levels at protrusions, measured across the dashed line as
1212 shown in **B1**, and indicated by FRET signal calculated as the ratio of Venus to mTFP1
1213 fluorescence [F(Venus)/F(mTFP1)]. (B3) Quantitative measurement of FRET signals
1214 (\pm SEM, n=5 cells for each group; “*”, $p<0.05$, compared to time=0 value; multiple *t* tests)
1215 before and after bath application of 50 μ M dynasore or 100 μ M MDC. Arrow marks drug
1216 addition (time=0).

1217 **C.** Inhibition of endocytosis decreases the probability of lamellipodium segmentation
1218 and delays neurite initiation on soft gels. (C1) Representative fluorescent images of
1219 neurons plated on 0.1 kPa gels for 5 hr in the absence or presence of indicated

1220 endocytosis inhibitors. Scale bar: 20 μm . (C2) Representative fluorescent images of
1221 transfected IUE neurons (arrow) expressing control EGFP and/or a dominant-negative
1222 dynamin II mutant (Dy II^{K44A}), cultured on 0.1 kPa gels for 16 hr, and stained with
1223 phalloidin (Red), DAPI (Blue), and antibodies against Tuj-1 (Green). Asterisks mark non-
1224 transduced neighboring cells. Scale bar: 20 μm . Histograms summarize the
1225 percentages ($\pm\text{SEM}$; “****”, $p < 0.001$, one way ANOVA with *Dunnett’s post hoc* test) of
1226 16 hr neurons bearing neurites in the presence or absence of dynasore (50 μM , 5-hr
1227 treatment) or MDC (100 μM , 5-hr treatment), as indicated.

1228

1229 Figure 2– figure supplement 1. Increased Rac1 activity in neurons grown on 0.1 kPa gels

1230 **A.** Active Rac1 and active RhoA pull-down assay of neurons grown on 0.1 kPa or 20
1231 kPa hydrogels. Cell lysates obtained from cortical neurons grown on substrates (5 hr of
1232 culture) were subjected to a GST resin pull-down assay using PAK-GST (upper panel)
1233 or GST-Rhotekin-RBD (lower panel), as indicated. The precipitants were analyzed by
1234 Western blotting with antibodies specific against Rac1 or RhoA. Histograms reflect
1235 quantitative measurement of band intensities ($\pm\text{SEM}$, $n=3$; normalized to the
1236 corresponding protein input and relative to that of 0.1 kPa culture; “*”, $p<0.05$; “**”,
1237 $p<0.001$, *t* test) of the active GTP-bound forms of Rac1 or RhoA.

1238 **B.** Pharmacological inhibition of Rac1 activation significantly increases the
1239 lamellipodium occupancy in 5 hr neuronal cultures on 0.1 kPa gels. Right panel shows
1240 representative images of neuronal cultures on 0.1 kPa gels, in the absence and
1241 presence of the selective Rac1-GEF inhibitor NSC-23766 (1 μM ; 1 hr treatment), the
1242 PI3K inhibitor LY-294002 (10 μM ; 1 hr treatment), or the ROCK inhibitor Y-27632 (25
1243 μM ; 1 hr treatment), stained with phalloidin (red) at the 5 hr or 48 hr time-points after cell
1244 plating, as indicated. Dashed line delimits lamellipodium area. Bar, 20 μm . Histograms
1245 summarize average lamellipodium occupancy in 5 hr neurons and percentages of
1246 neurite-bearing neurons in 16 hr cultures ($\pm\text{SEM}$; $n=300$ total cells for each group from
1247 three independent experiments; “****”, $p<0.0001$, unpaired *t* test) from all experiments
1248 similar to that shown in the right panel.

1249

1250

1251 **Figure 3, with 2 supplementary figures and 1 video**

1252 **Substrate modulus-dependent expression of paxillin and its association with**
1253 **endocytic and adhesion machineries**

1254 **A.** Representative Western blots of endocytic or adhesion molecules. Cell lysates
1255 obtained from cortical neurons grown on substrates with differing stiffness were
1256 subjected to immunoblotting with antibodies to indicated proteins.

1257 **B.** Summary histograms, all from experiments similar to that described in **A**, showing
1258 greater (>2-fold) abundance of paxillin, phospho-paxillin^{Y118} (p-paxillin), myosin VI
1259 (myo6), CIP4 and clathrin heavy chain (CHC) proteins in neurons grown on soft
1260 substrates (0.1 and 1 kPa) compared to those grown on stiff substrates (20 kPa and
1261 glass). Note the inverse expression of endocytic factors and adhesion molecules (i.e.,
1262 talin1/2, integrin β 1, vinculin and p-FAK^{Y397}). Data represent mean \pm SEM (n \geq 3,
1263 normalized to control actin; compared to 0.1 kPa cultures; “*”, $p < 0.05$; “**”, $p < 0.01$;
1264 “***”, $p < 0.001$; t -test).

1265 **C-F.** Paxillin co-localizes with the endocytosis complex at neuronal growth cones on soft
1266 substrates. **(C)** Representative confocal images of 16 hr neurons on 0.1 kPa gels co-
1267 immunostained with antibodies against paxillin (Green in merge panel), adaptor-
1268 associated kinase1 (AAK1, Red in merge panel), p-FAK^{Y397} (Red in merge panel), or F-
1269 actin, as indicated. Right panels show the region of interest ROI (marked by numbers)
1270 of neurite tips represented at higher magnification. Bar: 20 μ m. **(D and E)** Similar to **C**,
1271 except the resolution of images has been enhanced (\sim 1.7X higher) using Airyscan.
1272 Note that surface rendering was applied at neurite tips to more clearly show co-
1273 localization (yellow) of paxillin with indicated factors. Bar: 20 μ m. **(F)** Histograms, all
1274 from experiments similar to those described in **d** and **e**, summarizing percentages of
1275 paxillin co-localized with indicated endocytic or adhesion factors on hydrogels. Data
1276 represent percentages (\pm SEM, n=15 neurons for each set of experiments; ROI, 5 X 5
1277 μ m within one lamellipodium; “*”, $p < 0.01$; “***”, $p < 0.001$; “****”, $p < 0.0001$; t test).

1278

1279 Figure 3– figure supplement 1. Paxillin associates with free-floating vesicles in rat
1280 embryonic brain lysate

1281 **A-C.** Membrane flotation assay of embryonic brain **(A)** and heart **(B)** tissue lysates.
1282 Representative Western blot of gradient fractionations probed with antibodies against
1283 endocytic factors (Rab5 and CHC), adhesion-associated molecules (vinculin, and
1284 phospho-FAK^{Y397}), paxillin, and actin, as indicated. Histogram in **A** reflects quantitative
1285 measurements of the protein levels (\pm SEM; n=3 independent experiments; “***”, p<0.01;
1286 compared to that of paxillin; multiple *t* test for each fraction) found in the floating fraction
1287 (collective measurement from fraction 10 to fraction 18) out of the total gradient fractions.
1288 **(C)** Traces depict the differential protein levels (\pm SEM; from all experiments similar to that
1289 described in A and B, “****”, p<0.001; multiple *t* test) in each gradient fraction between
1290 embryonic brain and heart lysates, as indicated.

1291

1292 Figure 3– figure supplement 2. Ectopically-expressed paxillin displays predominantly
1293 retrograde motility

1294 Representative image **(A)** and kymograph **(B)** of paxillin-mCherry trajectories (*x*-axis,
1295 distance; *y*-axis, time) generated from 180-second time-lapse images (90 frames; 0.5
1296 frames per second), showing bidirectional movement of paxillin-mCherry along the axon
1297 (dashed line). Summary of directionality **(C)** and velocity distribution **(D)** of paxillin-mCherry
1298 along axons from all experiments similar to that described in B. Data represent means \pm
1299 SEM (n=15 cells).

1300

1301 Figure 3– video 1. Fast transport of paxillin-mCherry.

1302 A 180-second video (0.5 frames per second) shows bidirectional, long-range movements of
1303 paxillin-mCherry in a DIV5 neuron grown on 0.1 kPa gel.

1304

1305 **Figure 4, with 1 supplementary figure**

1306 **The endocytic F-BAR protein CIP4 directly associates with paxillin and competes**
1307 **with vinculin for paxillin binding**

1308 **A.** Paxillin preferentially binds endocytic factors in neurons grown on soft substrates.
1309 Paxillin-associated complexes were immunoprecipitated (IP) in lysates made from
1310 E17.5 rat brain or from cortical neuronal cultures grown on different substrates using a
1311 specific paxillin antibody and were then detected by Western blot analysis. Normal
1312 rabbit IgG (“IgG”) served as a negative control. Histograms show the opposing binding
1313 preference of paxillin towards CIP4/CHC or vinculin when grown on soft (0.1 kPa or 1
1314 kPa) versus rigid (20 kPa or glass) substrates. Data represent mean intensity \pm SEM
1315 (n=3 independent experiments; “*”, $p < 0.05$; *t*-test).

1316 **B.** Western blot showing direct interaction of paxillin with CIP4. Bacterially-expressed
1317 His-CIP4 was purified by fast protein liquid chromatography and subjected to a GST
1318 pull-down assay using GST-PXN^{FL}, GST-PXN ^{Δ LIM3-4} or GST alone. Precipitants were
1319 analyzed by Western blotting with antibodies specific to CIP4. Histograms summarize
1320 protein levels as determined by immunoblotting of full-length (His-CIP4) or F-BAR
1321 domain-deleted (His- Δ F-BAR) CIP4 pulled-down by GST-paxillin variants (\pm SEM, n=3;
1322 normalized to the corresponding GST-PXN^{FL} or GST-PXN ^{Δ LIM3-4} inputs; “***”, $p < 0.01$, *t*
1323 test).

1324 **C & D.** Mapping of paxillin domains interacting with CIP4 or vinculin. (**C**) GST pull-down
1325 and immunoblotting of vinculin, myc-CIP4, and CHC in lysates of myc-CIP4-expressing
1326 HEK293T cells. Histograms reflect quantification of levels of proteins pulled-down by
1327 GST fusions of full-length (“FL”) or LIM domain- and/or LD motif-deleted forms of
1328 paxillin, all from experiments similar to those shown in top panels (\pm SEM, n \geq 3
1329 independent experiments; “*”, $p < 0.05$; “***”, $p < 0.01$; “****”, $p < 0.001$; *t* test). (**D**) Schematic
1330 of GST fusion proteins used in **c**. Table summarizing relative CIP4 or vinculin (“Vin”)
1331 binding by paxillin deletion mutants or full-length protein. Solid lines mark primary sites
1332 of interaction, and dashed lines mark accessory interaction motifs for strong binding to
1333 vinculin or CIP4. Binding strength relative to full-length paxillin indicated as: “++++” > 75%
1334 > “+++” > 50% > “++” > 25% > “+” > 5% > “+/-”.

1335 **E.** *In vitro* protein interaction and competitive binding assays in HEK293T cells
1336 transfected with various amounts (1, 6, and 12 μ g) of plasmids encoding myc-tagged
1337 CIP4 protein (myc-CIP4) and/or control vectors, as indicated. Cell lysates were
1338 subjected to a GST pull-down assay with GST-PXN^{FL} or GST alone, and immunoblotted

1339 with vinculin and myc antibodies. Line chart depicts averaged protein levels as
1340 determined by immunoblotting of CIP4 or vinculin pulled-down by GST-PXN^{FL} (\pm SEM,
1341 n=4; normalized to band intensity of corresponding GST-paxillin variant).

1342 **F.** *In vivo* protein interaction and competitive binding assays in HEK293T cells
1343 transfected with various amounts (7.5 μ g and 15 μ g) of plasmids encoding the F-BAR
1344 domain (“F-BAR”) alone or F-BAR-domain-deleted (“ Δ N’-F-BAR”) CIP4 and/or control
1345 vectors, as indicated. Cell lysates were immunoprecipitated by paxillin antibodies and
1346 blotted with myc or vinculin antibodies. Histograms show relative protein levels as
1347 determined by immunoblotting of vinculin co-immunoprecipitated by paxillin antibodies
1348 (\pm SEM, n=3; “*”, $p < 0.05$, t test).

1349
1350 Figure 4– figure supplement 1. Paxillin associates with the F-BAR domain of CIP4

1351 **A.** Structures of the vinculin tail (PDB ID: 1QKR; top panel) and the CIP4 F-BAR domain
1352 (PDB ID: 2EFK; bottom panel) constructed by JMOl, version 14.4.4. Yellow marks
1353 indicate the predicted paxillin-binding subdomain (PBS) for vinculin (951K to 970Q) or
1354 CIP4 (35R to 55P). Secondary structures were predicted by the DSSP or STRIDE
1355 databases.

1356 **B.** Mapping of paxillin domains interacting with CIP4 or vinculin. GST pull-down and
1357 immunoblotting of vinculin and myc-CIP4 in lysates of myc-CIP4-expressing HEK293T
1358 cells. Histograms reflect quantification of levels of proteins pulled-down by GST fusions
1359 of full-length (“FL”) or LD motif-deleted forms of paxillin, all from experiments similar to
1360 those shown in top panels (\pm SEM, $n \geq 3$ independent experiments; “***”, $p < 0.01$; “****”,
1361 $p < 0.001$; multiple t test). Schematic of GST fusion proteins and table summarizing
1362 relative CIP4 or vinculin (“Vin”) binding by paxillin deletion mutants or full-length protein
1363 shown in the top panel. Binding strength relative to full-length paxillin indicated as: “++++”
1364 $> 75\% > “+++” > 50\% > “++” > 25\% > “+” > 5\% > “+/-”$. Note that although CIP4 primarily
1365 associates with LIM domains, deletion of the paxillin LD1-3 domain reduced its affinity
1366 for CIP4.

1367 **C.** Mapping of CIP4 domains interacting with paxillin. GST fusion proteins of full-length
1368 CIP4 (“FL”) or its variants with F-BAR domain, HR1 and/or SH3 domain truncations were
1369 subjected to GST pull-down assays in HEK293T cell lysates, followed by immunoblotting

1370 for paxillin and actin. Histogram reflects quantitative measurement of relative protein levels
1371 (\pm SEM, $n \geq 3$ independent experiments; compared to that of FL experiment; “***”, $P < 0.01$; t -
1372 test) pulled down by GST-CIP4, as indicated.

1373 **D.** Schematic of GST fusion proteins used in **B**. Table summarizes relative paxillin
1374 binding by CIP4 deletion mutants or full-length protein. Binding strength relative to that of
1375 full-length CIP4 is represented as: “++++” > 75% > “+++” > 50% > “++” > 25% > “+”.

1376 **E.** *In vivo* protein interactions in HEK293T cells co-transfected with plasmids encoding
1377 paxillin-GFP and myc-tagged CIP4 deletion mutants or full-length protein, as indicated.
1378 Cell lysates were immunoprecipitated by myc antibody and blotted with paxillin or myc
1379 antibodies. Histograms show relative protein levels as determined by immunoblotting for
1380 paxillin co-immunoprecipitated by myc antibody. Data represents mean (\pm SEM from more
1381 than three independent experiments; compared to that of F-BAR experiment; “**”, $P < 0.05$; t -
1382 test).

1383 **F.** *In vitro* protein interaction and competitive binding assays in HEK293T cells
1384 transfected with various amounts (1, 6, and 12 μ g) of plasmids encoding myc-tagged
1385 CIP4 protein (myc-CIP4) and/or control vectors, as indicated. Cell lysates were
1386 subjected to a GST pull-down assay with GST-PXN^{FL}, GST-PXN ^{Δ LD1}, GST-PXN ^{Δ LIM3-4} or
1387 GST alone, and immunoblotted with vinculin and myc antibodies. Line chart depicts
1388 averaged protein levels as determined by immunoblotting of CIP4 or vinculin pulled-
1389 down by GST-PXN variant (\pm SEM, $n = 3-4$; normalized to band intensity of corresponding
1390 GST-paxillin variant).

1391

1392 **Figure 5, with 2 supplementary figures**

1393 **Paxillin is required for endocytosis promoted by a soft surface**

1394 **A.** Paxillin knockdown suppresses the endocytic activity of neurons grown on 0.1 kPa
1395 gels. Representative time-lapse images of FM4-64 uptake in 3-DIV neurons on
1396 substrates of varying elasticity. Hippocampal neurons on 0.1 kPa gels were transduced
1397 with lentiviral particles harboring an shRNA-resistant construct (“PXN-R”) and/or
1398 constructs harboring scrambled control or paxillin (“PXN shRNA C + D”) shRNA at 5 hr

1399 after cell plating. Dashed circles surround the region of interest (ROI) in quantitative
1400 FM4-64 measurements. Bar: 20 μ m.

1401 **B.** Similar to **A**, except constructs encoding GFP fusions of wild-type paxillin (“PXN^{WT}-
1402 GFP”; B1 and B2) or the corresponding LIM domain deletion mutant (“PXN^{LD1-3}-GFP”;
1403 B3) were used for lentiviral transduction. Asterisk: non-transduced neighboring cells.
1404 Arrows: neurons expressing GFP-tagged paxillin proteins. Bar: 20 μ m.

1405 **C-E.** Quantitative measurements of cumulative FM4-64 intensity (\pm SEM, $n > 3$
1406 independent experiments, 7-12 cells for each set of experiments; “*”, $p < 0.05$; “**”,
1407 $p < 0.001$; “***”, $p < 0.0001$; compared to control groups; multiple t tests), all from
1408 experiments similar to those described in **A** and **B**. Note that ectopic expression of wild-
1409 type paxillin, but not PXN^{LD1-3}, restored rapid endocytic FM4-64 uptake on 20 kPa stiff
1410 gels.

1411

1412 Figure 5– figure supplement 1. Knockdown efficiency of PXN shRNAs

1413 **A.** Western blot showing efficiency of shRNA-mediated paxillin knockdown. Mouse
1414 neuroblastoma Neuro-2a (N2a) cells were transfected with plasmids encoding
1415 scrambled shRNA (“scr”) or one of four paxillin shRNAs (sequence A, B, C, or D)
1416 targeting to different regions of the paxillin sequence. Summary histograms showing
1417 that shRNA D exerted a ~2-fold suppression on paxillin expression and it had no effect
1418 on vinculin expression. Data represent mean \pm SEM ($n = 5$, normalized to control actin,
1419 compared to that of scr experiment; “*”, $P < 0.05$; t -test “***”, $p < 0.01$, “****”, $p < 0.0001$; t
1420 test).

1421 **B.** Images of neurons transfected with plasmids encoding scrambled shRNA or paxillin
1422 shRNAs (shRNA C + shRNA D), immunostained with antibody specific against paxillin.
1423 Right-most panels show the region of interest (ROI, dashed box) of neurite tips at a
1424 higher magnification, with the intensity of paxillin staining coded by pseudocolors in a
1425 linear scale. Bar: 5 μ m. Dot plot reflects quantification of paxillin immunostaining
1426 intensity (\pm SEM, $n = 20$ cells each, normalized to EGFP intensity and relative to scramble
1427 control; “****”, $p < 0.0001$; one way ANOVA with *Dunnett’s post hoc* test).

1428

1429 Figure 5– figure supplement 2. Endocytic function and distribution patterns of CIP4
1430 protein in 0.1 kPa neuronal cultures

1431 **A.** CIP4 knockdown suppresses endocytic activity of neurons grown on 0.1 kPa gels.
1432 (A1) Western blot showing efficiency of shRNA-mediated CIP4 knockdown. HEK293T
1433 cells were transfected with plasmids encoding scrambled shRNA (“scr”) or one of four
1434 CIP4 shRNAs (sequence A, B, C, or D) targeting to different regions of the CIP4
1435 sequence. (A2) Representative time-lapse images of FM4-64 uptake in 5 hr neurons
1436 grown on 0.1 kPa gels. Time-lapse images (20 frames; 2-minute intervals) of neurons
1437 isolated from E17.5 rat cortices which were transfected in utero at E16 with constructs
1438 encoding scrambled control or CIP4 (“CIP4 shRNA A-D”) shRNA, and/or CIP4-GFP,
1439 cultured on 0.1 kPa for 5 hr, followed by endocytosis assay. Dashed circles surround the
1440 region of interest (ROI) for quantitative FM4-64 measurements. Asterisk marks non-
1441 transduced neighboring cells. Graph at right summarizes the accumulation curves of
1442 FM4-64 signal (\pm SEM, $n > 3$ independent experiments, 5-10 cells per group, normalized
1443 to $t=0$ value; compared to that of scrambled control experiment “*”, $p < 0.05$; multiple t
1444 tests for each time point).

1445 **B.** Images of neurons transfected with plasmids encoding CIP4-GFP, stained with
1446 phalloidin and DAPI. Right-most panels show the region of interest (ROI, dashed box) of
1447 neurite tips at a higher magnification. Note that CIP4-GFP was distributed along the
1448 enlarged lamella edge when neurons were cultured on 20 kPa gels.

1449 **C.** Fluorescence images (**C1**) of P0 rat cortices transfected in utero at E16 with IRES
1450 constructs harboring GFP control or CIP4-GFP. The bottom panels show 4x
1451 magnifications of boxed regions corresponding to the P0 cortex in the top panels. Bar,
1452 100 μ m. (**C2**) Histograms showing the percentages (\pm SEM, $n > 3$ cortices each; “n.s.”,
1453 not significant, multiple t test) of neurons residing in the cortical plate (“CP”),
1454 intermediate zone (“IZ”), or subventricular zone (“SVZ”) regions. (**C3**) Histograms
1455 showing the percentage (\pm SEM, $n > 150$ cells per cortex, > 3 cortices each; “n.s.”, not
1456 significant, multiple t test) of transfected cortical neurons exhibiting unipolar/bipolar
1457 polarized processes (“polarized”), multiple short neurites without a long tailing process
1458 (“unpolarized”), or no process (“no neurite”) in cortices.

1459

1460

1461 **Figure 6. Paxillin facilitates QD-BDNF uptake**

1462 **A.** QD-BDNF internalization assay on HEK293T cells co-transfected with expression
1463 vectors encoding the BDNF receptor TrkB (Red), together with shRNA constructs
1464 (Green) and/or wild-type paxillin, as indicated. Histograms showing that co-transfection
1465 of paxillin shRNA C and shRNA D significantly reduced QD-BDNF internalization (as
1466 reflected by an ~8-fold reduction in the quantity of intracellular QD-BDNF). Data
1467 represent means \pm SEM ($n \geq 3$ independent experiments, 26-52 cells for each set of
1468 experiments; compared to scrambled shRNA control; “****”, $p < 0.001$; ANOVA with
1469 *Dunnett’s post hoc* test).

1470 **B.** Similar to **A**, except cells were pre-incubated with or without the dynamin inhibitor
1471 dynasore (50 μ M, 30 min). Histograms show that dynamin is required for paxillin to
1472 promote QD-BDNF internalization. Data represent means \pm SEM ($n \geq 3$ independent
1473 experiments, 21-58 cells for each set of experiments; compared to GFP control; “****”,
1474 $p < 0.001$; ANOVA with *Dunnett’s post hoc* test).

1475

1476 **Figure 7, with 2 supplementary figures**

1477 **Paxillin knockdown alters neurite formation and neuronal migration *in vitro* and *in***
1478 ***vivo***

1479 **A & B.** Paxillin knockdown impairs lamellipodium segmentation and neurite formation in
1480 neuronal cultures on 0.1 kPa gels. **(A)** Images of 16 hr hippocampal neurons
1481 transfected with scrambled control or paxillin siRNA at 30 min after cell plating on 0.1
1482 kPa gels, followed by phalloidin staining for F-actin (Red) and immunostaining for the
1483 neuronal marker Tuj-1 (Green) at 16 hr after cell plating. **(B)** Histograms showing that
1484 paxillin knockdown significantly decreased the percentage of neurite-bearing neurons
1485 (left y-axis) and increased the percentage of neurons exhibiting the BL phenotype (right
1486 y-axis) in 0.1 kPa cultures. Data represent mean (\pm SEM; $n > 3$ independent experiments,
1487 > 250 cells for each group; “*”, $p < 0.05$; “***”, $p < 0.01$; *t* test).

1488 **C.** Similar to **A**, except that 16 hr neuronal cultures were immunostained with antibodies
1489 against active Rac1-GTP (Gray). Fluorescence intensity of active Rac1 (boxed region)
1490 is coded by pseudocolors in the linear scale (right panel in **C**). Scale bar: 20 μm .

1491 **D.** Quantification of active Rac1 levels at segmented lamellipodia (averaged pixel value
1492 of a 2 μm X 2 μm area) in 0.1 kPa cultures transfected with paxillin-siRNA or control
1493 scrambled siRNA. Data represent mean \pm SEM (n>3 independent experiments, >250
1494 cells for each group; “****”, $p < 0.001$; ANOVA with *Dunnett’s post hoc* test).

1495 **E.** Paxillin knockdown promotes aberrant neurite formation and cortical neuron migration *in*
1496 *vivo*. Fluorescence images of E20 rat cortices transfected in utero at E17.5 with IRES
1497 constructs harboring EGFP plus scrambled-shRNA control, paxillin shRNA C+D, and/or
1498 shRNA C+D-resistant PXN-R. The middle panels show 4x magnifications of boxed
1499 regions of the corresponding E20 cortex in the top panels. Bottom panels show sample
1500 tracings of 2D projections from confocal images of eight typical cortical neurons in the
1501 subventricular zone (“SVZ”) of the corresponding E20 cortex. Bar, 100 μm .

1502 **F.** Histograms showing the percentage (\pm SEM, n=3 cortices each; “*”, $p < 0.05$, two-
1503 tailed *t* test) of neurons residing in the cortical plate (“CP”), intermediate zone (“IZ”), or
1504 subventricular zone (“SVZ”) regions.

1505 **G.** Calculation of the percentages (\pm SEM, n>150 cells per cortex, >5 cortices each;
1506 “****”, $p < 0.001$, multiple *t* test) of transfected cortical neurons exhibiting unipolar/bipolar
1507 processes or no process (“none”; arrowheads in **e**) in the cortical SVZ/IZ region for
1508 cortices described in **e**. Datasets (connected by dashed lines) showing significant
1509 differences are marked.

1510 **H.** Schematic illustrating the proposed substrate elasticity-controlled, paxillin-dependent
1511 bistable mechanism, comprising a genetic response and mutual inhibition of
1512 endocytosis by adhesion and vice versa. Growth on a soft substrate shifts neurons to a
1513 Rac1-activated neuritogenic state.

1514

1515

1516 Figure 7– figure supplement 1. Manipulation of paxillin binding affinity leads to a SL-BL
1517 phenotypic switch

1518 **A.** Representative fluorescent images of transfected IUE neurons (yellow arrows)
1519 expressing control EGFP and/or a paxillin deletion mutation (Green), cultured on 0.1
1520 kPa (A1) or 20 kPa (A2) gels for 16 hr, and stained with phalloidin (Red), DAPI (Blue),
1521 and antibodies against Tuj-1 (Gray).

1522 **B.** Histograms summarize the percentages (\pm SEM; “*”, $p < 0.05$; “***”, $p < 0.001$, one way
1523 ANOVA with Dunnett’s post hoc test) of 16 hr neurons bearing segmented lamellipodia
1524 (“SL”) or broad lamellipodia (“BL”) in neurons expressing different paxillin deletion
1525 mutations, as indicated. The top panel shows schematic of the neurite phenotype switch
1526 observed in the PNX Δ LIM3-4 expressing neuron on 0.1 kPa gel and the PNX Δ LD1
1527 expressing neuron on 20 kPa gel.

1528

1529 Figure 7– figure supplement 2. Differential protein abundances between the endocytosis
1530 and adhesion machineries in embryonic brain, cardiac, and hepatic tissues

1531 Representative Western blots (**A**) and quantitative analysis (**B**) of embryonic E18 brain,
1532 heart and liver lysates. Note that endocytic factors (CHC, Rab5 and CIP4) are more
1533 abundant in brain than in heart. Data represent mean \pm SEM in more than three
1534 independent experiments. (**C**) Pie charts depicting the relative levels of adhesion and
1535 endocytic factors in brain, cardiac and hepatic tissues at E18, from all experiments
1536 similar to that described in B. The size of each pie slice is proportional to the sum of
1537 adhesion molecules (including integrin β 1, talin1/2, vinculin and paxillin) or endocytic
1538 accessory factors (including paxillin, CIP4, CHC and Rab5) over all proteins measured.
1539 Paxillin and actin are assigned to dual function (endocytosis and adhesion). Note that
1540 endocytic factors are highly abundant in embryonic brain tissue.

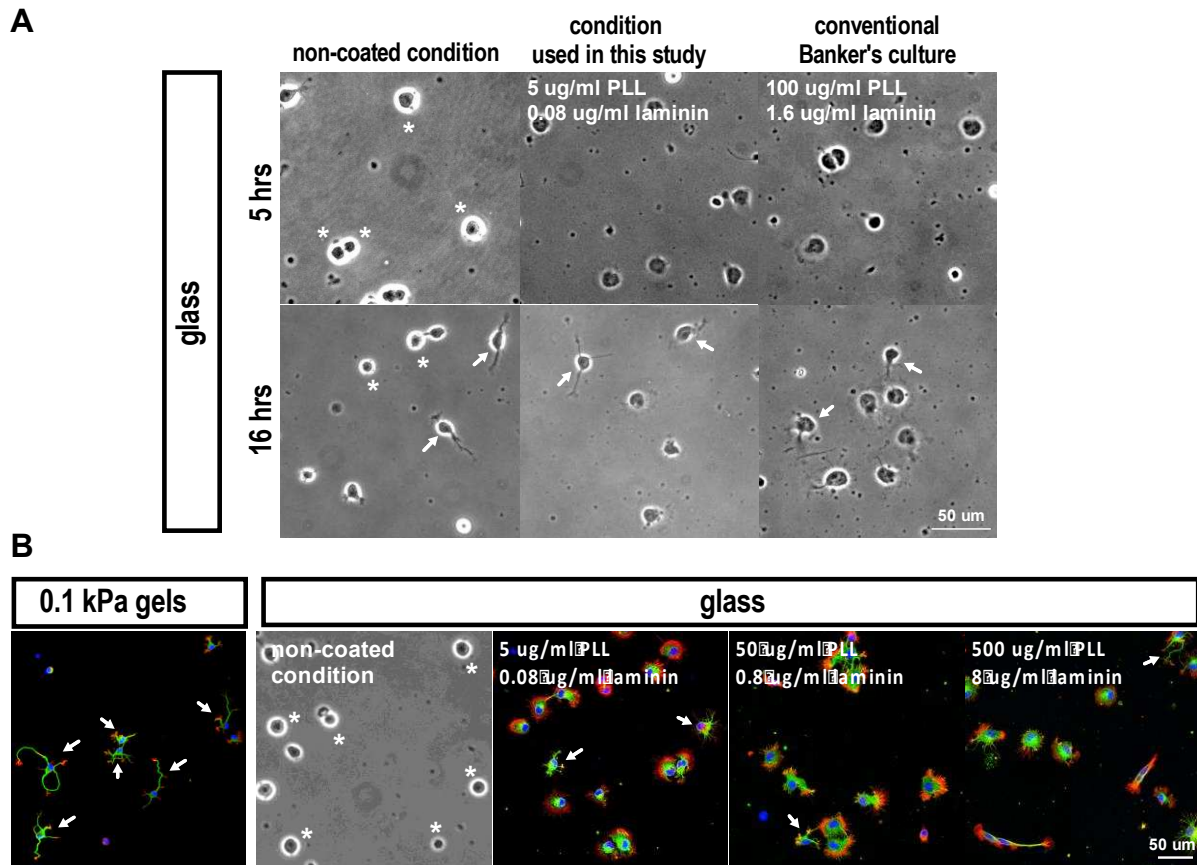
1541

1542 Figure 7– figure supplement 3. Expression time-course of adhesion- or endocytosis-
1543 related proteins in developing mouse cerebral cortex

1544 **A.** Western blots of mouse brain lysates showing protein expression profiles at different
1545 developmental stages (including E13, E15, E18, P1, P4, P7, P14, and adult), as indicated.
1546 **B.** Quantification of protein levels, from all experiments similar to that described in **A**, at
1547 different time-points compared to corresponding levels at E13. Data represents mean
1548 \pm SEM from more than three independent experiments.

1549 **Appendix**

1550



1551

1552 **Appendix—figure 1.**

1553 **A.** Bright-field images of hippocampal neurons cultured on coverslips (glass) coated
1554 under differing conditions for 5 or 16 hours, as indicated.

1555 **B.** Images of neurons grown on 0.1 kPa gels or coverslips with varied coatings for 5
1556 hours, stained for F-actin (phalloidin; red), microtubules (anti-Tuj-1; green), and nuclei
1557 (DAPI; blue). Asterisks mark cells with no lamellipodial protrusions. Arrows mark
1558 neurite-bearing neurons.

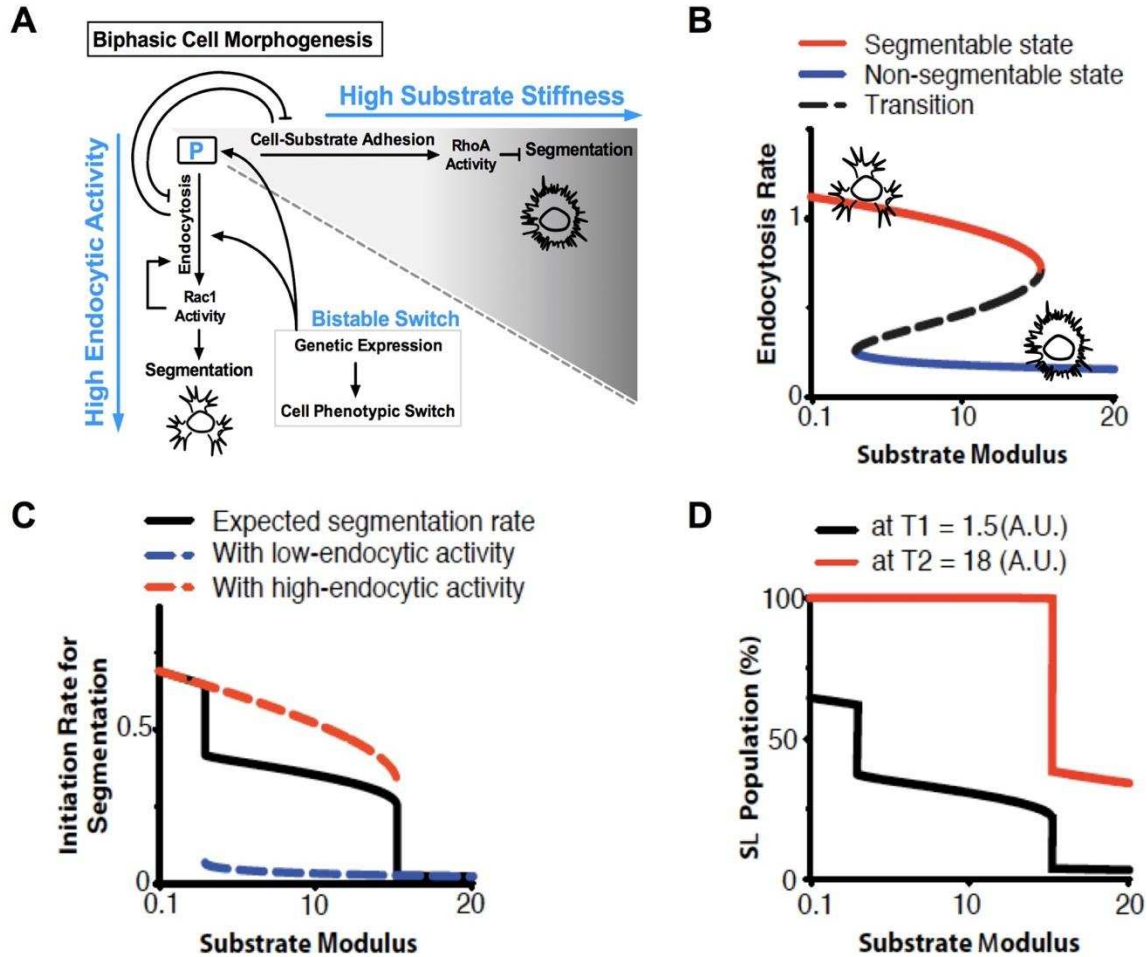
1559

1560

1561

1562

1563



1564

1565 **Appendix—figure 2. Proposed model for the biphasic behavior in neuronal**
 1566 **morphogenesis** (related to Figure 3)

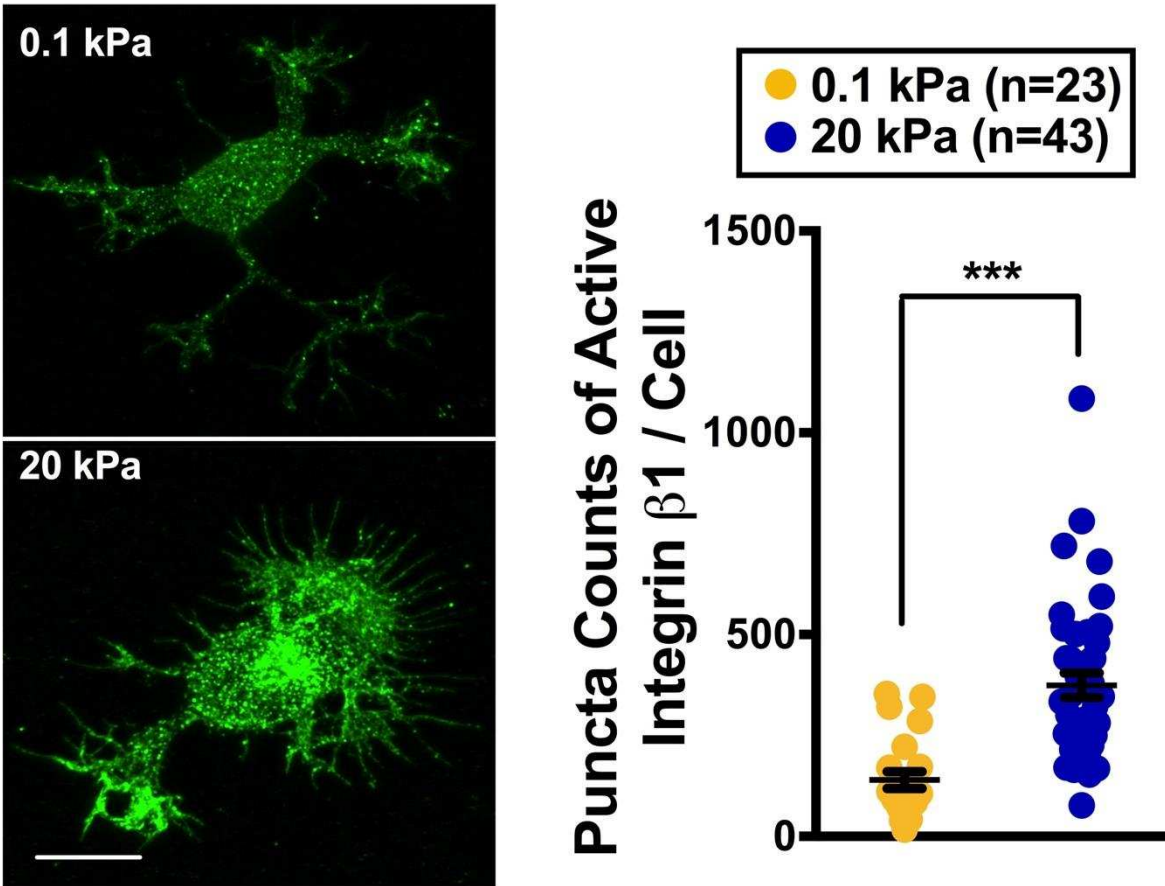
1567 **A.** The probability of segmentation depends on a “P” factor that can bind to both
 1568 endocytosis and adhesion complexes. When bound to the former, P factor enhances
 1569 endocytosis and cells activate Rac1 and expression of factors required for the endocytic
 1570 machinery (including P factor itself), providing a positive feedback that is modulated by
 1571 substrate softness to accelerate segmentation. On stiff substrates, P factor is
 1572 sequestered to cell-substrate adhesions, promoting a low-endocytosis and non-
 1573 segmentable state.

1574 **B.** Numerical simulations show that, based on the proposed model, cells can form a
 1575 bistable switch between a high (Red line) and a low (Blue line) endocytosis state,
 1576 dependent on the substrate modulus.

1577 **C.** Numerical results show that the probability of segmentation depends on the
1578 substrate modulus and endocytic activity.

1579 **D.** Numerical results show delayed onset of lamellipodium segmentation in cells grown
1580 on rigid substrates. For **(B-D)**, see below model for details and parameters.

1581
1582
1583
1584



1585
1586

1587 **Appendix–figure 3. Active Integrin $\beta 1$ staining of neurons grown on 0.1 kPa or 20**
1588 **kPa gels**

1589 Right panel shows representative images of neuronal cultures stained with antibody
1590 specific against activated integrin $\beta 1$ at the 16-hr time points after cell plating. Scale bar:
1591 5 μm . Dot plot: quantification for puncta density of activated integrin $\beta 1$ (n= 23-43 cells
1592 each, “***”, $p < 0.001$; t test).

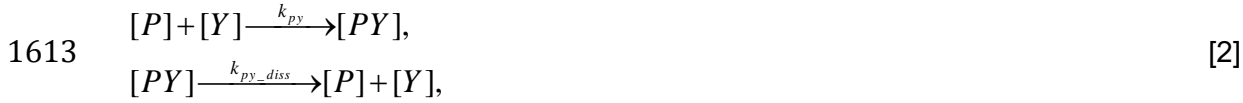
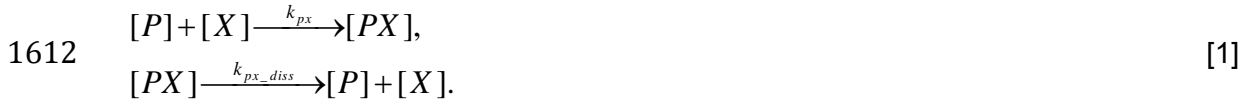
1593 **Appendix- basic assumptions of our model**

1594 To construct our model, we made the following assumptions:

1595 a) There is a common factor (hereafter referred to as the “P factor”) that increases the
 1596 probability of segmentation (and hence neurite formation); b) Both adhesion (for cell substrates)
 1597 and endocytosis complexes bind to the P factor; c) Most P factors are sequestered to either the
 1598 adhesion or the endocytosis complexes; d) Association of P factor with the endocytosis complex
 1599 enhances endocytosis, by which cells can up-regulate the activation of Rac1 and the expression
 1600 of endocytosis-related molecules (including P factor); e) Increasing substrate stiffness enhances
 1601 cell-substrate adhesion, thereby sequestering P factor from binding to the endocytosis complex
 1602 and down-regulating the endocytic rate; f) Expression levels of P factor and the endocytic
 1603 machinery are co-regulated; and g) The probability of segmentation depends on Rac1 activity.

1604 To simplify our analysis, we grouped the endocytic complex (or machinery) and the
 1605 adhesion complex (or machinery) into single entities denoted as X and Y, respectively. Because
 1606 we assumed that the expression of P factor and the endocytic machinery is co-regulated, we set
 1607 the total expression level of P factor $[P_{Total}]$ (represented by the concentration inside the cell) as
 1608 being proportional to the total expression level of X $[X_{Total}]$ according to $P_{Total} \approx e_{PX} \times X_{Total}$, where
 1609 e_{PX} is a constant.

1610 The chemical balance between the association and dissociation of P factor with X and Y
 1611 follows:



1614 with the constraint $[PX] + [PY] + [P] = [P_{Total}]$, $[PX] + [X] = [X_{Total}]$, and $[PY] + [Y] = [Y_{Total}]$, where
 1615 $[P_{Total}]$, $[X_{Total}]$, and $[Y_{Total}]$ are the total expression levels of P factor, the adhesion complex
 1616 machinery, and the endocytosis complex machinery, respectively. We assumed that most P
 1617 factors are sequestered to either the endocytosis or the adhesion complex, and free-form P
 1618 factor is limited (i.e., $[P] \ll 1$). As such, the quasi-steady state concentration of PX and PY can
 1619 be estimated as:

$$1620 \quad [PX] = \frac{k_{px}[P][X_{Total}]}{k_{px_diss} + k_{px}[P]} \approx k_{px}k_{px_diss}^{-1}[P][X_{Total}], \tag{3}$$

$$[PY] = \frac{k_{py}[P][Y_{Total}]}{k_{py_diss} + k_{py}[P]} \approx k_{py}k_{py_diss}^{-1}[P][Y_{Total}].$$

1621 Consequently, we have:

$$1622 \quad [P] \approx \frac{[P_{Total}]}{1 + k_{py}k_{py_diss}^{-1}[Y_{Total}] + k_{px}k_{px_diss}^{-1}[X_{Total}]}, \tag{4}$$

$$\rightarrow [PX] \approx \frac{k_{px}k_{px_diss}^{-1}e_{PX}[X_{Total}]^2}{1 + k_{py}k_{py_diss}^{-1}[Y_{Total}] + k_{px}k_{px_diss}^{-1}[X_{Total}]}.$$

1623 For simplicity, we further assumed that the endocytic rate is proportional to $[PX]$.

1624 *Endocytic rate* $\propto [PX]$. [5]

1625

1626 **Analysis of two-state behavior**

1627 Next, we considered the equation for endocytosis-induced up-regulation of the expression of P
 1628 factor and the endocytic machinery. We used a simple approach in that the endocytosis-induced
 1629 up-regulation follows Michaelis–Menten kinetics (Michaelis, Menten et al., 2011). Based on the
 1630 assumption that the endocytic rate is proportional to $[PX]$ (Eqn. [5]), we have:

$$1631 \quad \frac{d[X_{Total}]}{dt} = k_{deg} \left(X_0 + X_{up} \frac{[PX]}{PX_T + [PX]} - [X_{Total}] \right), \quad [6]$$

1632 where k_{deg} is the degradation rate, X_0 is the baseline expression in the absence of endocytosis-
 1633 induced up-regulation, X_{up} is the efficacy for endocytosis-induced up-regulation. Michaelis–
 1634 Menten kinetics use a constant PX_T as the threshold for $[PX]$ to reach half the maximum level of
 1635 up-regulation. Substituting Eqn. [4] into Eqn. [6], we have:

$$1636 \quad \frac{d[X_{Total}]}{k_{deg} dt} = X_0 + \frac{X_{up} k_{px} k_{px_diss}^{-1} e_{PX} [X_{Total}]^2}{PX_T (1 + k_{py} k_{py_diss}^{-1} [Y_{Total}] + k_{px} k_{px_diss}^{-1} [X_{Total}]) + k_{px} k_{px_diss}^{-1} e_{PX} [X_{Total}]^2} - [X_{Total}]. \quad [7]$$

1637

1638 We further simplified Eqn. [7] by setting $\tau = k_{deg} t$, $\beta = e_{PX} X_0 / PX_T$, $\alpha = e_{PX} X_{up} / PX_T$, $x =$
 1639 $e_{PX} [X_{Total}] / PX_T$, and $y = e_{PX} (1 + k_{py} [Y_{Total}] / k_{py_diss}) / (k_{px} PX_T / k_{px_diss})$ and obtained :

$$1640 \quad \frac{dx}{d\tau} = \beta + \frac{\alpha x^2}{y + x + x^2} - x, \quad [8]$$

$$1641 \quad \text{Endocytosis rate} \propto [PX] \approx PX_T \frac{x^2}{x + y} \propto \frac{x^2}{x + y}. \quad [9]$$

1642 Here, variable x is related to the expression level of the endocytic machinery (including P
 1643 factor). Variable y is related to cell-substrate adhesion and increases with substrate stiffness.
 1644 For simplicity, we approximated y with a linear dependence on the substrate modulus; namely, y
 1645 $= y_0 + y_1 \times$ substrate modulus, where y_0 and y_1 are constants. The steady-state solutions of Eqn.
 1646 [8] can be found by solving its null-clines in the x - y plane, which read:

$$1647 \quad y = \frac{\alpha x^2}{x - \beta} - x(x + 1). \quad [10]$$

1648 An example of Eqn. [10] is illustrated in Fig. S6 B, in which we use a linear relationship to
 1649 link the substrate modulus with the variable y (i.e., $y = y_0 + y_1 \times$ substrate modulus) and to set
 1650 the endocytic rate as a function of x and y (Eqn. [9]). Analysis of Eqn. [10] revealed that for a
 1651 given y , two stable steady-state solutions of x could coexist (the two solid lines in Fig. S6 B) with
 1652 one unstable transition-state solution (the dotted line in Fig. S6 B), provided that the following
 1653 criterion is satisfied:

$$1654 \quad (\alpha - 2\beta - 1)^3 \geq 27\alpha\beta^2. \quad [11]$$

1655 Under such a condition, cells possess the ability to perform a bistable switch between a high- x
1656 state and a low- x state for a given y (i.e., substrate stiffness). Here, the high- x state corresponds
1657 to the endocytosis-dominant state where the cells exhibit a higher endocytic rate, higher Rac1
1658 activation, and higher expression of the endocytic machinery (including P factor). In comparison,
1659 the low- x state corresponds to the adhesion-dominant state with lower Rac1 activation and
1660 lower expression of the endocytic machinery. For convenience, hereafter we define $S(x, y)$ as
1661 the state for a given set of (x, y) . Furthermore, for any given y , we define $S_{end}(x_{end}(y), y)$ as the
1662 corresponding endocytosis-dominant state, with $x_{end}(y)$ as the steady-state solution from Eqn.
1663 [10]. Likewise, we define $S_{adh}(x_{adh}(y), y)$ as the adhesion-dominant state for a given y , with
1664 $x_{adh}(y)$ as the steady-state solution. Similarly, $S_{tx}(x_{tx}(y), y)$ defines the transition state for a given
1665 y , with $x_{tx}(y)$ as the steady-state solution.

1666

1667 **Statistics of two-state behavior**

1668 The distribution of the proposed two states at a given substrate modulus (i.e., y) can be
1669 estimated by rewriting Eqn. [8] into a Langevin equation followed by adopting a free energy
1670 approach (Lemons & Gythiel, 1997, Mossa & Clementi, 2007). The “free energy” is then used to
1671 estimate the probability of finding one cell at a given state. Furthermore, the free energy can be
1672 used to estimate the rate at which the cells switch from one state to another. Specifically, we
1673 approximated Eqn. [8] as the derivative of a free energy, $F(x, y)$, and added a time-dependent
1674 Gaussian white noise η of width D to the system:

$$1675 \quad \frac{dx}{d\tau} = \beta + \frac{\alpha x^2}{y + x + x^2} - x + \eta(\tau) = -\frac{dF(x, y)}{dx} + \eta(\tau),$$

1676 [12]

1677 where

$$1678 \quad \begin{aligned} \langle \eta(\tau)\eta(\tau') \rangle &= D\delta(\tau - \tau'), \\ \langle \eta(\tau) \rangle &= 0, \end{aligned} \tag{13}$$

$$1679 \quad F(x, y) = C - (\alpha + \beta)x - \frac{x^2}{2} + \frac{\alpha}{2} \ln(y + x + x^2) + \frac{\alpha}{2} \times \begin{cases} \frac{(y-1/2)}{\sqrt{|y-1/4|}} \ln \left(\frac{x+1/2 - \sqrt{|y-1/4|}}{x+1/2 + \sqrt{|y-1/4|}} \right), & y < 1/4 \\ \frac{1}{x+1/2}, & y = 1/4, \\ \frac{2(y-1/2)}{\sqrt{|y-1/4|}} \tan^{-1} \left(\frac{x+1/2}{|y-1/4|} \right), & y > 1/4 \end{cases}$$

1680 [14] with C as an integral constant. The probability of finding one cell at a state $S(x, y)$, denoted
1681 as $f(x, y)$, is then specified by the free energy as:

$$1683 \quad f(x, y) \propto \exp[-F(x, y)/D], \tag{15}$$

1684 or

1685
$$f(x, y) = \frac{e^{-F(x,y)/D}}{\int dx e^{-F(x,y)/D}}. \quad [16]$$

1686 Note that in Eqn. [16], x does not need to be the steady-state solution from Eqn. [10]. For the
 1687 bistable regime where cells are allowed to select one of the steady states at a given y (provided
 1688 that Eqn. (11) is satisfied) or switch from one state to another, the rate at which the switch
 1689 occurs can be estimated by Transition State Theory, Eyring theory, Arrhenius' law, or Kramers'
 1690 law (Goychuk, Jung et al., 2010, Wodkiewicz, 1984). For instance, for a cell in the endocytosis-
 1691 dominant state, the average rate at which it switches to the adhesion-dominant state, $k_{end \rightarrow adh}$,
 1692 can be calculated by the mean first passage time by which the cell moves from the endocytosis-
 1693 dominant state $S_{end}(x_{end}(y), y)$ to the transition state $S_{tx}(x_{tx}(y), y)$, $\tau_{end \rightarrow tx}$, in the free energy
 1694 landscape $F(x, y)$. Likewise, the average rate at which the cell switches from the adhesion-
 1695 dominant state to the endocytosis-dominant state, $k_{adh \rightarrow end}$, can be calculated by the mean first
 1696 passage time $\tau_{adh \rightarrow tx}$. Following Transition State Theory, Eyring theory, Arrhenius' law, or
 1697 Kramers' law (Goychuk et al., 2010, Wodkiewicz, 1984), we establish the switch rate at a given
 1698 y as:

1699 $k_{end \rightarrow adh}(y) \sim k_0 \times \exp[(F(x_{end}(y), y) - F(x_{tx}(y), y))/D],$
 1700 $k_{adh \rightarrow end}(y) \sim k_0 \times \exp[(F(x_{adh}(y), y) - F(x_{tx}(y), y))/D], \quad [17]$

1701 where k_0 is a constant.

1702

1703 Segmentation rate in the two-state system

1704 In our model, we assumed that the probability of segmentation depends on Rac1 activity, which
 1705 is primarily induced by endocytosis. To estimate the segmentation rate, hereafter defined as
 1706 $k_s(x, y)$, we approximated it as being proportional to the endocytic rate (Eqns. [5] and [9]),
 1707 namely:

1708 $Segmentation\ rate\ k_s(x, y) \propto Endocytosis\ rate \sim \frac{x^2}{x + y}. \quad [18]$

1709 Examples of the segmentation rates from Eqn. [18] are illustrated in Fig. S6 C, where the rates
 1710 for the endocytosis-dominant and adhesion-dominant states are plotted. For a given y , the
 1711 expected rate of segmentation in a population of cells was estimated as:

1712 $Expected\ Segmentation\ rate\ \langle k_s(y) \rangle \sim \frac{f(x_{adh}(y), y) \frac{x_{adh}^2}{x_{adh} + y} + f(x_{end}(y), y) \frac{x_{end}^2}{x_{end} + y}}{f(x_{adh}(y), y) + f(x_{end}(y), y)}$
 1713 $= \frac{e^{-F(x_{adh}(y), y)/D} \frac{x_{adh}^2}{x_{adh} + y} + e^{-F(x_{end}(y), y)/D} \frac{x_{end}^2}{x_{end} + y}}{e^{-F(x_{adh}(y), y)/D} + e^{-F(x_{end}(y), y)/D}}. \quad [19]$

1714

1715 Segmentation dynamics in the two-state system

1716 Finally, we estimated the dynamics of a population of cells that progressively switched to the
 1717 segmented state. To do so, we assumed that cells were initially in the adhesion-dominant state,
 1718 and defined the density of cells in the adhesion-dominant state as $n_{adh}(\tau)$ for a given time τ , the

1719 density of cells in the endocytosis-dominant state as $n_{end}(\tau)$, and the density of cells that formed
 1720 segments as $n_{seg}(\tau)$, with the following constraints: $n_{adh}(0) = 1$, $n_{end}(0) = 0$, and $n_{adh}(\tau) + n_{end}(\tau) +$
 1721 $n_{seg}(\tau) = 1$. The dynamics for these cells are as follows:

$$\frac{dn_{adh}}{d\tau} = -k_s(x_{adh}(y), y)n_{adh} - k_{adh \rightarrow end}(y)n_{adh} + k_{end \rightarrow adh}(y)n_{end},$$

1722 $\frac{dn_{end}}{d\tau} = -k_s(x_{end}(y), y)n_{end} + k_{adh \rightarrow end}(y)n_{adh} - k_{end \rightarrow adh}(y)n_{end},$

$$\frac{dn_{seg}}{d\tau} = k_s(x_{adh}(y), y)n_{adh} + k_s(x_{end}(y), y)n_{end}.$$

1723 [20]

1724 Examples of the segmentation dynamics in a population of cells are illustrated in Fig. S6 D,
 1725 where the contributions from cells in the endocytosis-dominant or the adhesion-dominant states
 1726 is plotted separately.

1727

1728 **Parameters used in the figures**

1729 To simulate the segmentation dynamics illustrated in **Appendix-figure 1**, we set $\alpha = 2.5$, $\beta =$

1730 0.1 , $k_0 = 1$, $D = 1$, and $y = 0.7 + 10^{-5} \times$ substrate rigidity, and used Eqns. [10], [17], [18], and [20].

1731

1737
1738

Appendix–Table 3. Paxillin-associating protein identified by liquid chromatography-tandem mass spectrometry

Table S3. Paxillin-associating protein identified by liquid chromatography-tandem mass spectrometry (related to Fig. 4)

Category	Protein ID	Score	MW	MW _{obs}
Endocytosis	clathrin heavy chain 1	68	190	190
	dynammin-1-like protein isoform X17	84	80	80
Adhesion	talin-1	159	270	270
Cytoskeleton dynamics	drebrin isoform X3	90	72	120
	alpha-internexin	70	56	60
	citron Rho-interacting kinase	63	235	270
	protein unc-45 homolog B isoform X1	243	103	105
Transcription/	matrin-3	152	94	120
Translation	elongation factor 1-alpha 1	94	50	49
	eukaryotic translation initiation factor 3 subunit A	114	163	180
	eukaryotic translation initiation factor 3 subunit B	57	90	120
	eukaryotic translation initiation factor 3, subunit 6 interacting protein	51	66	65
	heterogeneous nuclear ribonucleoprotein M, isoform X2	98	64	75
	AT-rich interactive domain-containing protein 1B isoform X3, partial	58	58	63
	heterogeneous nuclear ribonucleoprotein A2/B1	181	38	37
Protein quality control	heat shock protein 60 kDa precursor	171	61	60
control	heat shock cognate 71 kDa protein	182	71	75
	heat shock protein 90 kDa alpha, class B member 1	222	83	95
	T-complex protein 1 subunit alpha	79	60	60
	T-complex protein 1 subunit gamma	79	60	60
	protein unc-45 homolog B isoform X1	243	103	105
	stress-70 protein	70	74	75
Signaling transduction	calcium/calmodulin-dependent protein kinase II, beta 3 isoform	67	65	65
DNA repair	fanconi anemia group C protien homolog	73	64	60
Metabolism	glyceraldehyde-3-phosphate dehydrogenase	192	36	36

1739
1740

1741

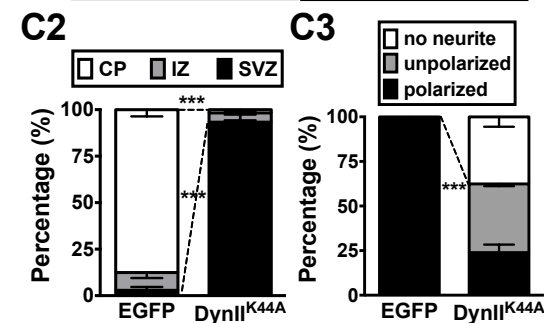
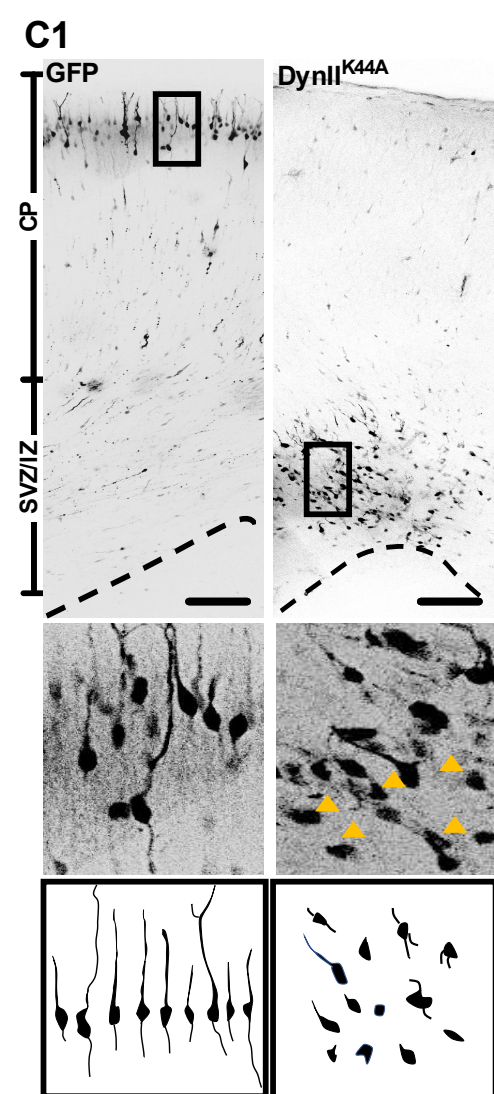
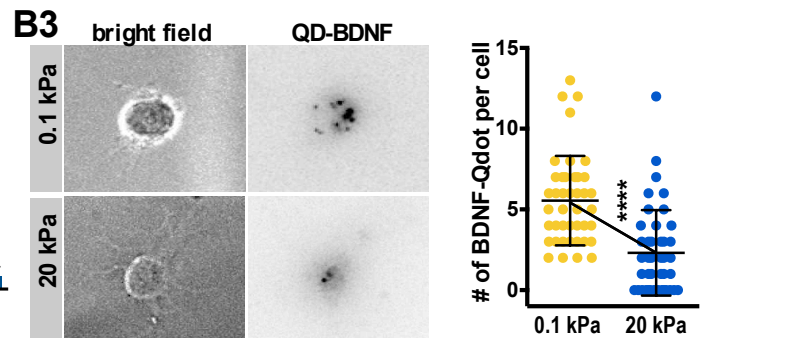
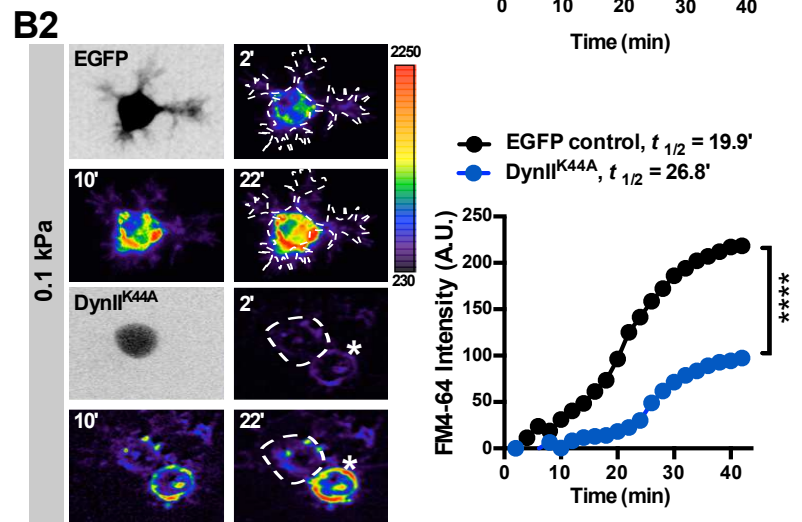
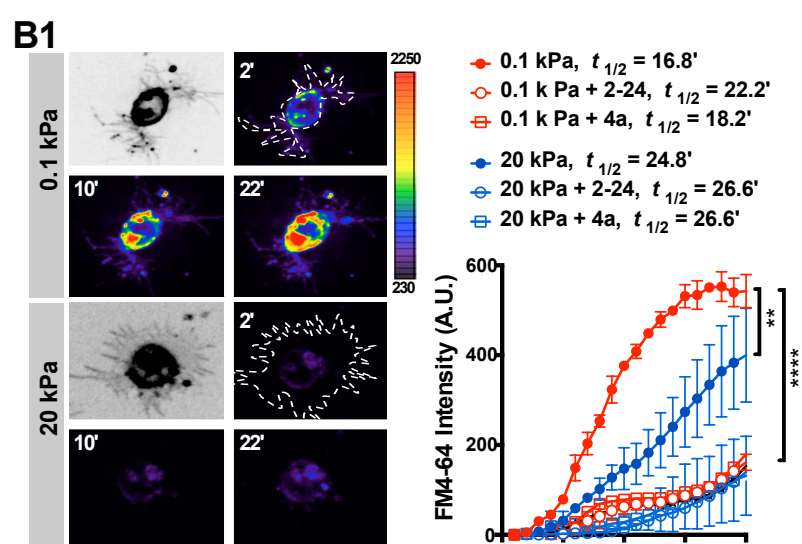
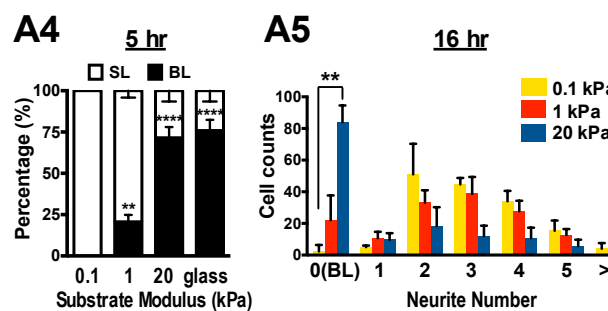
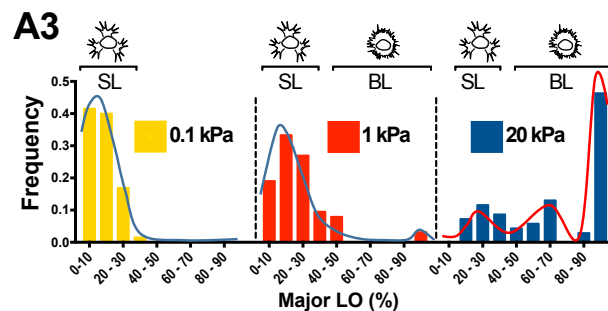
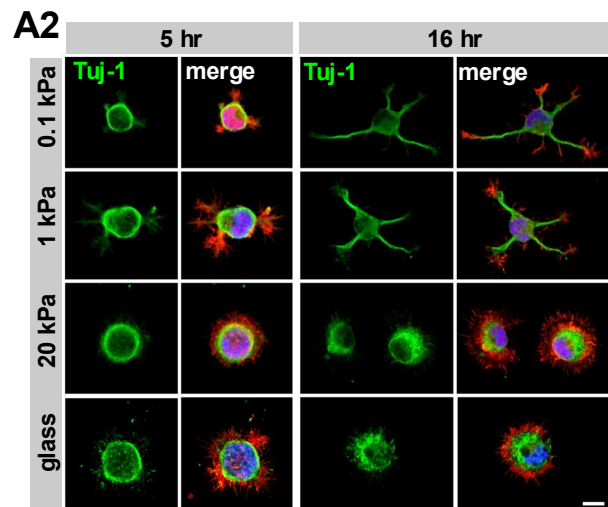
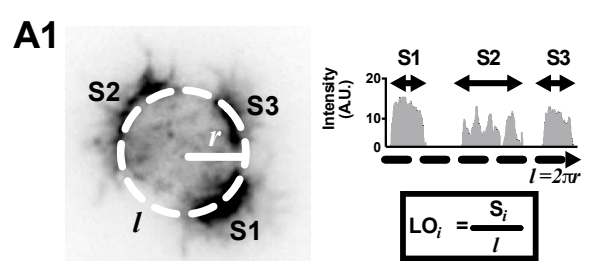
1742

1743

1744

1745

1746



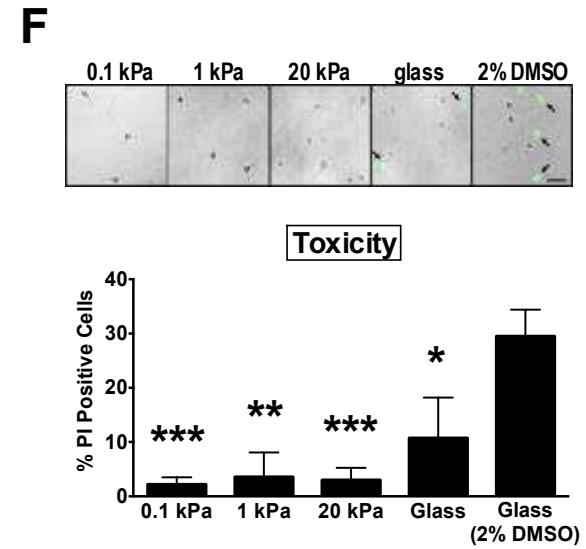
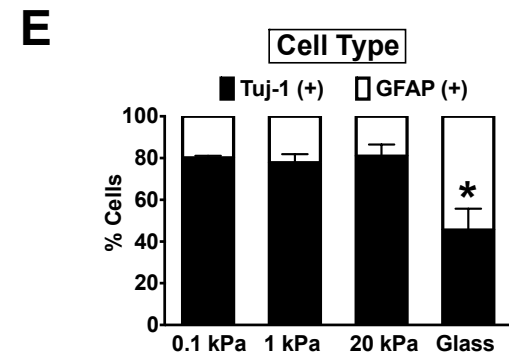
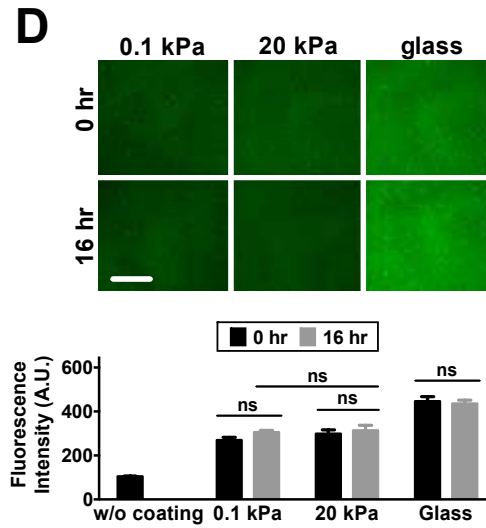
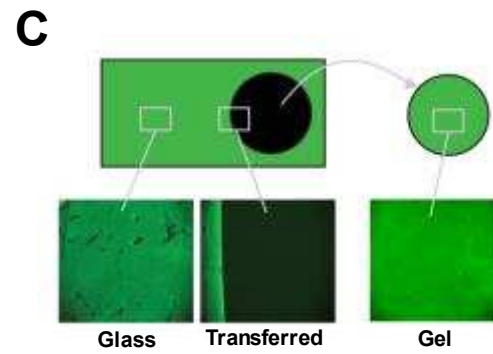
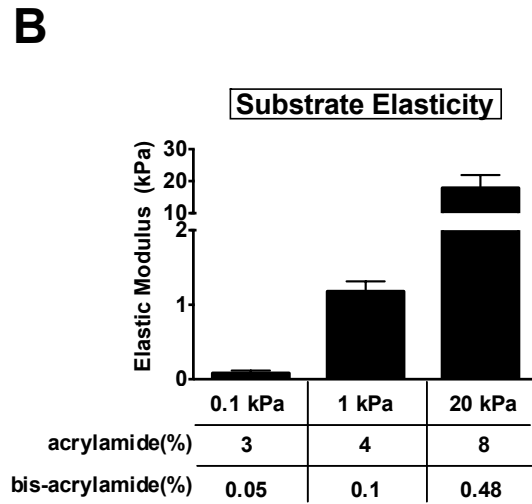
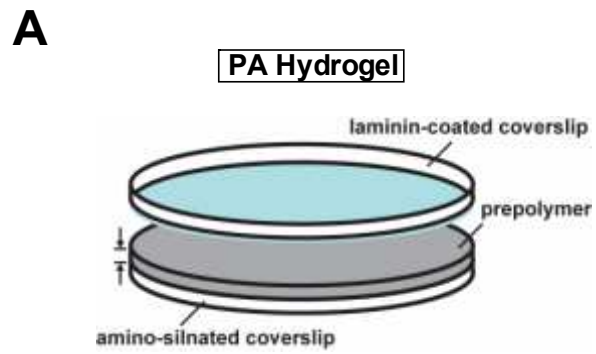


Figure 1-figure supplement 1

Figure 1-figure supplement 1

Hippocampal neurons cultured on polyacrylamide hydrogels of varying stiffness

A. Schematic of the three-layer assembly of polyacrylamide (PA) hydrogels (diameter=1.8 mm, thickness=200 μm). Light blue, the poly-L-Lysine/laminin-coated side of the coverslip.

B. Atomic force microscopy measurement of elastic modulus (\pm SEM, $n=3$) of PA gels. Table shows the ratio of acrylamide and bis-acrylamide used to determine the crosslink density and the stiffness (0.1 kPa, 1 kPa, and 20 kPa) of the polymers.

C, D. Transfer printing of laminin on hydrogels. (C) Representative images of PA hydrogel peeled from laminin-coated coverslips, both immunostained with antibodies against laminin (shown in green). Note that laminin was completely transferred from the laminin-coated coverslip to the gel surface. (D) Quantification of laminin fluorescence intensity (\pm SEM, $n>3$; “ns”, no significance; *t-test*) on the gel surface before and after incubation for 16 hr with culture medium. Acid-washed coverslips were pre-coated with laminin (a stock concentration of 1.62 mg/ml) in a 1:50 dilution. Note that the staining intensity of surface laminin was comparable between 0.1 kPa and 20 kPa gels.

E. Cell type enrichment analysis for hippocampal cultures. Cultured neurons plated on substrates were immunostained with antibodies against the neuron-specific marker Tuj-1 and the astroglial marker glial fibrillary acidic protein (GFAP). Histogram showing percentages (\pm SEM; $n>200$ cells for each group from more than three independent experiments; “*”, $p < 0.05$; relative to that of 0.1 kPa culture, *t-test*) of Tuj-1- or GFAP-positive cells in hippocampal cultures at 3 days in vitro (DIV).

F. Cell viability analysis for hippocampal neurons cultured on PA gels and glass. DIV3 cultures were subjected to propidium iodide (PI) staining. Arrow, apoptotic cells with fragmented nuclei (PI positive). Dimethyl sulfoxide (2%) was used as a positive control of maximum cytotoxicity. Data represent mean \pm SEM ($n>200$ cells for each group from more than three independent experiments; “*”, $p < 0.05$; “****”, $p < 0.001$; relative to that of glass culture, *t-test*).

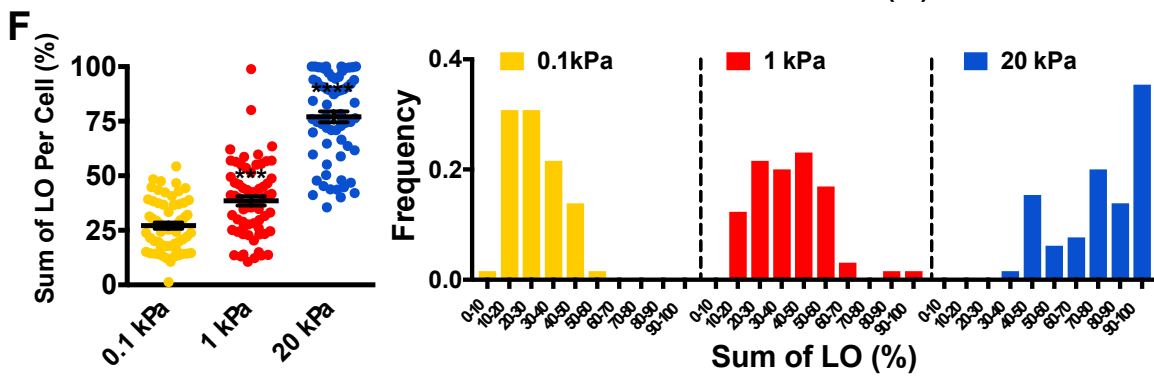
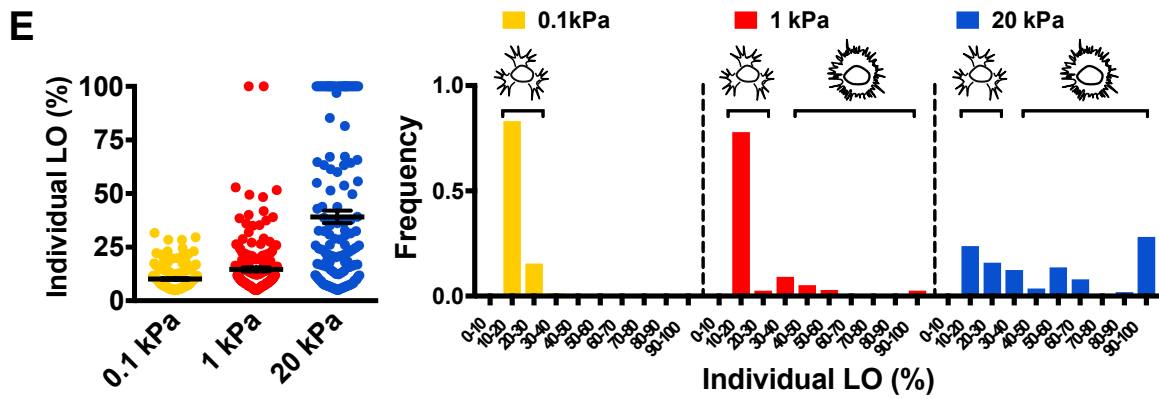
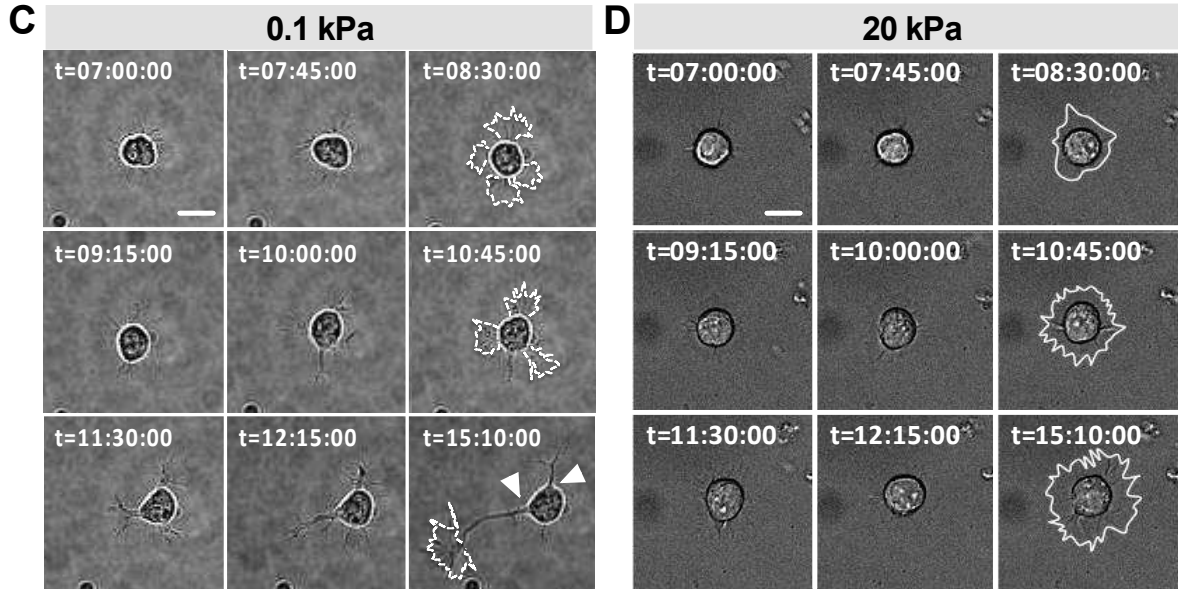
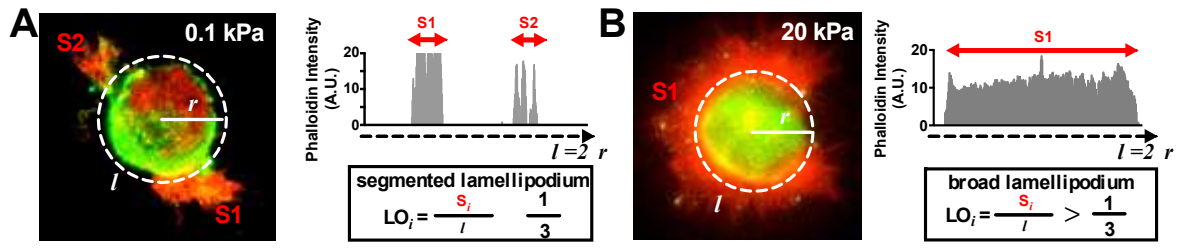


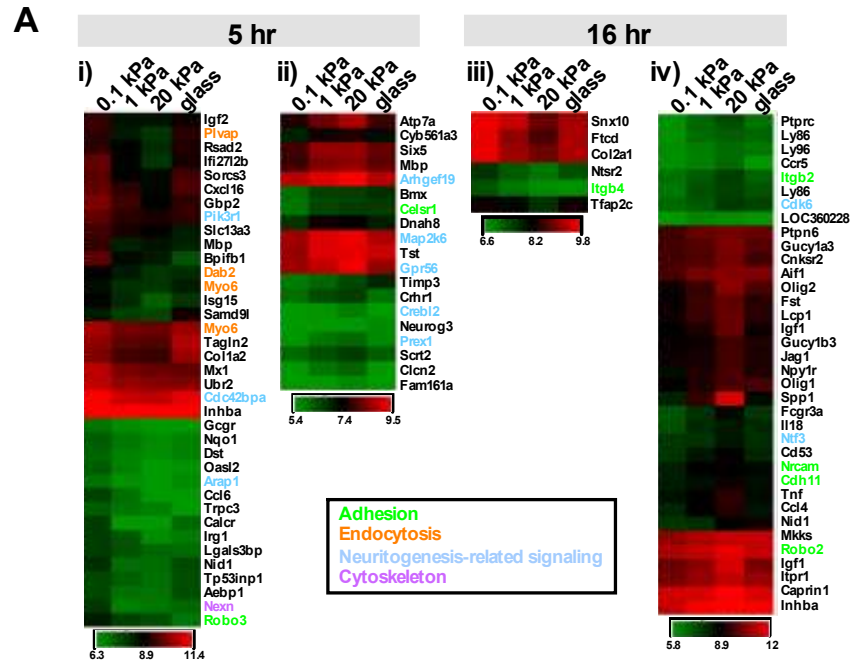
Figure 1– figure supplement 2

Differential lamellipodium phenotypes of neurons grown on hydrogels

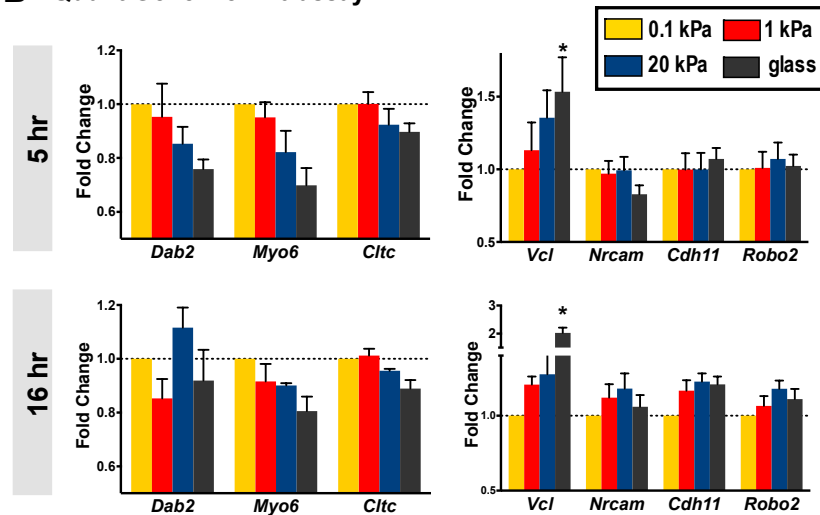
A, B. Phalloidin intensity profiling of neurons on soft ($E=0.1$ kPa; **A**) and stiff ($E=20$ kPa; **B**) hydrogels stained with phalloidin (Red) for F-actin filaments and antibodies against Tuj-1 (Green), as indicated. Lamellipodium occupancy (LO) of phalloidin-positive segments (“S”) along the cell periphery was calculated according to the formula shown in the lower panel. Cells exhibiting typical morphologies of the segmented lamellipodium (“SL”, A) or broad lamellipodium (“BL”, B) are shown.

C, D. Time-lapse bright-field images of newly plated neurons on 0.1 kPa (C) or 20 kPa (D) gels. Note that neurite initiation sites (arrowheads at time-point=15:10:00) are correlated with the positions of initial segmented lamellipodia (delimited by the dashed line in panel C; individual LO < 0.33). Broad lamellipodia of a neuron grown on a 20 kPa gel are delimited by solid lines in panel D. Scale bar = 20 μm .

E, F. Distribution of individual lamellipodium occupancy (E) and total lamellipodium occupancy (F) from the same sets of experiments shown in main Figure 1A3. Simplified drawings above histograms illustrate the typical segmented lamellipodium and broad lamellipodium phenotypes of hippocampal neurons grown on soft ($E = 0.1$ kPa or 1 kPa) and stiff ($E = 20$ kPa) PA hydrogels.



B QuantiGene Plex 2.0 assay



C smRNA FISH

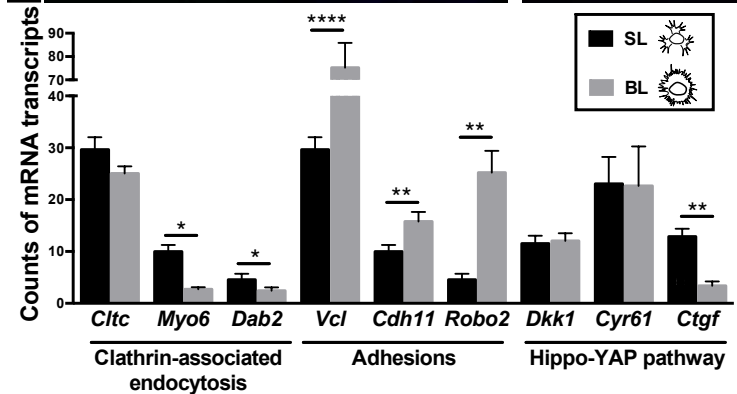
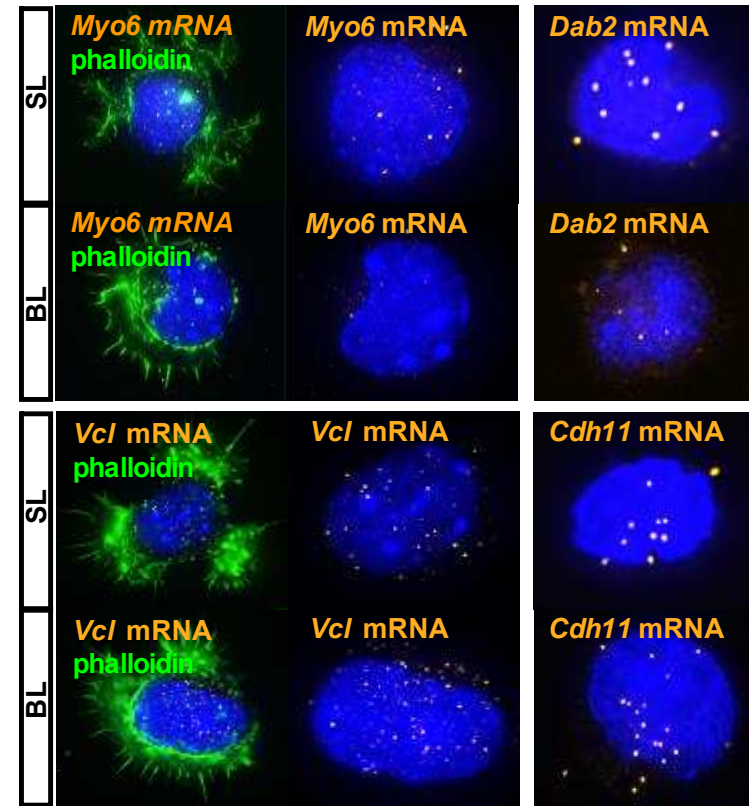


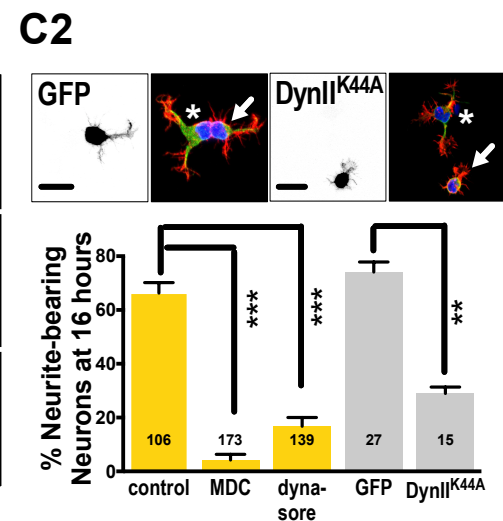
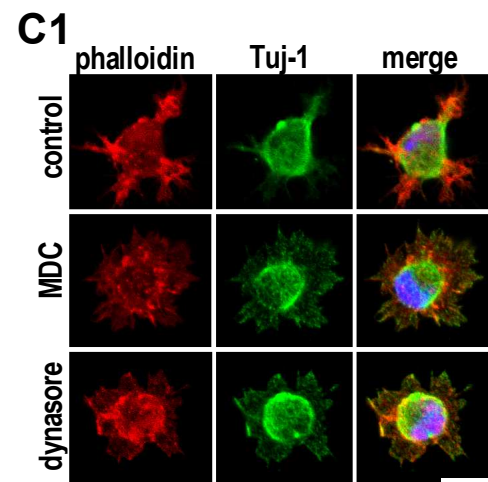
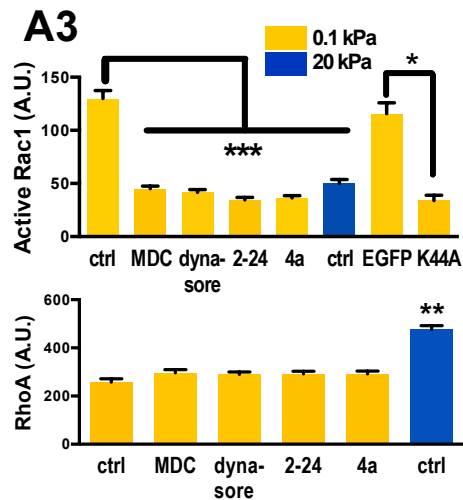
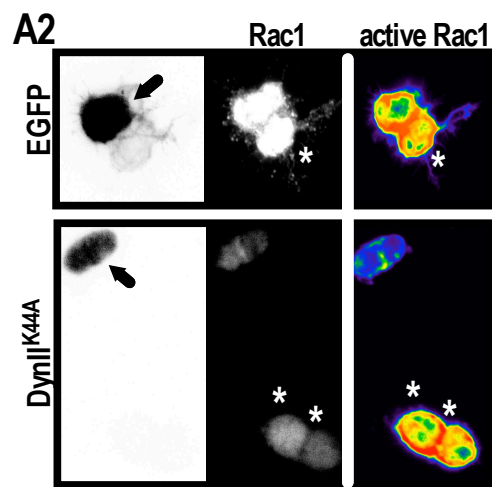
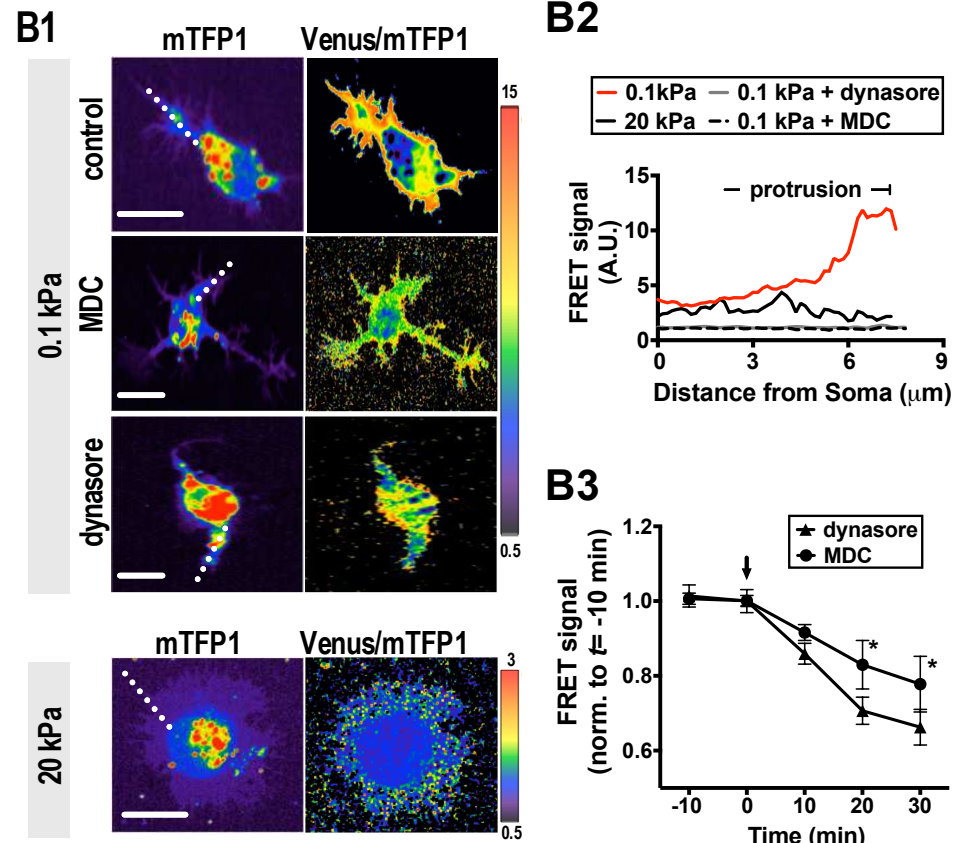
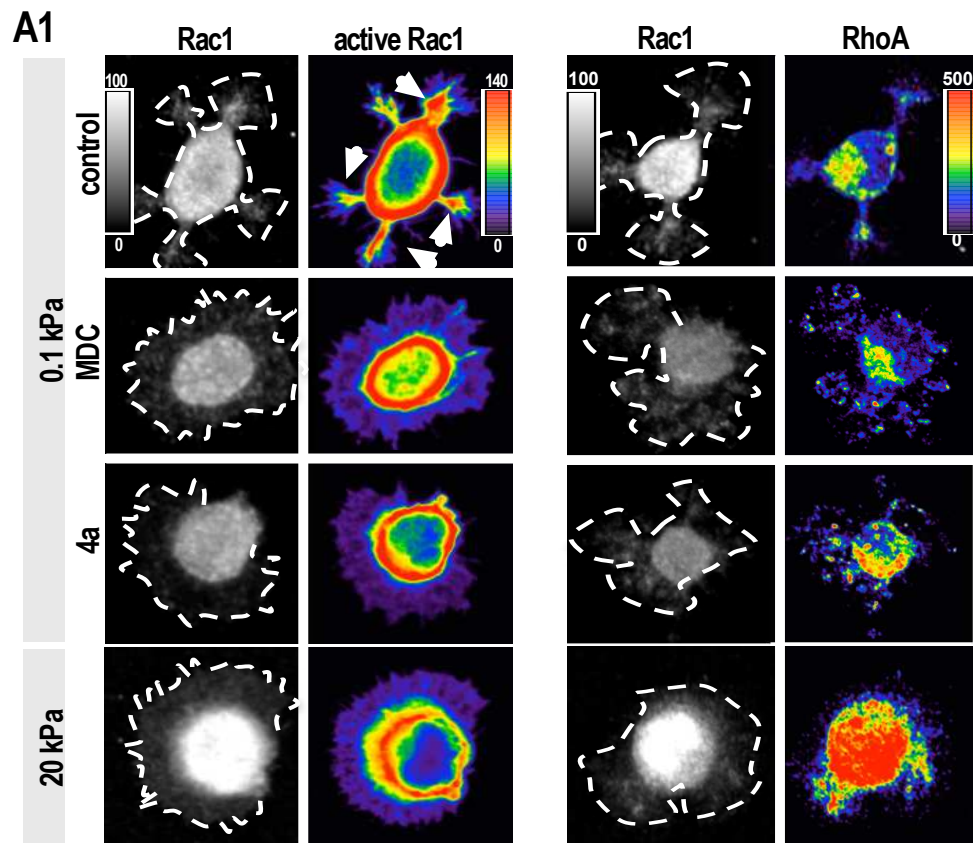
Figure 1– figure supplement 3

Differential gene expression pattern of neurons grown on hydrogels

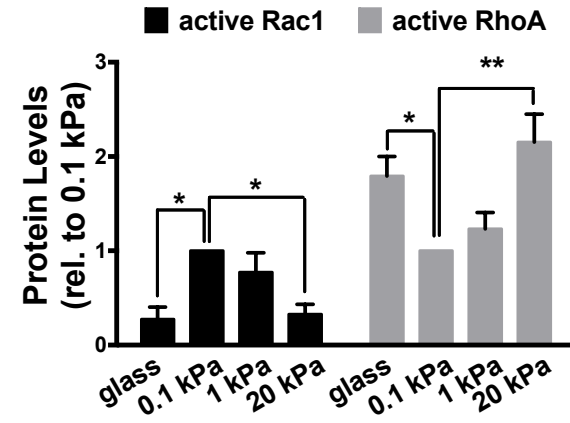
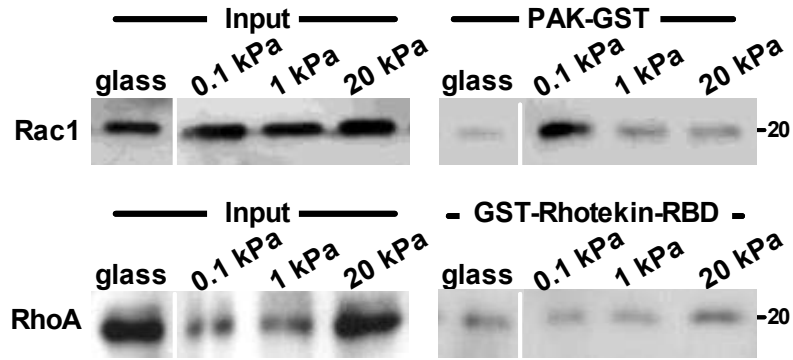
A. Up-regulation of clathrin-associated endocytosis genes in 0.1 kPa cultures. Gene expression patterns emerging from microarray analysis were grouped into four modules: expression increased with substrate softness in 5 hr (i) or 16 hr (iii) cultures, or increased with substrate stiffness in 5 hr (ii) or 16 hr (iv) cultures (cut off: >1.5-fold change, $p < 0.05$, $n = 3$ independent experiments). Normalized expression levels are represented by a color-coded heatmap.

B. A QuantiGene Plex branched-chain DNA amplification assay validated the relatively increased levels of mRNAs encoding the clathrin-associated endocytosis factors Dab2, Myo6, and Cltc in neurons grown on 0.1 kPa gels. Data represent fold changes in RNA levels (\pm SEM; $n = 4-5$ independent experiments; relative to that of 0.1 kPa culture; “*”, $p < 0.05$; t test).

C. Representative single-molecule RNA fluorescence in situ hybridization (smRNA FISH) images of mRNA encoding Myo6, Dab2, Chd11, Vcl, or Cry61 on segmented lamellipodium (SL) or broad lamellipodium (BL) neurons in 5 hr cultures, as indicated. Histograms showing average number (\pm SEM; $n = 42-52$ cells; “*”, $p < 0.05$; “***”, $p < 0.01$; “*****”, $p < 0.0001$; t test) of smRNA FISH puncta for each gene per single neurons of the SL and BL cells.



A



B

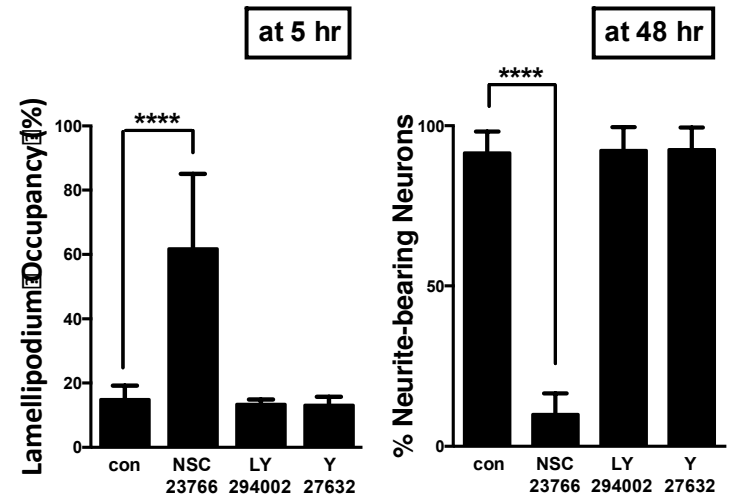
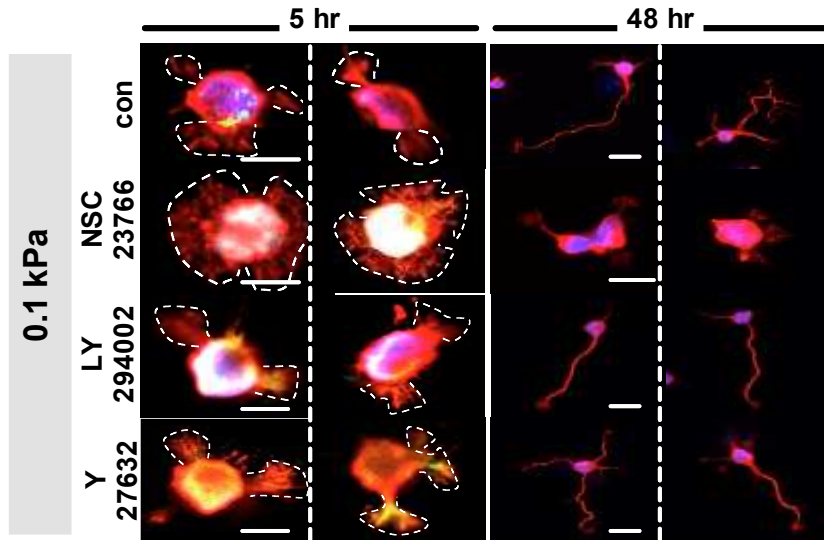
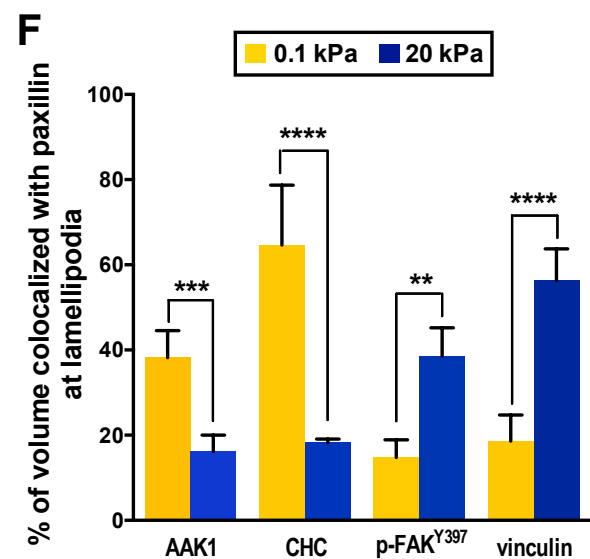
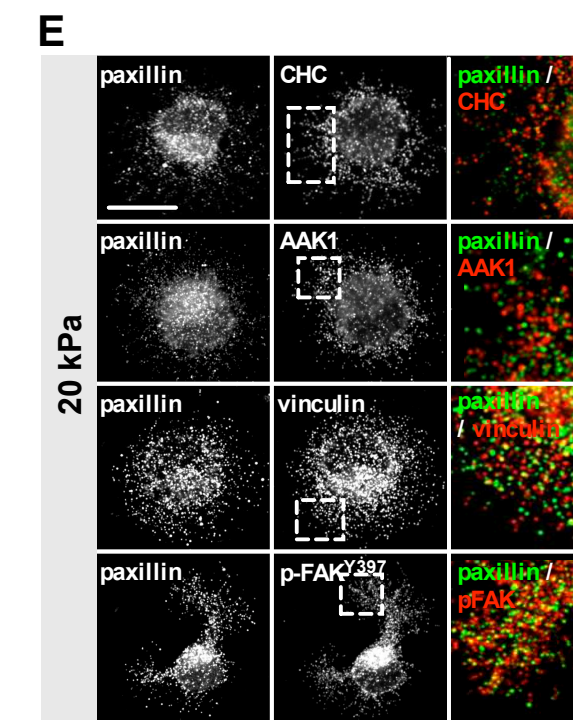
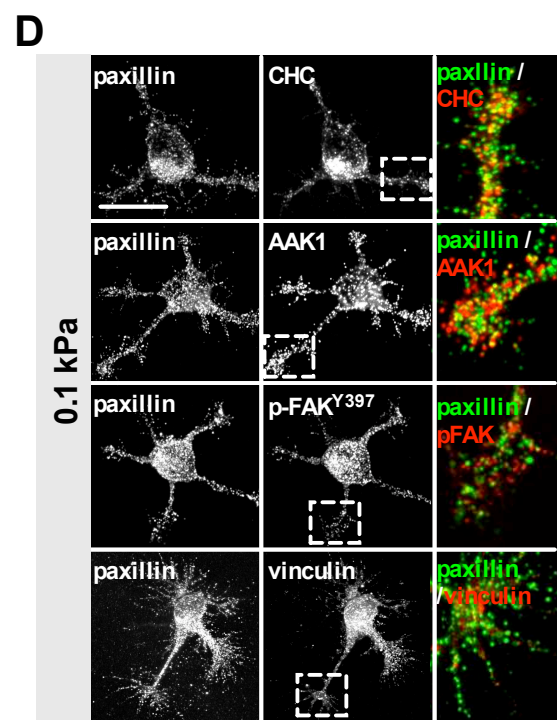
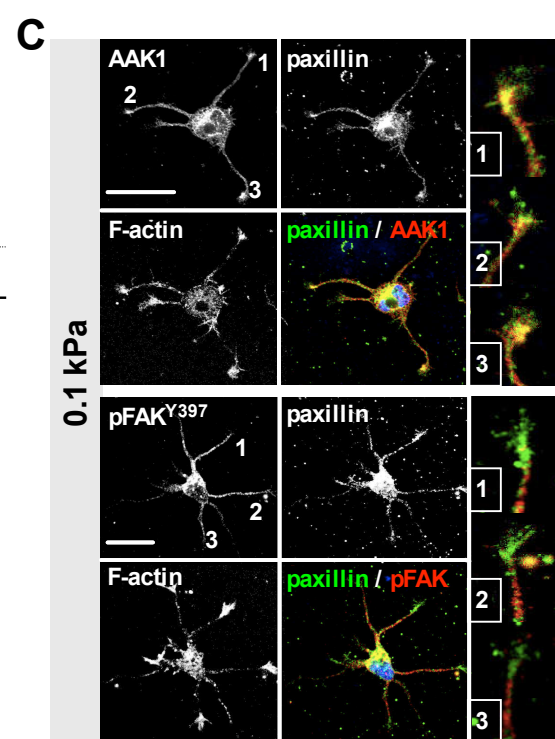
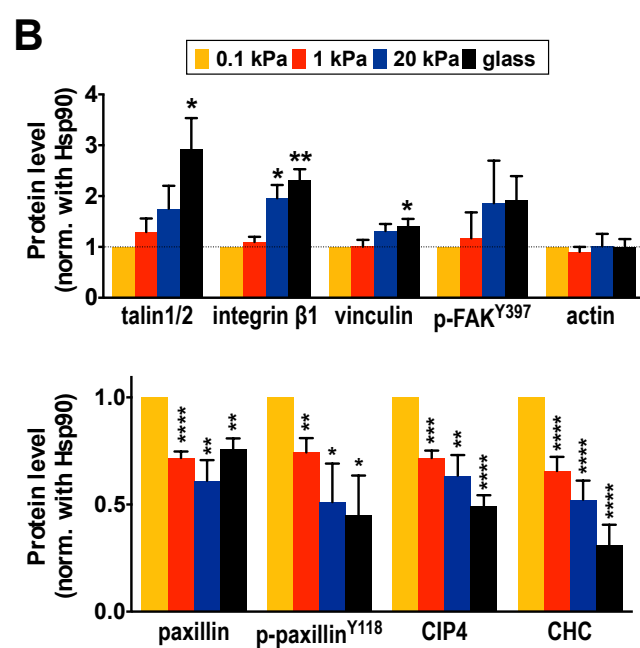
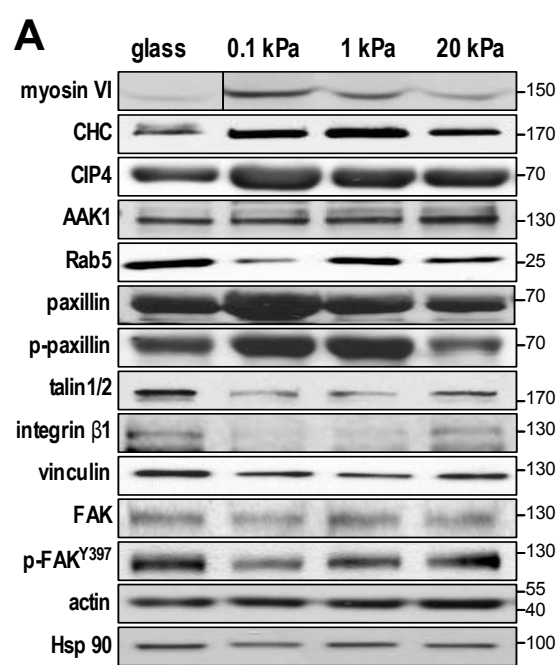


Figure 2– figure supplement 1

Increased Rac1 activity in neurons grown on 0.1 kPa gels

A. Active Rac1 and active RhoA pull-down assay of neurons grown on 0.1 kPa or 20 kPa hydrogels. Cell lysates obtained from cortical neurons grown on substrates (5 hr of culture) were subjected to a GST resin pull-down assay using PAK-GST (upper panel) or GST-Rhotekin-RBD (lower panel), as indicated. The precipitants were analyzed by Western blotting with antibodies specific against Rac1 or RhoA. Histograms reflect quantitative measurement of band intensities (\pm SEM, $n=3$; normalized to the corresponding protein input and relative to that of 0.1 kPa culture; ******, $p<0.05$; *******, $p<0.001$, t test) of the active GTP-bound forms of Rac1 or RhoA.

B. Pharmacological inhibition of Rac1 activation significantly increases the lamellipodium occupancy in 5 hr neuronal cultures on 0.1 kPa gels. Right panel shows representative images of neuronal cultures on 0.1 kPa gels, in the absence and presence of the selective Rac1-GEF inhibitor NSC-23766 (1 μ M; 1 hr treatment), the PI3K inhibitor LY-294002 (10 μ M; 1 hr treatment), or the ROCK inhibitor Y-27632 (25 μ M; 1 hr treatment), stained with phalloidin (red) at the 5 hr or 48 hr time-points after cell plating, as indicated. Dashed line delimits lamellipodium area. Bar, 20 μ m. Histograms summarize average lamellipodium occupancy in 5 hr neurons and percentages of neurite-bearing neurons in 16 hr cultures (\pm SEM; $n=300$ total cells for each group from three independent experiments; *********, $p<0.0001$, unpaired t test) from all experiments similar to that shown in the right panel.



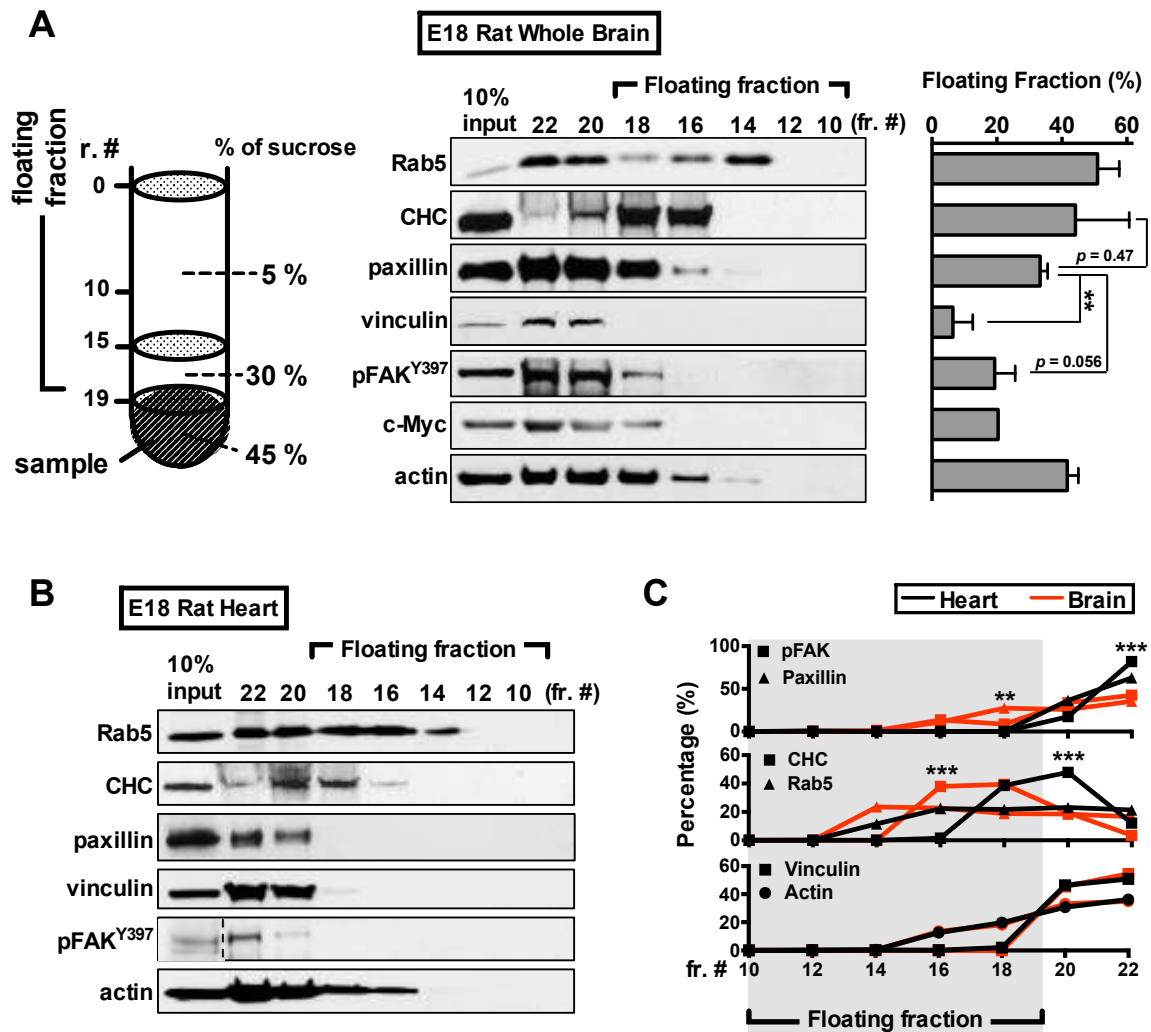


Figure 3– figure supplement 1

Paxillin associates with free-floating vesicles in rat embryonic brain lysate

A-C. Membrane flotation assay of embryonic brain (**A**) and heart (**B**) tissue lysates. Representative Western blot of gradient fractionations probed with antibodies against endocytic factors (Rab5 and CHC), adhesion-associated molecules (vinculin, and phospho-FAK^{Y397}), paxillin, and actin, as indicated. Histogram in **A** reflects quantitative measurements of the protein levels (\pm SEM; $n=3$ independent experiments; “***”, $p<0.01$; compared to that of paxillin; multiple t test for each fraction) found in the floating fraction (collective measurement from fraction 10 to fraction 18) out of the total gradient fractions. (**C**) Traces depict the differential protein levels (\pm SEM; from all experiments similar to that described in A and B, “***”, $p<0.001$; multiple t test) in each gradient fraction between embryonic brain and heart lysates, as indicated.

A

paxillin-mCherry

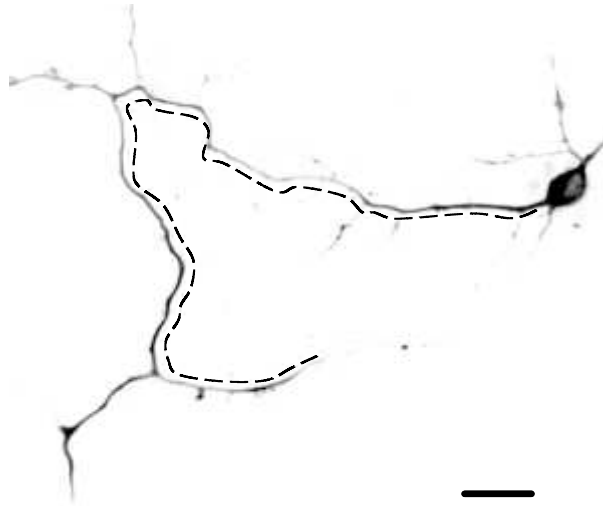
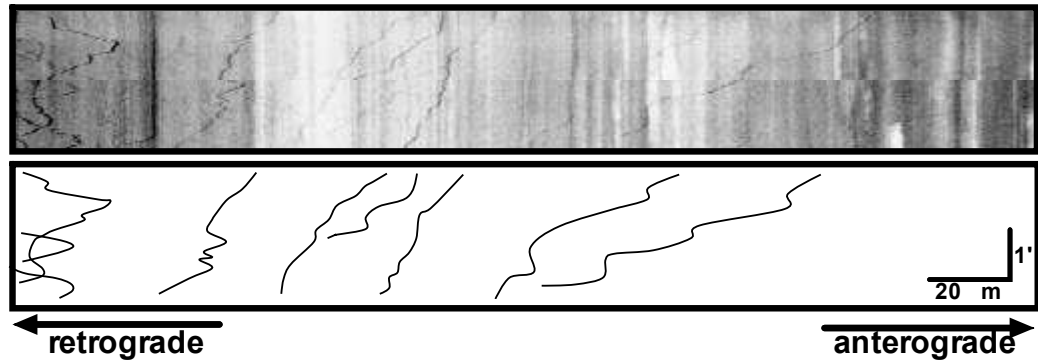
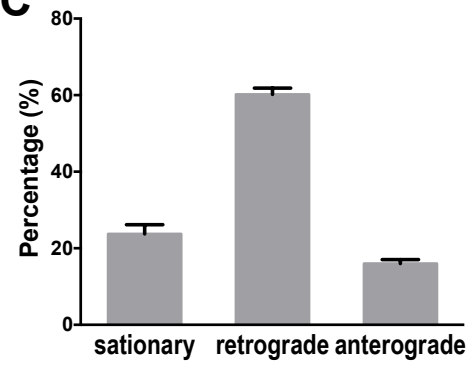
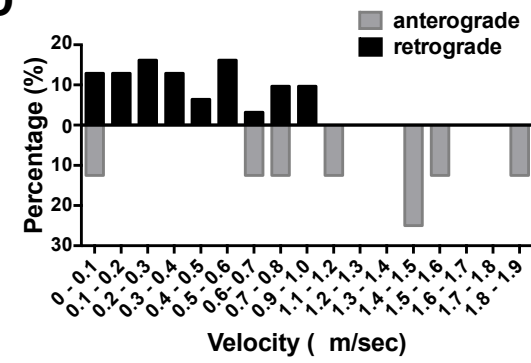
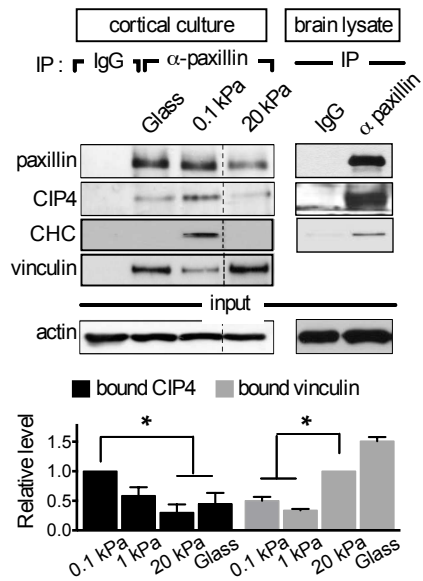
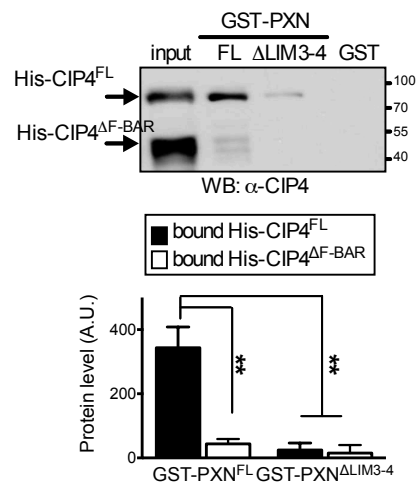
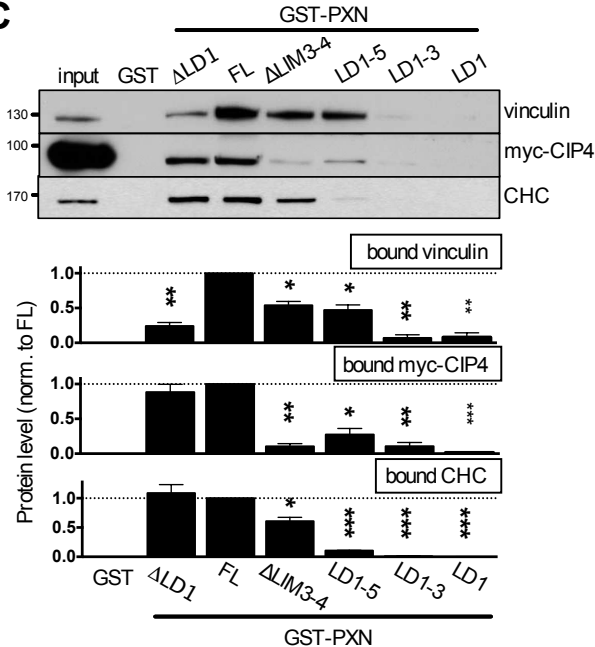
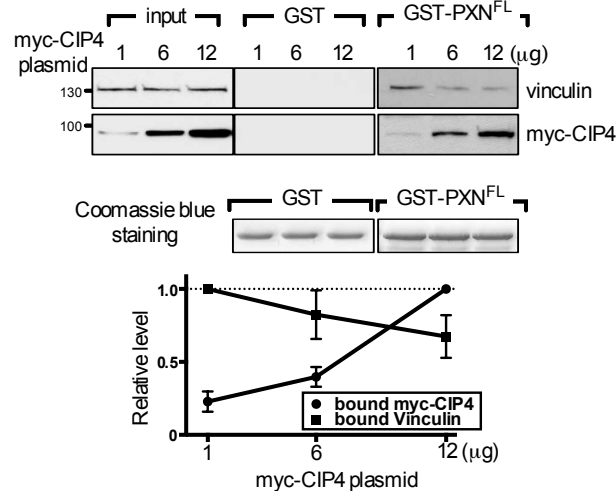
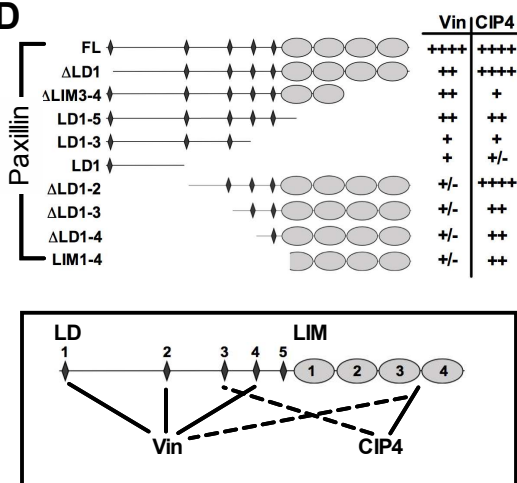
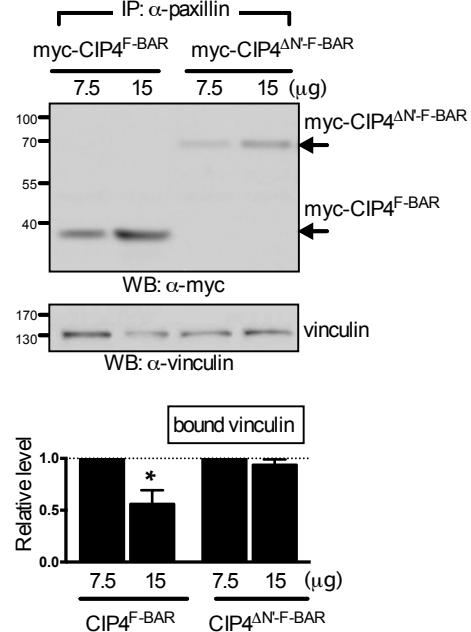
**B****C****D**

Figure 3– figure supplement 2

Ectopically-expressed paxillin displays predominantly retrograde motility

Representative image **(A)** and kymograph **(B)** of paxillin-mCherry trajectories (x-axis, distance; y-axis, time) generated from 180-second time-lapse images (90 frames; 0.5 frames per second), showing bidirectional movement of paxillin-mCherry along the axon (dashed line). Summary of directionality **(C)** and velocity distribution **(D)** of paxillin-mCherry along axons from all experiments similar to that described in B. Data represent means \pm SEM (n=15 cells).

A**B****C****E****D****F**

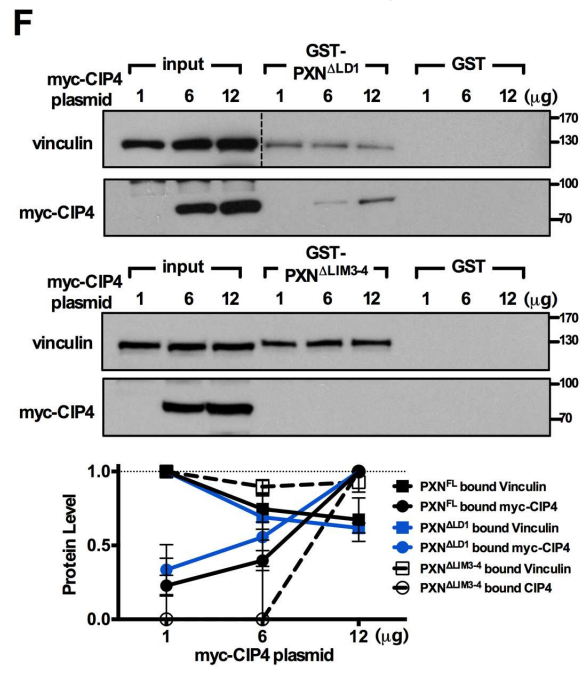
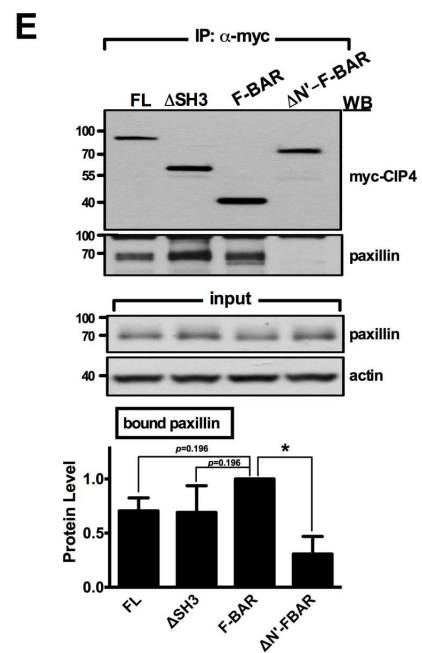
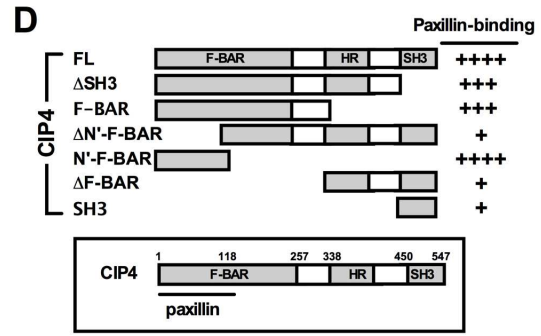
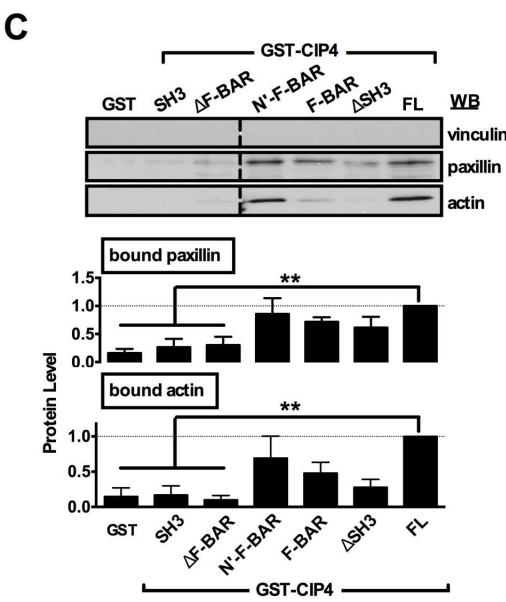
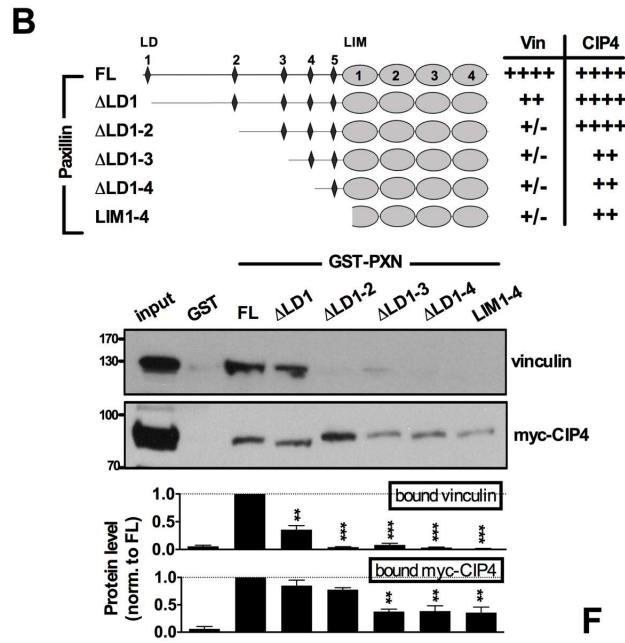
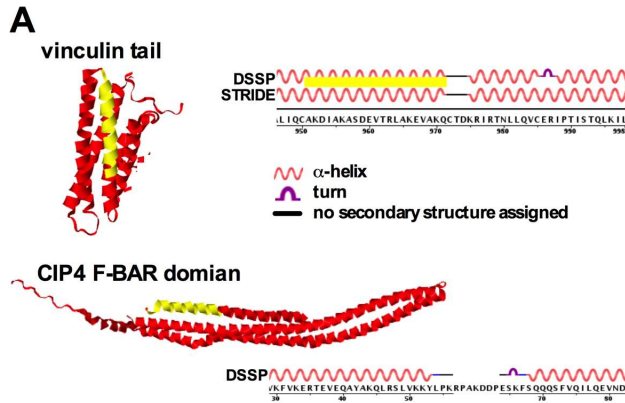


Figure 4– figure supplement 1

Paxillin associates with the F-BAR domain of CIP4

A. Structures of the vinculin tail (PDB ID: 1QKR; top panel) and the CIP4 F-BAR domain (PDB ID: 2EFK; bottom panel) constructed by JMOL, version 14.4.4. Yellow marks indicate the predicted paxillin-binding subdomain (PBS) for vinculin (951K to 970Q) or CIP4 (35R to 55P). Secondary structures were predicted by the DSSP or STRIDE databases.

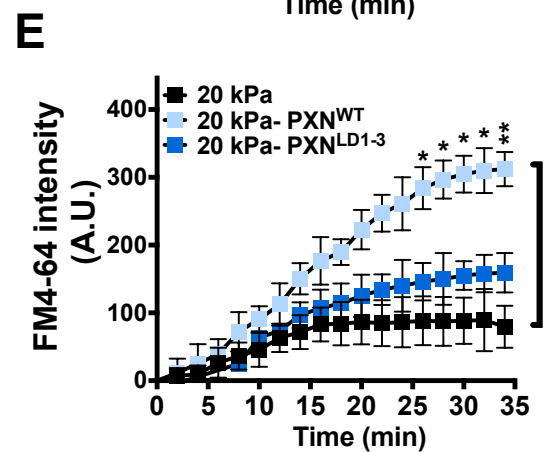
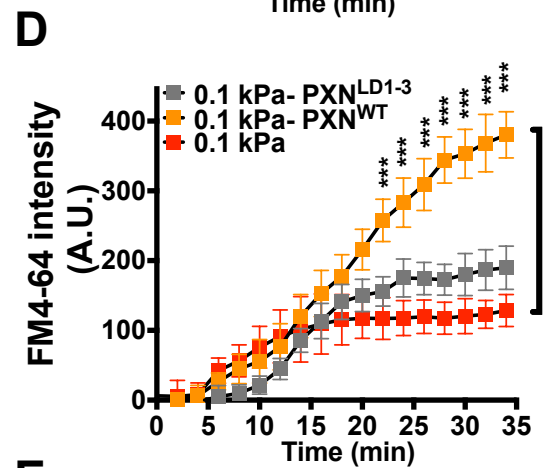
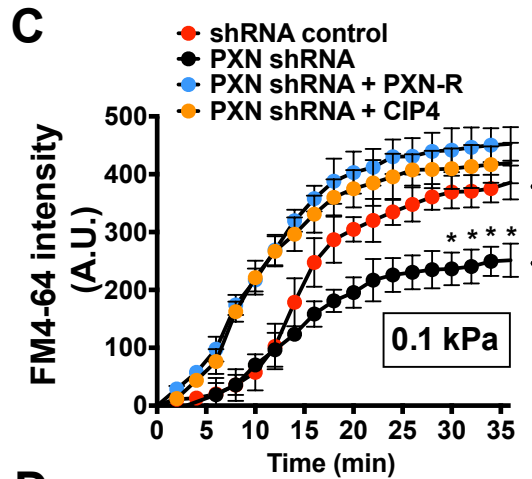
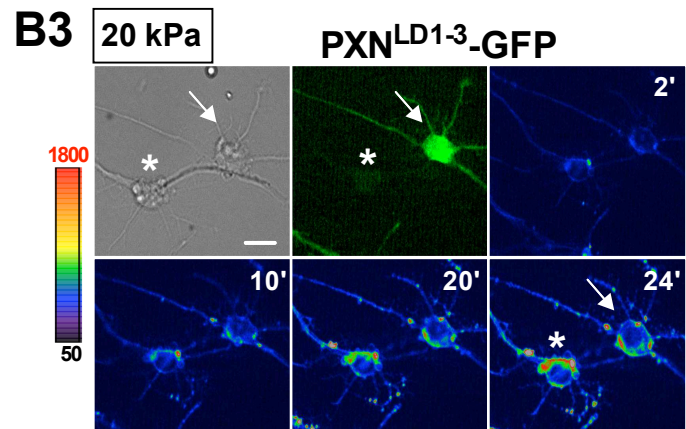
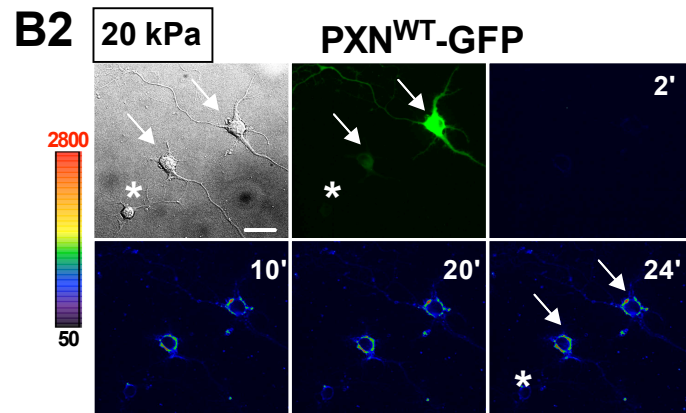
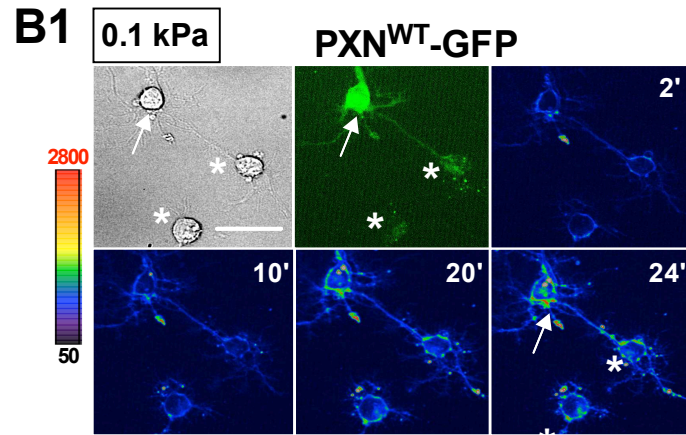
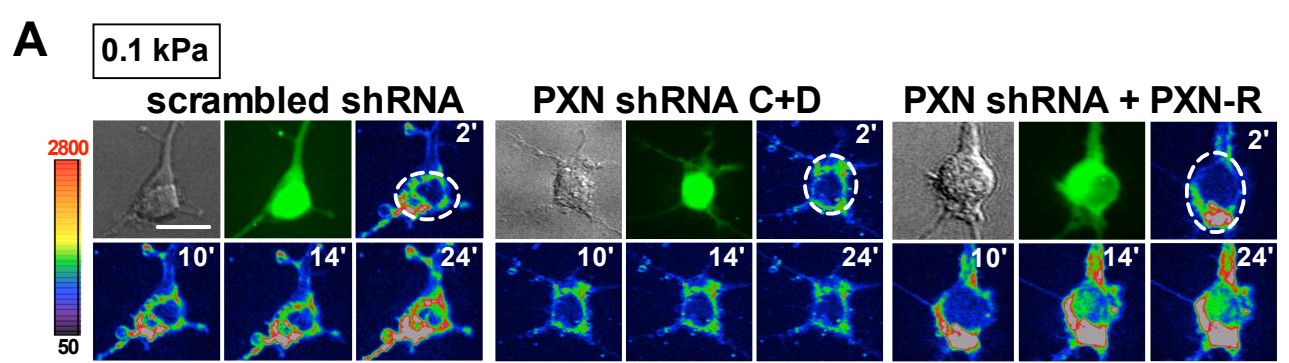
B. Mapping of paxillin domains interacting with CIP4 or vinculin. GST pull-down and immunoblotting of vinculin and myc-CIP4 in lysates of myc-CIP4-expressing HEK293T cells. Histograms reflect quantification of levels of proteins pulled-down by GST fusions of full-length (“FL”) or LD motif-deleted forms of paxillin, all from experiments similar to those shown in top panels (\pm SEM, $n \geq 3$ independent experiments; “***”, $p < 0.01$; “****”, $p < 0.001$; multiple t test). Schematic of GST fusion proteins and table summarizing relative CIP4 or vinculin (“Vin”) binding by paxillin deletion mutants or full-length protein shown in the top panel. Binding strength relative to full-length paxillin indicated as: “++++” > 75% > “+++” > 50% > “++” > 25% > “+” > 5% > “+/-”. Note that although CIP4 primarily associates with LIM domains, deletion of the paxillin LD1-3 domain reduced its affinity for CIP4.

C. Mapping of CIP4 domains interacting with paxillin. GST fusion proteins of full-length CIP4 (“FL”) or its variants with F-BAR domain, HR1 and/or SH3 domain truncations were subjected to GST pull-down assays in HEK293T cell lysates, followed by immunoblotting for paxillin and actin. Histogram reflects quantitative measurement of relative protein levels (\pm SEM, $n \geq 3$ independent experiments; compared to that of FL experiment; “***”, $P < 0.01$; t -test) pulled down by GST-CIP4, as indicated.

D. Schematic of GST fusion proteins used in **B**. Table summarizes relative paxillin binding by CIP4 deletion mutants or full-length protein. Binding strength relative to that of full-length CIP4 is represented as: “++++” > 75% > “+++” > 50% > “++” > 25% > “+”.

E. *In vivo* protein interactions in HEK293T cells co-transfected with plasmids encoding paxillin-GFP and myc-tagged CIP4 deletion mutants or full-length protein, as indicated. Cell lysates were immunoprecipitated by myc antibody and blotted with paxillin or myc antibodies. Histograms show relative protein levels as determined by immunoblotting for paxillin co-immunoprecipitated by myc antibody. Data represents mean (\pm SEM from more than three independent experiments; compared to that of F-BAR experiment; “*”, $P < 0.05$; t -test).

F. *In vitro* protein interaction and competitive binding assays in HEK293T cells transfected with various amounts (1, 6, and 12 μg) of plasmids encoding myc-tagged CIP4 protein (myc-CIP4) and/or control vectors, as indicated. Cell lysates were subjected to a GST pull-down assay with GST-PXN^{FL}, GST-PXN ^{Δ LD1}, GST-PXN ^{Δ LIM3-4} or GST alone, and immunoblotted with vinculin and myc antibodies. Line chart depicts averaged protein levels as determined by immunoblotting of CIP4 or vinculin pulled-down by GST-PXN variant (\pm SEM, n=3-4; normalized to band intensity of corresponding GST-paxillin variant).



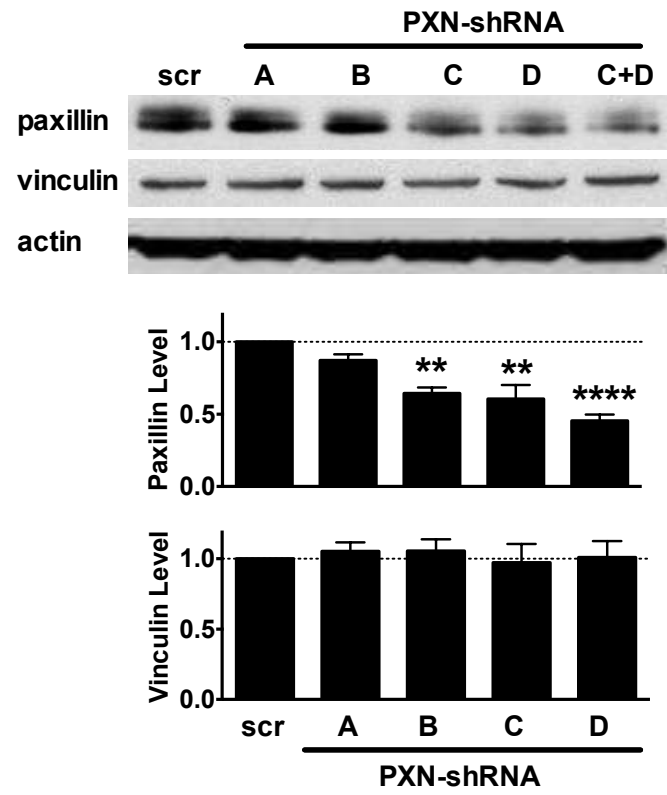
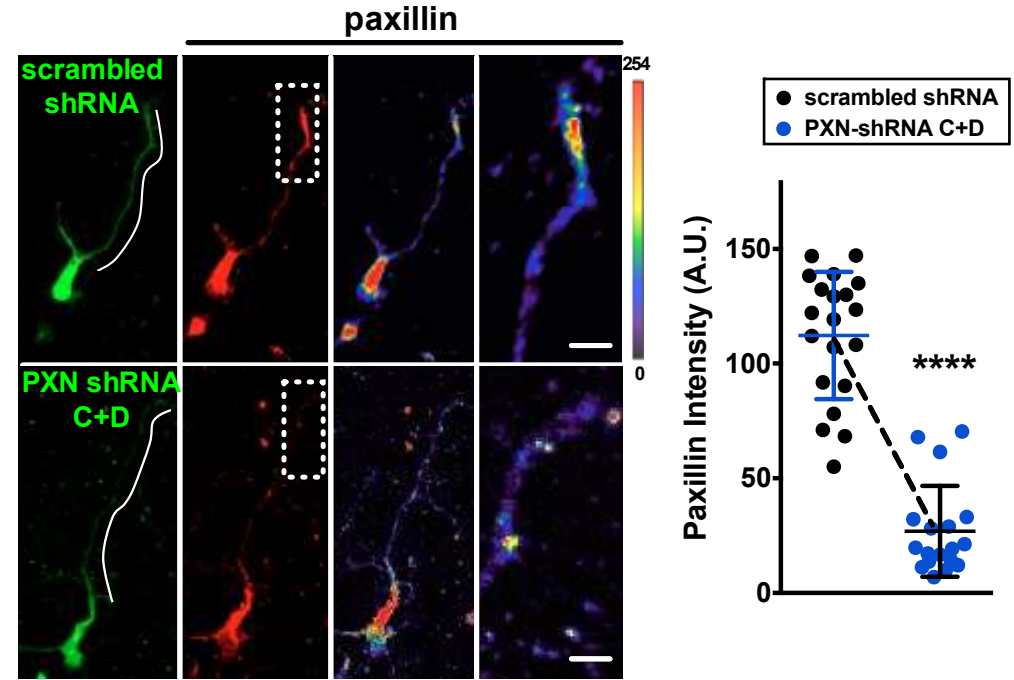
A**B**

Figure 5– figure supplement 1

Knockdown efficiency of PXN shRNAs

A. Western blot showing efficiency of shRNA-mediated paxillin knockdown. Mouse neuroblastoma Neuro-2a (N2a) cells were transfected with plasmids encoding scrambled shRNA (“scr”) or one of four paxillin shRNAs (sequence A, B, C, or D) targeting to different regions of the paxillin sequence. Summary histograms showing that shRNA D exerted a ~2-fold suppression on paxillin expression and it had no effect on vinculin expression. Data represent mean \pm SEM (n=5, normalized to control actin, compared to that of scr experiment; “*”, $P < 0.05$; *t*-test “***”, $p < 0.01$, “*****”, $p < 0.0001$; *t* test).

B. Images of neurons transfected with plasmids encoding scrambled shRNA or paxillin shRNAs (shRNA C + shRNA D), immunostained with antibody specific against paxillin. Right-most panels show the region of interest (ROI, dashed box) of neurite tips at a higher magnification, with the intensity of paxillin staining coded by pseudocolors in a linear scale. Bar: 5 μ m. Dot plot reflects quantification of paxillin immunostaining intensity (\pm SEM, n=20 cells each, normalized to EGFP intensity and relative to scramble control; “*****”, $p < 0.0001$; one way ANOVA with *Dunnett’s post hoc* test).

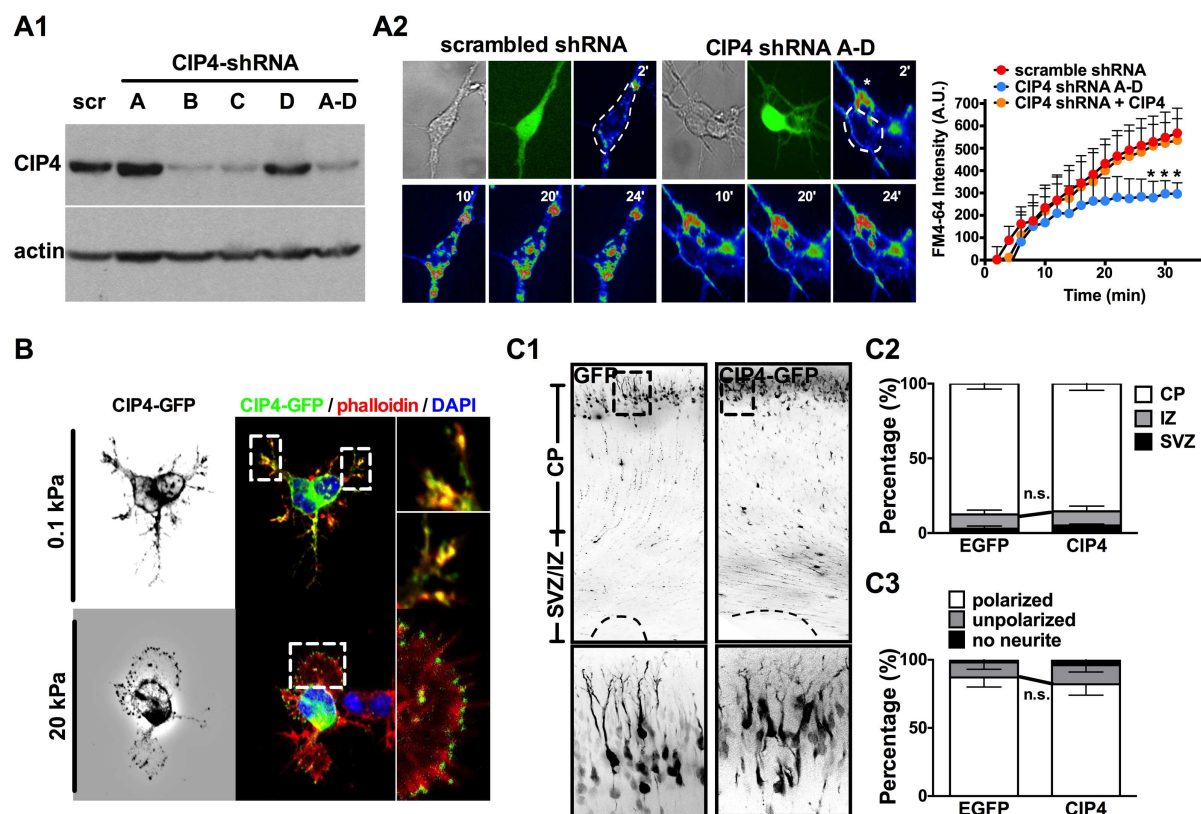


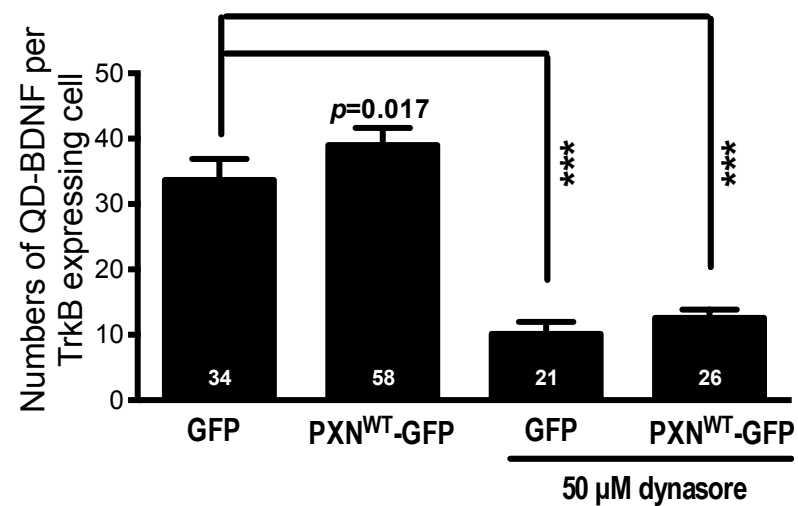
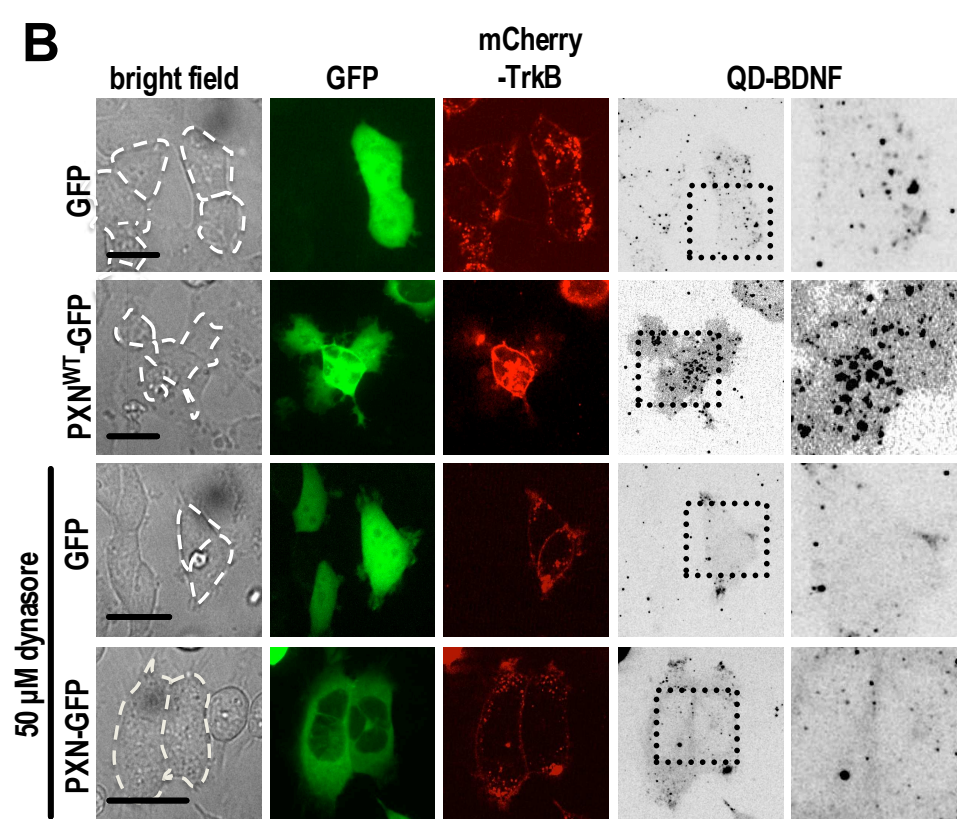
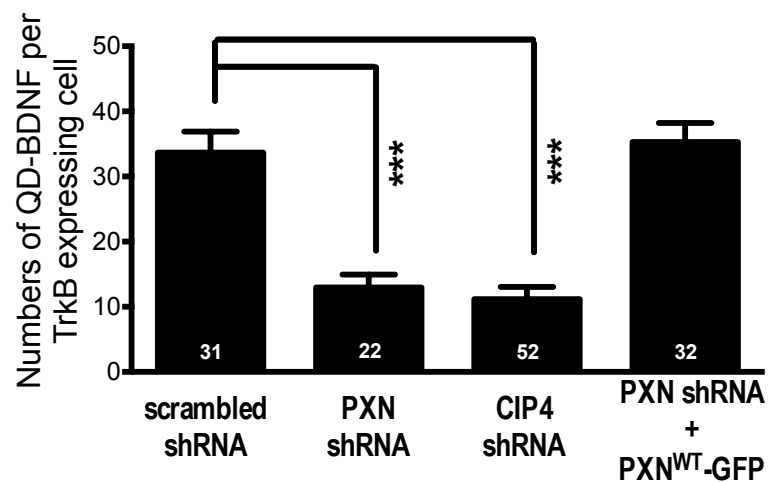
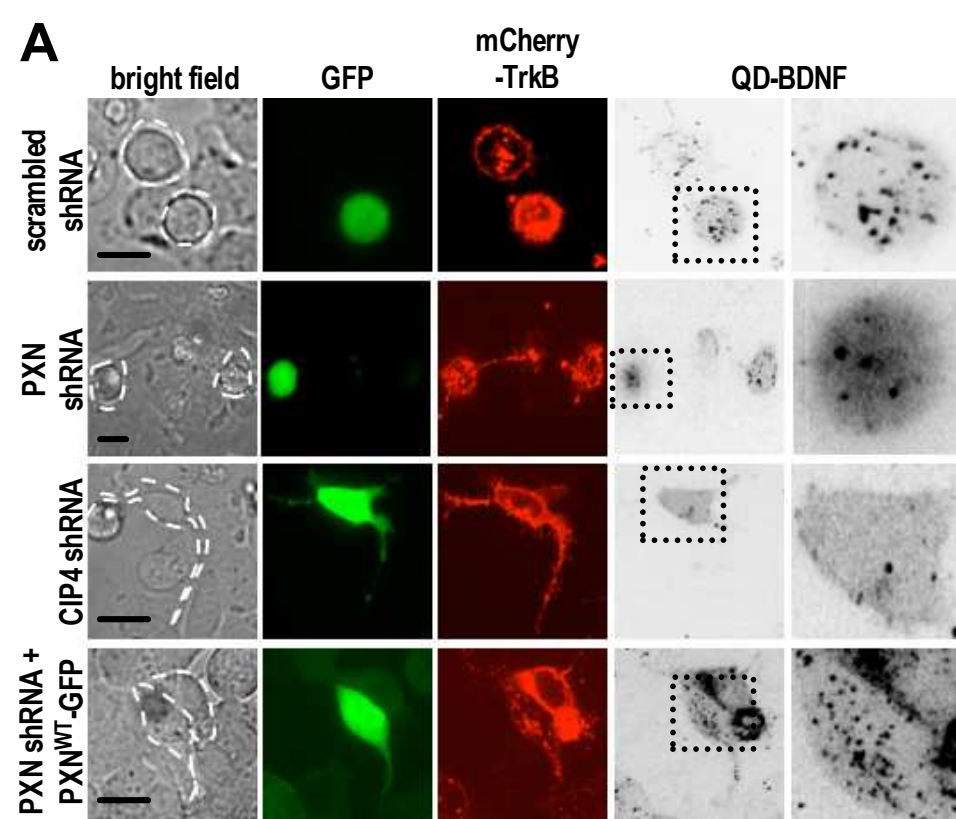
Figure 5– figure supplement 2

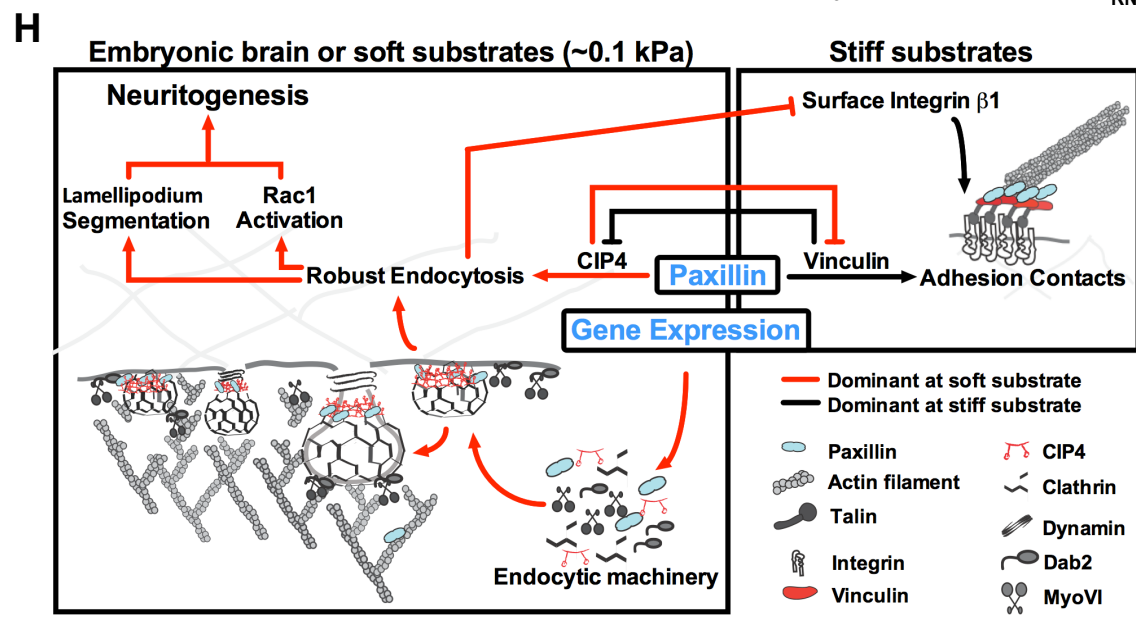
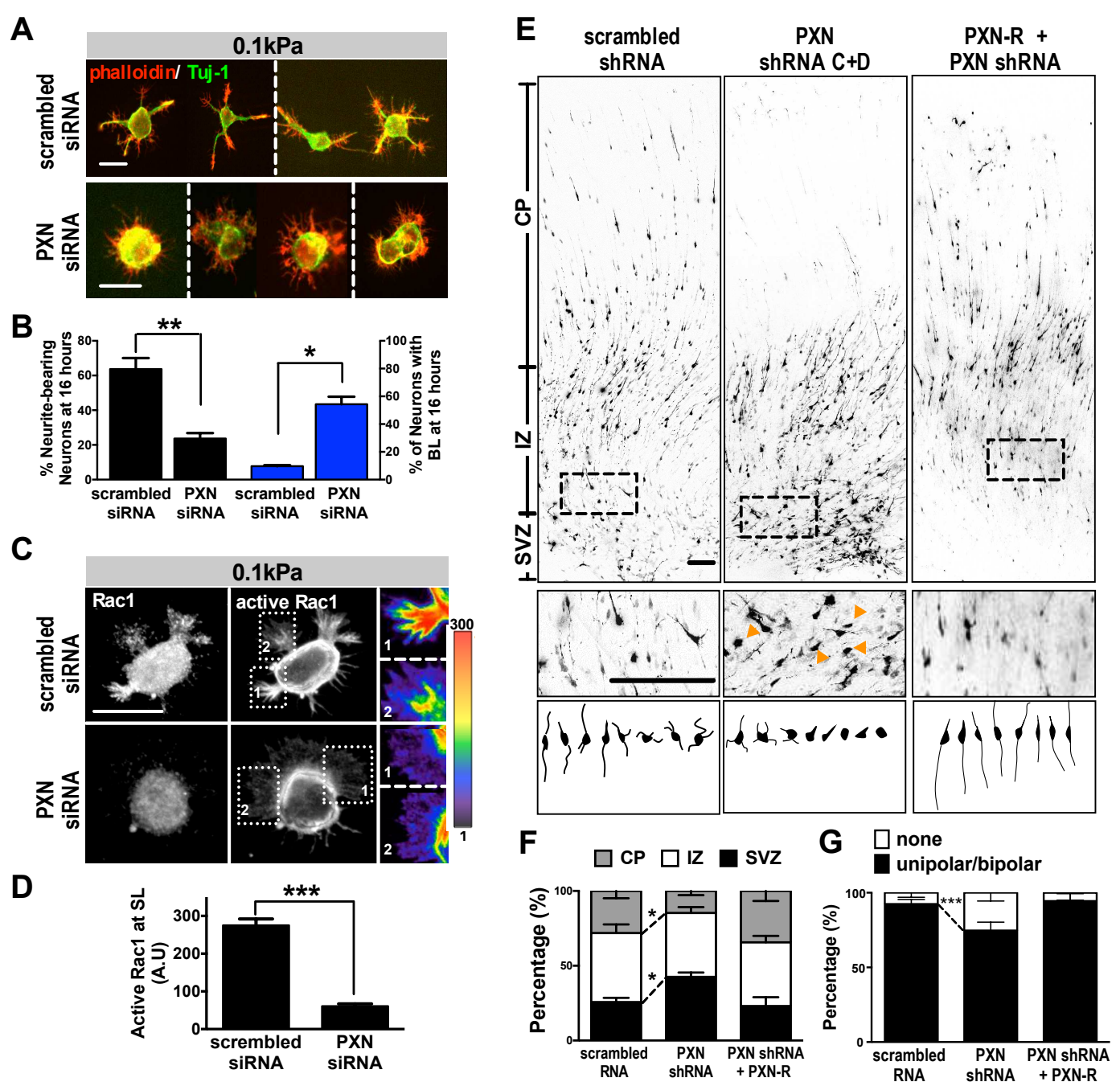
Endocytic function and distribution patterns of CIP4 protein in 0.1 kPa neuronal cultures

A. CIP4 knockdown suppresses endocytic activity of neurons grown on 0.1 kPa gels. (A1) Western blot showing efficiency of shRNA-mediated CIP4 knockdown. HEK293T cells were transfected with plasmids encoding scrambled shRNA (“scr”) or one of four CIP4 shRNAs (sequence A, B, C, or D) targeting to different regions of the CIP4 sequence. (A2) Representative time-lapse images of FM4-64 uptake in 5 hr neurons grown on 0.1 kPa gels. Time-lapse images (20 frames; 2-minute intervals) of neurons isolated from E17.5 rat cortices which were transfected in utero at E16 with constructs encoding scrambled control or CIP4 (“CIP4 shRNA A-D”) shRNA, and/or CIP4-GFP, cultured on 0.1 kPa for 5 hr, followed by endocytosis assay. Dashed circles surround the region of interest (ROI) for quantitative FM4-64 measurements. Asterisk marks non-transduced neighboring cells. Graph at right summarizes the accumulation curves of FM4-64 signal (\pm SEM, $n > 3$ independent experiments, 5-10 cells per group, normalized to $t = 0$ value; compared to that of scrambled control experiment “*”, $p < 0.05$; multiple t tests for each time point).

B. Images of neurons transfected with plasmids encoding CIP4-GFP, stained with phalloidin and DAPI. Right-most panels show the region of interest (ROI, dashed box) of neurite tips at a higher magnification. Note that CIP4-GFP was distributed along the enlarged lamella edge when neurons were cultured on 20 kPa gels.

C. Fluorescence images (**C1**) of P0 rat cortices transfected in utero at E16 with IRES constructs harboring GFP control or CIP4-GFP. The bottom panels show 4x magnifications of boxed regions corresponding to the P0 cortex in the top panels. Bar, 100 μm . (**C2**) Histograms showing the percentages ($\pm\text{SEM}$, $n>3$ cortices each; “n.s.”, not significant, multiple t test) of neurons residing in the cortical plate (“CP”), intermediate zone (“IZ”), or subventricular zone (“SVZ”) regions. (**C3**) Histograms showing the percentage ($\pm\text{SEM}$, $n>150$ cells per cortex, >3 cortices each; “n.s.”, not significant, multiple t test) of transfected cortical neurons exhibiting unipolar/bipolar polarized processes (“polarized”), multiple short neurites without a long tailing process (“unpolarized”), or no process (“no neurite”) in cortices.





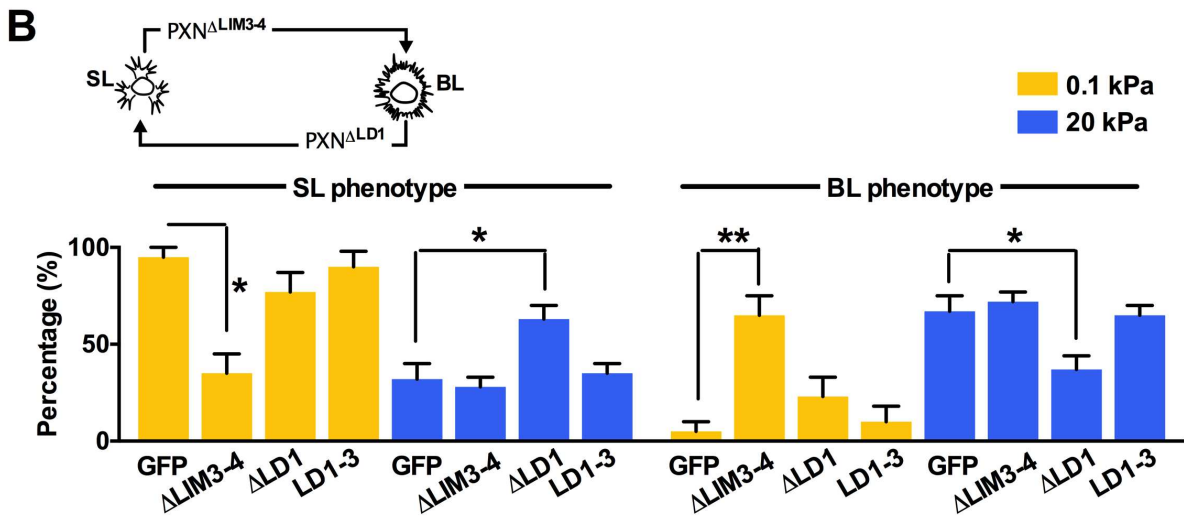
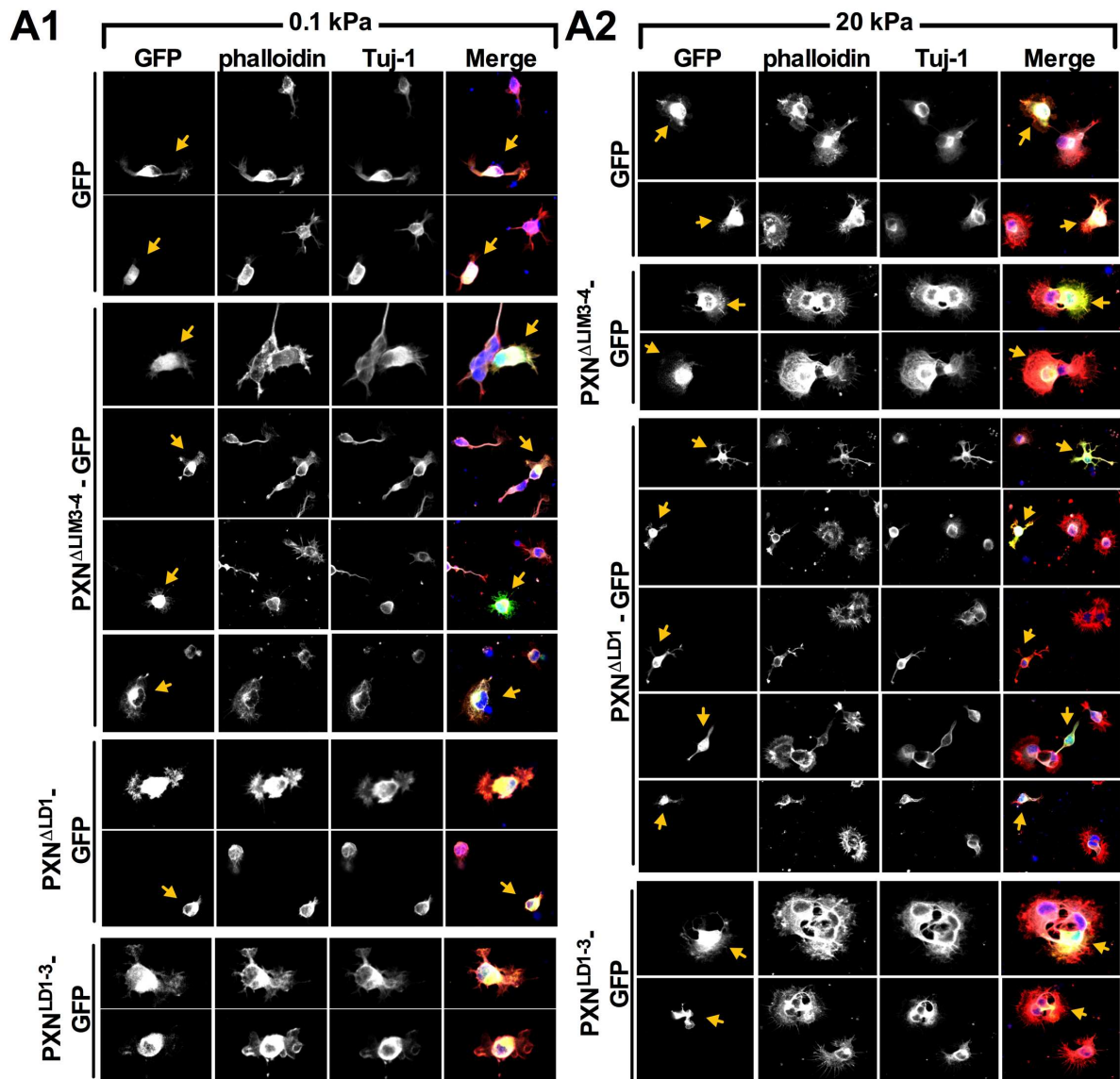


Figure 7– figure supplement 1

Manipulation of paxillin binding affinity leads to a SL-BL phenotypic switch

A. Representative fluorescent images of transfected IUE neurons (yellow arrows) expressing control EGFP and/or a paxillin deletion mutation (Green), cultured on 0.1 kPa (**A1**) or 20 kPa (**A2**) gels for 16 hr, and stained with phalloidin (Red), DAPI (Blue), and antibodies against Tuj-1 (Gray).

B. Histograms summarize the percentages (\pm SEM; “*”, $P < 0.05$; “***”, $p < 0.001$, one way ANOVA with *Dunnett’s post hoc* test) of 16 hr neurons bearing segmented lamellipodia (“SL”) or broad lamellipodia (“BL”) in neurons expressing different paxillin deletion mutations, as indicated. The top panel shows schematic of the neurite phenotype switch observed in the $PXN^{\Delta LIM3-4}$ expressing neuron on 0.1 kPa gel and the $PXN^{\Delta LD1}$ expressing neuron on 20 kPa gel.

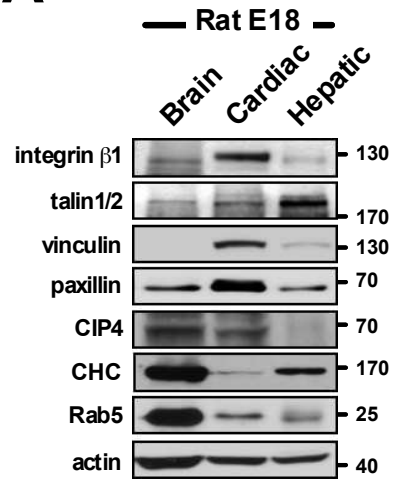
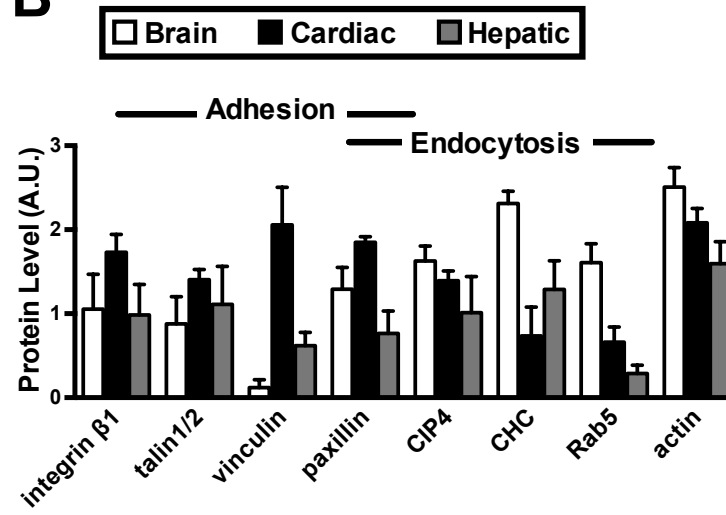
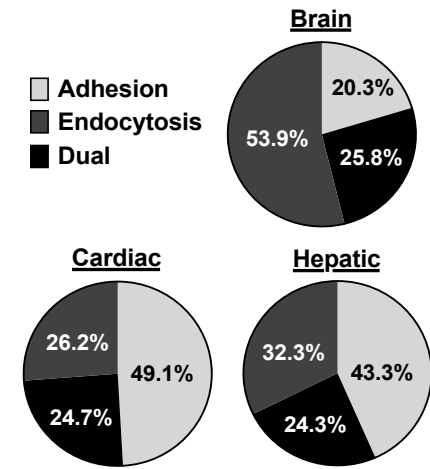
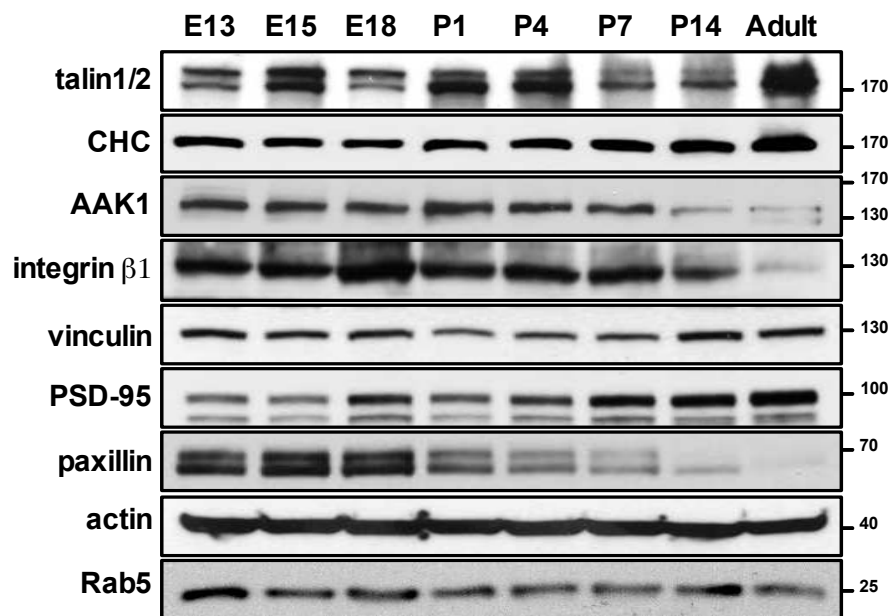
A**B****C**

Figure 7– figure supplement 2

Differential protein abundances between the endocytosis and adhesion machineries in embryonic brain, cardiac, and hepatic tissues

Representative Western blots (**A**) and quantitative analysis (**B**) of embryonic E18 brain, heart and liver lysates. Note that endocytic factors (CHC, Rab5 and CIP4) are more abundant in brain than in heart. Data represent mean \pm SEM in more than three independent experiments. (**C**) Pie charts depicting the relative levels of adhesion and endocytic factors in brain, cardiac and hepatic tissues at E18, from all experiments similar to that described in **B**. The size of each pie slice is proportional to the sum of adhesion molecules (including integrin β 1, talin1/2, vinculin and paxillin) or endocytic accessory factors (including paxillin, CIP4, CHC and Rab5) over all proteins measured. Paxillin and actin are assigned to dual function (endocytosis and adhesion). Note that endocytic factors are highly abundant in embryonic brain tissue.

A



B

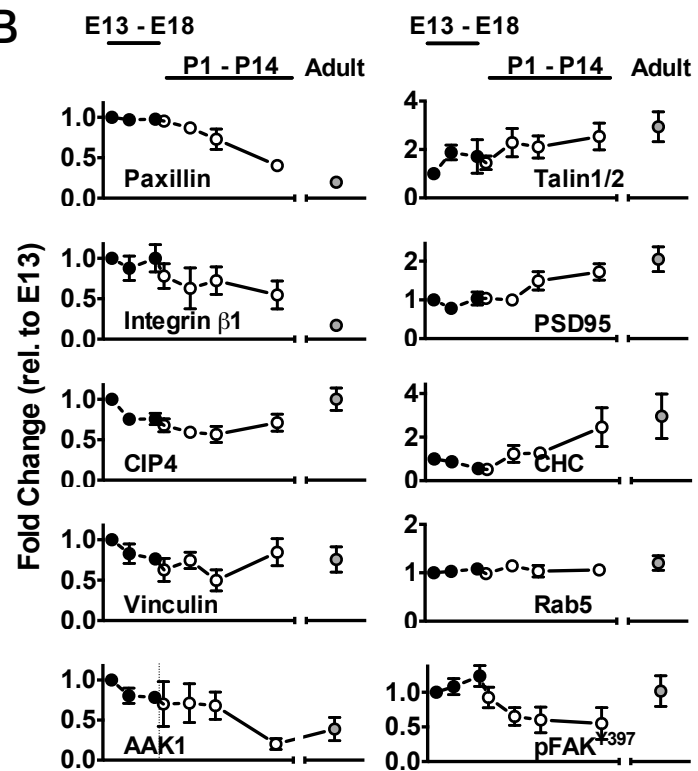


Figure 7– figure supplement 3

Expression time-course of adhesion- or endocytosis-related proteins in developing mouse cerebral cortex

A. Western blots of mouse brain lysates showing protein expression profiles at different developmental stages (including E13, E15, E18, P1, P4, P7, P14, and adult), as indicated.

B. Quantification of protein levels, from all experiments similar to that described in **A**, at different time-points compared to corresponding levels at E13. Data represents mean \pm SEM from more than three independent experiments.

